Master of Science Thesis

Induction Welded Unidirectional Carbon Fiber Reinforced Thermoplastic L-Joints

Joint performance and testing methodology

M.G. van Dijk

Department of Aerospace Structures and Materials
Delft University of Technology
December 2019

Induction Welded Unidirectional Carbon Fiber Reinforced Thermoplastic L-Joints

Joint performance and testing methodology

by

M.G. van Dijk

to obtain the degree of Master of Science
at the Delft University of Technology,
to be defended publicly on Friday December 13, 2019 at 09:30.

Student number:	4209141	
Project duration:	September 3, 2018 – December 13, 2019	
Thesis committee:	Prof. dr. C. Kassapoglou,	TU Delft, chairman
	Dr. C.D. Rans,	TU Delft
	Dr. D. Zarouchas,	TU Delft
	Ir. M. Labordus,	KVE Composites

This thesis is confidential and cannot be made public until December 13, 2021.

Abstract

Induction welding is an effective technique for joining unidirectional carbon fiber reinforced thermoplastic composites and L-joints can be produced through quick and cost-effective processing steps. However, due to high localized stresses in the skin-stiffener interface, these L-joints are often avoided in primary aircraft structures. Also, no international testing standards have been developed for testing of such joints.

A method was developed for the implementation of a neat thermoplastic resin fillet between the L-joint skin and stiffener web using the induction welding process in an attempt to remove the high stress concentration at this location. A 35.4% increase in quasi-static pull-off strength was measured with a weight penalty of less than 0.5%. This result was compared with a similar autoclave co-consolidated joint, which showed an 80.9% improvement. An ANSYS Parametric Design Language finite element model was developed based on the virtual crack closure technique and it showed that the joint pull-off performance is strongly dependent on geometric parameters such as the skin and stiffener thickness. Also, a new test setup was developed, which reduced internal stresses created by the setup compared to those commonly used in literature.

By further improving the method through which the fillet is joined to the induction welded L-joint, a performance increase similar to that of the co-consolidated joint should be achievable. Test results have shown that the use of this type of fillet can lead to the skin-stiffener interface no longer being the critical failure point for realistic joints in primary aircraft structures.

Acknowledgements

I would like to thank my supervisor and committee chair, Prof. dr. Christos Kassapoglou, for his continuous support, availability to answer questions and immense technical knowledge in the field of aerospace composite structures.

I would also like to thank my supervisor, Dr. Irene Fernandez Villegas, for her insightful advice regarding welding of thermoplastic composites and interpreting micrographs, and her feedback on my research.

I wish to express my sincere gratitude to the people at KVE Composites for receiving me with open arms and for their patience and support. In particular I want to thank Maarten Labordus, my company supervisor, and Alexander Mitrousias, my day-to-day advisor, for their assistance with any problems I encountered and with any questions I came up with. I also want to thank Tom Jansen and Michiel Bruijkers, who were always available for discussions about composites and induction welding.

M.G. van Dijk
Delft, December 2019

Contents

List of Figures

List of Tables

List of Abbreviations

AITM	Airbus Industries Test Method
APDL	ANSYS Parametric Design Language
ASTM	American Society for Testing and Materials
CC	Compliance calibration
CF	Carbon fiber
CFRP	Carbon fiber reinforced polymer
CFRTP	Continuous fiber reinforced thermoplastic
CNC	Computer numerical control
CV	Coefficient of variation
CZM	Cohesive zone model
DASML	Delft Aerospace Structures & Materials Laboratory
DCB	Double cantilever beam
DTC	Dutch Thermoplastic Components
ENF	End notched fixture
FE	Finite element
FEA	Finite element analysis
FEM	Finite element method
ISO	International Organization for Standardization
HSD	Honest significant difference
KVE	Kok & Van Engelen
LSS	Lap shear strength
MBT	Modified beam theory
MCC	Modified compliance calibration
MMB	Mixed mode bending
PA6	Polyamide/Nylon 6
PA11	Polyamide/Nylon 11

PA12	Polyamide/Nylon 12
PEEK	Polyetheretherketone
PEI	Polyetherimide
PEKK	Polyetherketoneketone
PPS	Polyphenylenesulfide
PRIM	Printed Injection Mould
PROP	Propagation
SERR	Strain energy release rate
SLS	Selective laser sintering
TPC	Thermoplastic composite
TSC	Thermoset composite
UD	Unidirectional
VCCT	Virtual crack closure technique
VIS	Visible onset

List of Symbols

a	Crack/delamination length	[mm]
b	Coupon width	[mm]
c	Material constant in Paris law	[–]
da/dN	Fatigue crack growth rate	[mm/cycle]
dy	Crosshead displacement	[mm]
E	Young's modulus	[GPa]
E_{11}	Longitudinal tensile modulus	[GPa]
E_{22}	Transverse tensile modulus	[GPa]
E_{33}	Through-thickness tensile modulus	[GPa]
f	Linear fracture criterion index	[–]
G	Strain energy release rate	[N/mm]
G_{12}, G_{13}	In-plane shear modulus	[GPa]
G_{23}	Interlaminar shear modulus	[GPa]
G_I	Mode I SERR	[N/mm]
G_{II}	Mode II SERR	[N/mm]
G_{III}	Mode III SERR	[N/mm]
G_c	Critical SERR	[N/mm]
G_{Ic}	Critical mode I SERR	[N/mm]
G_{IIc}	Critical mode II SERR	[N/mm]
G_{IIIc}	Critical mode III SERR	[N/mm]
G_{max}	SERR at peak loading	[N/mm]
G_{th}	Threshold SERR	[N/mm]
k	Skin grip spring constant	[(N/mm)/mm]
n	Material constant in Paris law	[–]
P	Applied force	[N]
R	Fatigue load amplitude	[–]

R_1	Ratio of mode II SERR to mode I SERR	[–]
R_2	Ratio of failure to critical mode I SERR	[–]
S_y	Out-of-plane tensile stress	[MPa]
$S_x y$	In-plane shear stress	[MPa]
T_g	Glass transition temperature	[°C]
T_m	Melting temperature	[°C]
t_{ply}	Ply thickness	[mm]
V_f	Fiber volume fraction	[%]
W_f	Fiber weight fraction	[%]
x	Position in weld line	[mm]

δ	Load point displacement	[mm]
Δ	Modified beam theory correction factor	[mm]
ϵ_T	Elongation at break	[%]
ν_{12}, ν_{13}	In-plane Poisson's ratio	[–]
ν_{23}	Transverse Poisson's ratio	[–]
ρ	Density	[g/cm^3]
σ	Tensile strength	[MPa]
σ_{11}	Longitudinal tensile strength	[MPa]
σ_{22}	Transverse tensile strength	[MPa]
τ_{12}	In-plane shear strength	[MPa]

1 Introduction

1.1. Overview and Statement of Need

Continuous fiber reinforced thermoplastic composites (TPCs) exhibit several advantages compared to their thermoset counterparts. They have greater damage tolerance, fracture toughness and impact resistance, shelf life is infinite without the need for low temperatures and by applying heat they can be reformed and reprocessed [1–3]. This allows for cost-effective, rapid production techniques, quicker than curing thermoset resins, and makes welding of TPCs possible [4]. Thermoplastic components built from unidirectional (UD) plies have yet to be implemented in welded primary aircraft structures, but induction welded carbon fabric rudders and elevators for the Gulfstream G650 have been in production for several years and show great potential for future applications [5, 6]. The induction welding technology used for these components was developed by Kok & Van Engelen Composite Structures (KVE), which also played a crucial role in the realisation of this thesis. In order to better understand the induction welding process and its use in primary aircraft structures, research should be done on parameters affecting joint performance and how such joints can be tested reliably.

Thermoplastic stiffeners in aircraft structures are preferably designed with simple geometric shapes. This allows for a one-shot process in which stiffeners are produced from flat laminates through hot press forming. This process results in relatively short production times and a low number of processing steps, minimizing overall cost. *Niu* [7] listed geometries of aluminium stiffeners used in a range of aircraft types and showed that, in particular in the wing and tailplane, stiffeners with simple shapes are used, such as L-, C- and Z-stiffeners. In skin-stiffener joints where such simple geometries are used, a stress concentration is present at the point where skin and stiffener meet. While for aluminium skin-stiffener joints an adhesive fillet can be used in order to reduce this stress concentration, a method for welded TPCs has not yet been developed. By eliminating this stress concentration, joint strength and fatigue performance can be improved, which can potentially lead to a reduction in weight and cost.

In order to certify new materials or manufacturing techniques in aircraft structures, a large number of tests must be performed. Some important design allowables for skin-stiffener joints are shear and pull-off strength. Standardized tests for shear strength have been developed either for mechanically fastened or adhesively bonded joints and no standardized tests have been established for pull-off strength of skin-stiffener joints. Currently static and fatigue shear strength of welded TPC joints is often determined through single-lap shear tests [8] and although using the same test consistently provides useful comparative data, the test is not necessarily an accurate representation of real-world aircraft structures. Research is needed to study if existing testing methodologies can be applied to induction welded skin-stiffener joints or if a new method should be developed.

During previous pull-off experiments on induction welded TPC L-joints performed by KVE, crack growth was found to start at the skin-stiffener interface under the stiffener web and propagated along the weld line until full separation had occurred. This failure process can be explained by the presence of high localized stresses at the crack front. Crack propagation can be simulated using the finite element method (FEM) with the virtual crack closure technique (VCCT), assuming crack propagation along the weld line and using critical strain energy release rate values of the TPC material found through experiments [9–11]. An accurate model for predicting failure of induction welded skin-stiffener joints under pull-off loading can provide a useful insight in how geometric parameters and test setups influence joint performance.

1.2. Research Goals and Objectives

The primary goals of this thesis are to estimate the expected static joint strength of induction welded unidirectional carbon fiber reinforced thermoplastic L-joints under pull-off loading and to develop a methodology to manufacture and test specimens which can approach or exceed this strength. The following objectives were defined to achieve these goals:

1. Find testing methodologies that can be used or modified to test these joints under pull-off loading.
2. Estimate the expected static joint strength based on data available in literature or experiments.
3. Determine which geometric parameters have the largest influence on joint performance.
4. Determine to what extend physical tests approach or exceed the predicted joint strength.

1.3. Research Question

The research question and sub-questions to be answered follow from the research objective. The main research question is: ”What specimen geometries can be recommended to improve the performance of joints typical for primary aircraft structures and what testing methodologies can be recommended to determine static joint strength of induction welded UD CF/thermoplastic joints in pull-off loading conditions?” The following sub-questions were formulated:

1. What are typical joint configurations under pull-off loading in aircraft structures?
2. What testing methodologies can potentially be used or modified to test these joints under pull-off loading?
3. What testing methodology has the most potential for testing these joints under pull-off loading, in terms of manufacturing cost and time for the test setup and specimens, and representativeness of actual aircraft structures?
4. What is the expected static joint strength of these joints under pull-off loading conditions?
5. Which geometric parameters affect coupon performance most in pull-off joints and what geometric configuration results is the best performing joint?
6. What process and tooling parameters are required to develop the best performing joint?
7. To what extend do physical tests approach or exceed the expected joint strength?

1.4. Scope of Thesis

Due to the high cost of aerospace-grade TPCs, such as polyetheretherketone (PEEK) and polyetherketoneketone (PEKK), only UD carbon fiber reinforced polyamide 11 (CF/PA11) was used. This material was readily available for this thesis and its lower melting temperature, 183°C [12] as opposed to 337°C for PEKK [13], allowed for quicker and easier processing.

This thesis is limited to quasi-static testing and no fatigue tests were conducted due to time constraints. A finite element model for fatigue performance was developed and will be briefly discussed, but this model has not been validated using test data.

1.5. Thesis Outline

This thesis starts in Chapter 2 with a review of literature on thermoplastic composites, induction welding of thermoplastic composites and typical joints in aircraft structures. Testing methodologies used to determine shear and pull-off joint strength will be discussed, as well as the influence of various geometric parameters on joint performance. Fracture mechanics applicable to pull-off testing of skin-stiffener joints will also be examined. In Chapter 3 the research methodology is described, followed by the production process of test samples in Chapter 4. Test results are discussed in 5 and compared with FEM simulations. Finally, conclusions are drawn in Chapter 6 and recommendations are provided for further research.

2

Literature Review

This literature review provides a brief background on thermoplastic composites and its use in aircraft structures in Section 2.1, followed by an overview of the basic principles of induction welding and its application to thermoplastic composites in Section 2.2. In Section 2.3 common loading conditions in aircraft structures are discussed. This is followed by a review on testing methodologies and influential parameters for shear joints in Section 2.4 and pull-off joints in Section 2.5. In Section 2.6 the basics of fracture mechanics and fatigue crack growth are presented and in Section 2.7 some concluding remarks are given.

2.1. Thermoplastic Composites

Fiber reinforced polymers, often referred to as composites, are a material type consisting of a polymer matrix reinforced with fibers, usually carbon in the aerospace industry. These materials show a more favorable strength- and stiffness-to-weight ratio compared to metals, which can reduce aircraft weight, resulting in lower operational costs and a reduction of gas emissions [14]. Composites with continuous fibers, most commonly used in aircraft structures, come in the form of unidirectional tapes and woven fabrics, before being stacked to form a laminate. This allows for components to be designed with different stiffness and strength properties in the various orientations. The polymer binding the fibers together can either be a thermoset or a thermoplastic, both with very different material properties. Thermoplastic composites (TPCs) exhibit higher damage tolerance, fracture toughness and impact resistance than thermoset composites (TSCs) and their shelf life is infinite at room temperature [1–3, 15–18]. TSCs on the other hand require a lower processing temperature and pressure and the raw material is currently cheaper. Because thermoplastic polymers can be reformed and reprocessed when sufficient heat is applied, TPCs can be processed through different methods than their thermoset counterparts, for example through welding.

In 1988, demonstrator wing ribs were manufactured for the V-22 tiltrotor (Bell Helicopter Textron, Incorporated) utilizing a discontinuous long-fiber reinforced TPC, showing significantly better open-hole compression properties compared to the baseline thermoset structure [17]. The landing flap ribs and impact resistant ice-protection plates on the Dornier 328 were the first carbon fiber reinforced thermoplastic (CFRTP) structural parts in a civil fixed wing aircraft and made its first flight in 1991 [19, 20]. In 1997, Westland developed a carbon fiber reinforced thermoplastic tailplane and fins for the Westland 30-300 helicopter [21].

2.2. Induction Welding

Electromagnetic induction has been studied since the 1830s [22] and has been used to heat metals since the middle of the 1910s [23]. In recent decades extensive research has been done on heating and welding of TPCs by means of induction as outlined by *Ahmed et al.* [24] and *Bayerl et al.* [22]. By running an alternating current through a conductive coil, a magnetic field is generated with an equal frequency. This alternating magnetic field induces eddy currents in electrically conductive materials in proximity to the coil. In case of a conductive mesh, either metallic or non-metallic, for example carbon fiber, heat can be generated through three mechanisms: joule losses in the fibers and dielectric hysteresis and contact resistance in the fiber junctions [22, 25]. In order for eddy currents to be induced in electrically conductive fibers, closed-loop circuits must be present, either in the form of woven fabrics or laminates with varying fiber orientations. In electromagnetic materials, magnetic hysteresis occurs. Heating through magnetic hysteresis is independent of eddy currents and can occur in metallic meshes or particles, for example embedded in a polymer film as demonstrated by *Suwanwatana et al* [26]. For welding of laminates consisting of non-conductive fibers, such as glass or aramid, or laminates with all fibers in the same orientation, susceptor material is required between the laminate interfaces, commonly in the form of a woven carbon fiber fabric or metallic particles [18, 22]. In this thesis, carbon fibers were used in a quasi-isotropic laminate and therefore a susceptor was not required.

Several phenomena occur during induction welding of TPCs that can affect joint quality. The edge effect is the most troublesome of these [24]. If a weld zone is located near the edge of a workpiece, induced eddy currents are unable to follow the magnetic field generated by the induction coil. Because these currents must created closed-loop paths, they are forced to travel along the laminate edge. This results in a high current density near the edge of the workpiece, causing increased temperatures in this region, as shown in Figure 2.1.

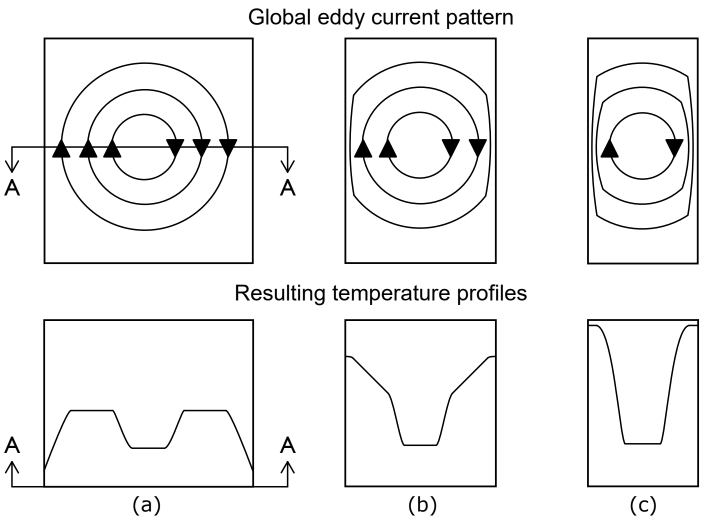

Figure 2.1: Eddy current pattern and temperature profile as function of workpiece width. No edge effect is observed in (a), but the effect is clearly visible in (c). Redrawn from [24].

Rudolf et al. [27] studied the influence of several basic process parameters on the heating rate and heat distribution in CFRTPs in stationary experiments. They determined that a higher current frequency strongly increases the power and heating rate in the workpiece and that for increased frequency the penetration depth of the electromagnetic field is reduced. They and *Pappadà et al.* [28] also reported that increasing generator power and reducing coupling distance, the distance between the coil and workpiece, both result in an increase in heat generation. Current frequency, generator power and coupling distance must thus be balanced in order to obtain an effective temperature distribution [24]. Coil geometry also has an strong influence on heat distribution in the workpiece [23, 27, 29].

For a high quality weld, pressure should be applied appropriately, in order to initiate strong contact between laminates. Too high or unequally divided pressure can lead to matrix squeeze-out at the edges [30] and insufficient pressure can lead to an increase in void content and delaminations. Accurate temperature control is also important. *Flanagan et al.* [31] showed that overheating CF/PEEK during induction welding causes porosity in the weld line, voids and delaminations in the laminates and squeeze-out at the sides. Insufficient pressure during cooling can lead to cracks in the material. These are caused by thermal stresses when the degree of crystallinity in the matrix is high, resulting in shrinkage of the matrix, which is prevented by the fibers [30].

2.3. Loading of Skin-Stiffener Joints

McDonnell Douglas Corporation and Northrop Corporation [32] published a report in which they identified typical direct and indirect out-of-plane loading conditions in composite aircraft structures. In wing and empennage torsion boxes subjected to fuel and aerodynamic pressure, out-of-plane stresses are present between spars and ribs and the skin. Skin-stiffened panels subjected to compression and/or shear can buckle, promoting skin-stiffener separation as shown in (a) in Figure 2.2. Pressurisation of the fuselage during flight, fuel pressure in the wings or aerodynamic loads can cause so-called pressure pillowing, where the skin pulls away from frames and stringers [33], as shown in (b) in Figure 2.2. In stiffener elements with a flange on both sides of the web, such as I-beam spar or T-stiffeners, chordwise tensile loads introduce interlaminar tensile stresses in the web, which can cause it to split. Also out-of-plane stresses in skin-stiffener joints can be observed when a stiffener is subjected to external loads from, for example, overhead luggage bins in the fuselage. Another common scenario is out-of-plane stresses induced at stiffener terminations in in-plane loaded stiffened panels due to geometric discontinuity, which can lead to separation of the stiffener before overall failure of the structure is observed [34].

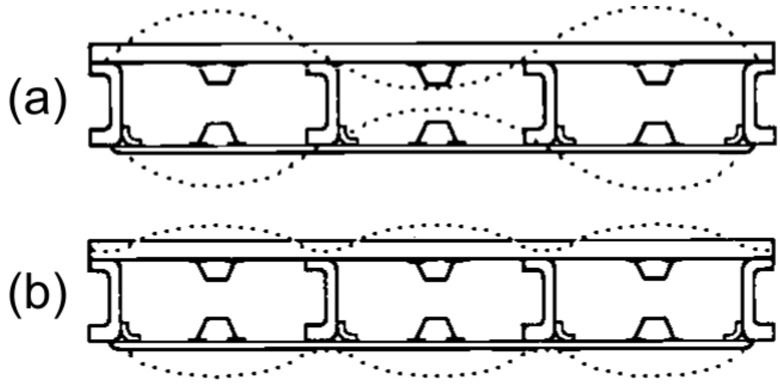

Figure 2.2: (a) (Post)buckling and (b) pressure pillowing in stiffened torque box [35].

Kim and Kedward [36] identified aircraft structures subjected to in-plane shear loading. Large aircraft fuselages consist of multiple sections, which are joined together. The joints between these sections encounter in-plane and transverse shear loading. Also, in-plane shear stresses are dominant in joints in assembled wing spars consisting of shear webs and angle clips, but with current manufacturing methods these spars are often made as one integral structure not requiring additional joints. In-plane stresses are also observed between skin and stiffener in skin-stiffened panels loaded in shear and at stiffener terminations when loaded in tension.

In 1988 *Niu* [7] published data on a range of aircraft types, listing stiffener shapes used in the fuselage, wings and empennage. This data showed that in fuselages commonly omega stiffeners are used, while in wings and tail sections simpler shapes, such as Z-stiffeners, are more prevalent. Also, in aluminium wing and tail sections, integral skin-stiffener structures, where the skin and stiffener web are machined from one block of material, are sometimes used. He noted that simpler composite stiffeners with only one flange in contact with the skin, such as L-, C- and Z-stifeners, should be avoided when no measures are taken to alleviate stress concentrations, because they are more prone to delaminations starting under the stiffener radius [37]. However, such stiffeners are easier and cheaper to manufacturing and join than the more complex T-, J- and omega stiffeners [38]. Because thermoplastics can be reformed at elevated temperatures, stiffeners with simple shapes can be press formed from flat laminates relatively cheaply and quickly, so it would be valuable to develop an design in which simple stiffeners can be used.

Because the focus in this thesis is on the joint performance and testing methodology of skin-stiffener joints with stiffeners that can be press formed in one step, this research is mainly applicable to wing and empennage structures.

2.4. Shear Joints

Shear strength is an important design allowable for joints in aircraft structures. Testing methodologies used in standards and literature are given in Section 2.4.1 and important geometric and material parameters that influence joint performance are discussed in Section 2.4.2.

2.4.1. Testing Methodologies

The most common test for determining lap-shear strength (LSS) of welded TPC joints is the single-lap shear test. Various standards have been developed, but all of these were designed for adhesively bonded joints. Some of the American Society for Testing and Materials (ASTM) standards are outlined below:

ASTM D1002 [39] – standard test method for apparent shear strength of single-lap-joint adhesively bonded metal specimens by tension loading (metal-to-metal): [40–47]

ASTM D3163 [48] – standard test method for determining strength of adhesively bonded rigid plastic lap-shear joints in shear by tension loading: [40, 49]

ASTM D5868 [50] – standard test method for lap shear adhesion for fiber reinforced plastic (FRP) bonding: [28, 51, 52]

Because no standards exist for welded TPC joints, procedures in the above mentioned standards are often modified to suit the material and joining method. For example in literature, differences can be found in loading rate, ranging from 0.5 mm/min [42] to 13 mm as recommended in ASTM D5868. *Dubé et al.* [53] used the double-lap shear test, according to ASTM D2528 [54], to determine joint strength of resistance welded TPC joints. Other standardized lap-shear tests are: ASTM D3165, ASTM D5656, ISO 4587:2003, ISO 9664, ISO 11003-2 and AITM 1-0019.

Tserpes et al. [55] developed an experimental rail shear setup for measuring shear strength of skin-stiffener joints, as shown in Figure 2.3. In their research an adhesively bonded CF/epoxy T-joint was tested, but this setup would also be applicable to induction welded L-joints. The main advantage of this setup is that load cases in actual shear loaded skin-stiffener joints in aircraft structures can be approached. The specimen configuration can be the same as a small section of a stiffened panel, for example in a wing or stabilizer. Disadvantages, however, are that the coupons and tooling are more time consuming and expensive to manufacture, compared to the lap-shear test and simulating this joint using finite element analysis would be rather complex.

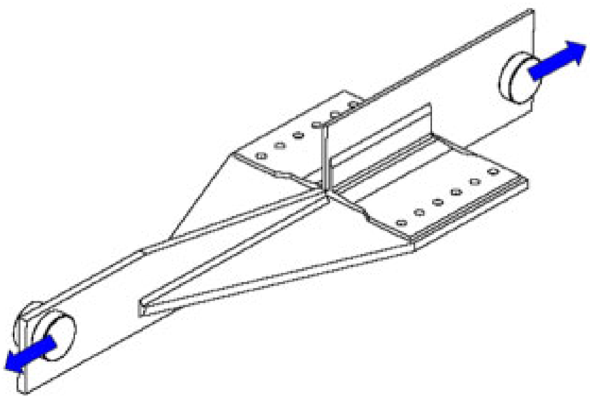

Figure 2.3: Rail shear test setup for skin-stiffener joints [55].

Various researchers have developed a setup for testing joints under in-plane, out-of-plane and mixed mode loading. This Arcan test setup, shown in Figure 2.4, has been used for bolted joints [56], friction stir welded aluminium joints [57], clinched sheet metal joints [58] and adhesive bonds [59–61]. This method can potentially be modified to also accommodate skin-stiffener joints. Pure in-plane loading would then be comparable to the load case as shown in Figure 2.3 and pure out-of-plane loading to a regular pull-off setup.

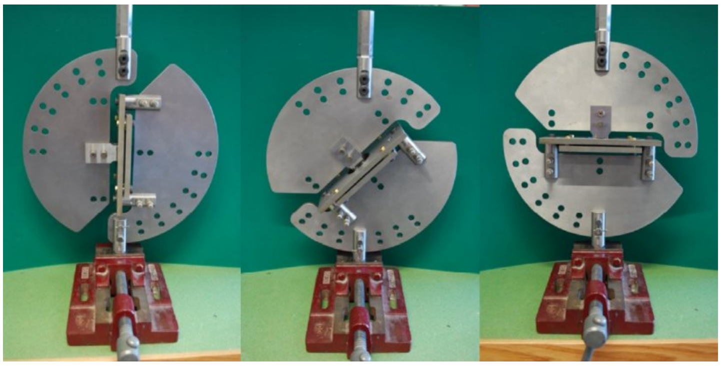

Figure 2.4: Arcan test setup for shear, pull-off and mixed loading [56].

2.4.2. Influential Parameters

Banea and Da Silva [62] and *Budhe et al.* [63] developed a comprehensive overview of the influence of various geometric and material parameters on the performance of adhesively bonded shear joints. It has been shown repeatedly that applying an outside taper or adhesive fillet to a lap shear joint, items 2 and 4 in Figure 2.5, respectively, greatly reduces out-of-plane stresses in the interface layer and increases joint strength [64–70]. *Shi et al.* [71] reported up to a 87% LSS increase when an epoxy adhesive fillet was used in a resistance welded thermoplastic joint. This shows that while thermoplastics are known for poor bonding characteristics, an adhesive fillet can improve joint performance. Tapering joints before induction welding is preferably avoided, because in order to apply sufficient pressure in the entire weld region more complex tooling is required. Also, less heat is generated in the weld under the tapered region, because less material is present.

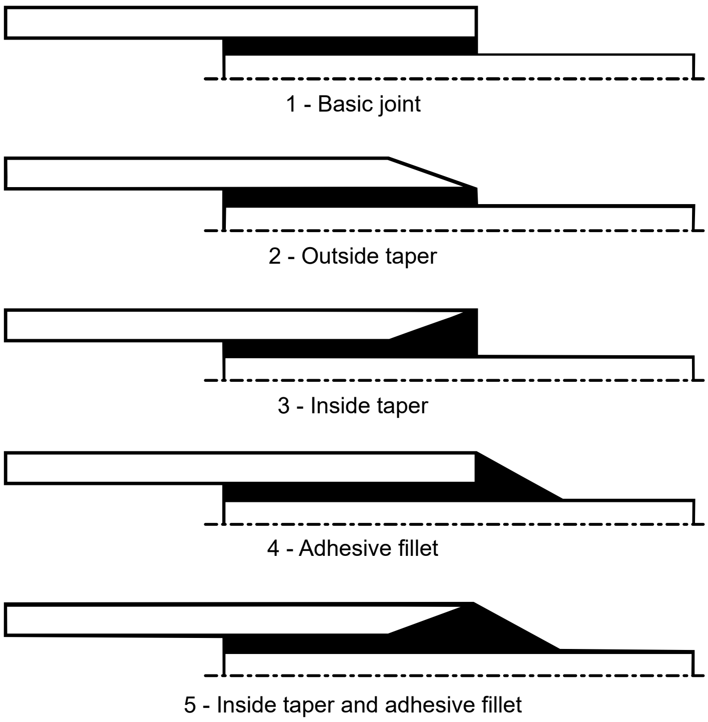

Figure 2.5: Lap joint taper designs. Adapted from [72].

Numerous studies [63, 66, 73–78] have been performed to study the effect of overlap length on single-lap joint performance. These studies showed that increasing the contact area results in a stronger joint up to a limit, depending on adherent and adhesive material. However, this performance increase is not proportional with the extra overlap needed. While for adhesive bonding the overlap length can easily be adjusted, for induction welding this is dependent on process settings, coil geometry and material properties and geometry.

Lionetto et al. [79] measured a 22% higher LSS in induction welded CF/PEEK coupons with a PEEK film placed between the laminates, compared to when no additional film was used. *Sacchetti* [80] also measured a higher fracture toughness in CF/PEEK joints with increased thickness of the resin rich interface. These studies show that through a relatively simple additional process step, induction welded joint performance can be improved, for both in-plane and out-of-plane loading.

The cooling rate in the induction welding process can also influence joint performance. *Gao and Kim* [81] showed that a higher cooling rate leads to a lower degree of crystallinity for PEEK, resulting in a lower tensile strength and elastic modulus. *Choupin* [82] observed the same for PEKK. On the other hand, several studies [80, 83, 84] found that a lower degree of crystallinity, thus a higher cooling rate, increases fracture toughness of the thermoplastic material. Generally a high degree of crystallinity is preferred, also due to improved moisture, chemical and thermal resistance [85], but it could be worth investigation if a lower cooling rate results in an increase in pull-off joint performance, due to increased fracture toughness.

2.5. Pull-off Joints

Most studies on joint performance of welded TPC joints are about shear loading, but research is available that is valuable for improving induction welded L-joints. In Section 2.5.1 testing of out-of-plane joints is reviewed and in Section 2.5.2 important geometric and material parameters affecting joint performance are discussed.

2.5.1. Testing Methodologies

No standardized test methods exist for determining pull-off strength of skin-stiffener joints. In industry, company-specific tests are performed and in literature a range of different setups and coupon geometries are used. Most of these studies are on T-joints and only limited research is available on L-joints.

Pappadà et al. [28, 52] tested induction welded TPC L-joints, where the skin was simply supported and a pulling force was applied to the stiffener. The coupons were narrow with a width of only 23 mm and the skin laminate was only 1.2 mm thick. Also, the distance between the skin supports was only 50 mm. *Feih and Shercliff* [86] performed pull-off tests on adhesively bonded TSC L-joints and a coupon width of 70 mm was used with a skin and L-piece thickness of 10 mm and 3.7 mm, respectively. The skin was clamped at its edges with a grip separation of 145 mm. As can be noted from these studies, there is no consensus on what coupon geometry to use and therefore it is hard to directly compare results in literature.

2.5.2. Influential Parameters

Sápi et al. [87] published a literature study on the effect of various geometric parameters and design choices on the pull-off performance of skin-stiffener joints. Some studies on T-joints [88, 89] have shown that minimising bending of the skin laminate by increasing skin thickness or reducing the distance between grips, leads to a higher joint strength. By limiting bending of the skin laminate, peeling effects between the skin and stiffener are reduced.

Haugen [90] noted that for T-stiffeners subjected to pull-off loading, increasing the stiffener flange thickness will at some point cause the joint to fail at the stiffener flange tip instead of under the stiffener radius, due to high geometric stiffness discontinuity. Stresses at the flange tip have been studied [91, 92] and several researches [93–96] have demonstrated that tapering the flange in a similar way as shown in item 2 in Figure 2.5 reduces interlaminar shear and out-of-plane stresses and improves joint strength. In case of induction welded skin-stiffener joints this taper should preferably not be applied before welding, due to issues with pressure application and heat generation, as discussed in Section 2.4.2.

In TSC T-joints the region between the skin and stiffener radii is filled with some material. Commonly UD tape or resin film is rolled and then formed in an open tool [97]. Some other options of producing such fillets are pultrusion of continuous fiber reinforced material, injection molding of neat or short fiber reinforced resin and hand layup [87]. Also, an adhesive fillet can be applied after the joining process and can be used for a wide range of skin-stiffener joints, including L-joints.

Feih and Shercliff [86] showed that adding an adhesive fillet to a TSC L-joint can increases joint strength significantly. In Figure 2.6 two of the four tested fillet geometries are shown. Although adhesives are generally not well compatible with thermoplastic composites, it has been shown that an adhesive fillet can increase lap shear strength, as discussed in Section 2.4.2 [71]. For this reason, it would be worth investigating if an adhesive fillet can increase pull-off performance of induction welded TPC L-joints. Another option would be to implement a thermoplastic resin fillet of the same material as used in the laminates, but no literature has been published using this approach. Potentially this fillet can be joined to the skin and stiffener during the induction welding process or otherwise it can be joined to the stiffener before welding. Possible options for producing this fillet could be additive manufacturing or machining from stock material.

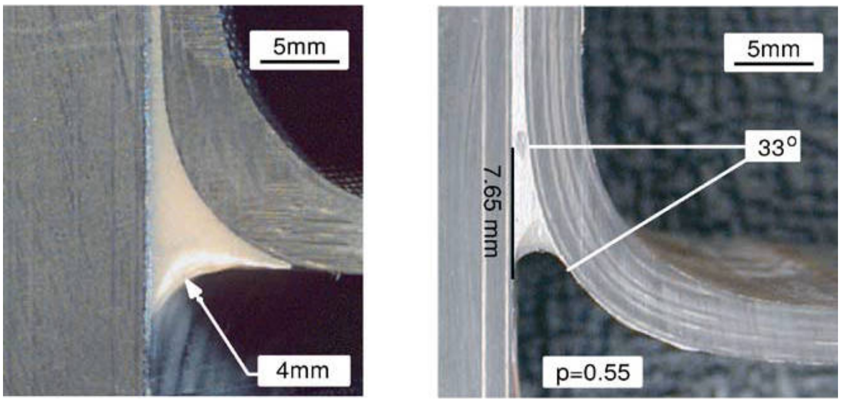

Figure 2.6: Adhesive fillet in CF/epoxy L-joint [86].

Van Ingen et al. [5] observed that for induction welding of L-joints, the coil position with respect to the stiffener radius influences joint performance. They showed that pull-off strength is improved when the coil and therefore the welded region is closer to the stiffener radius. If a thermoplastic resin fillet would be used during welding, as discussed in the previous paragraph, the coil must be moved further toward the stiffener radius and the effect of this on joint performance should be investigated.

Hoffmann et al. [98] investigated z-pinning of TPC joints. Z-pinning is a through-thickness reinforcement approach for increasing pull-off strength of composite joints, where rods, made of a high-strength and high-stiffness material, are inserted in the through-thickness direction of a laminate. They were unsuccessful in increasing joint performance using this method and attributed it to insufficient bonding and friction between the laminate and pins.

2.6. Fracture Mechanics

Based on previous experiments at KVE and in literature, it is expected that pull-off coupons in this thesis will fail between the skin and stiffener radius due to high localized stresses and failure will propagate along the weld line. In Section 2.6.1 a brief overview on fracture mechanics will be provided, followed by fracture analysis in section 2.6.2. This is concluded with a discussion on fatigue crack growth in section 2.6.3.

2.6.1. Overview

In 1913, *Inglis* [99] published a paper on quantifying stresses around holes and corners and in 1921, *Griffith* [100] applied this work to develop an energy balance criterion around cracks, based on the principle of minimum energy. This criterion describes that a crack will propagate once the strain energy release rate (SERR) G, the potential energy dissipated during fracture, is equal to or exceeds a critical value G_c [101]. The value of G is dependent on specimen geometry and applied loading, while G_c is regarded as a material property, the ability to resist delamination.

For composite materials three delamination failure modes are defined: mode I (tension), mode II (sliding shear) and mode III (scissoring shear). In Figure 2.7 an illustration of these failure modes is shown. A composite material has a critical G_c value for each of these modes and this value is dependent on many factors, such as resin quality, fiber volume fraction, void content, laminate stacking sequence, loading rate and temperature.

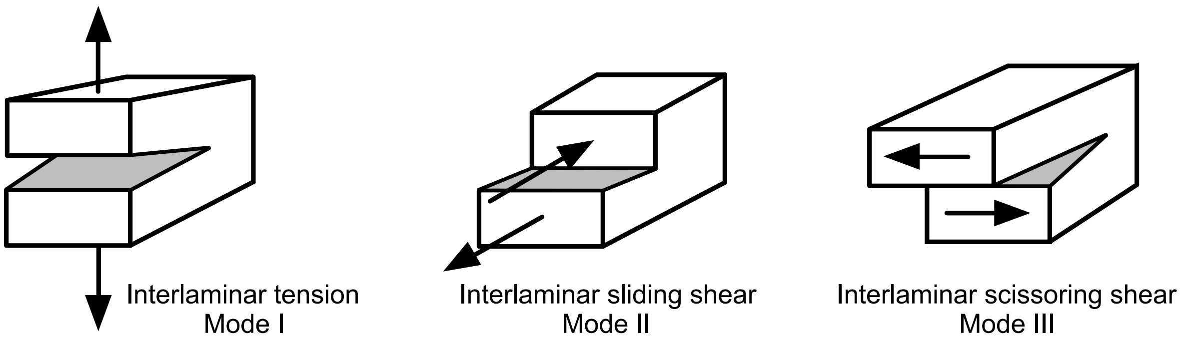

Figure 2.7: Composite delamination modes. Redrawn from [102].

An L-joint under pull-off loading, as studied in this thesis, will predominantly be subjected to mode I, interlaminar tension, and to a smaller degree to mode II, interlaminar sliding shear. For some composites, such as CF/PEEK, critical SERR values are reported in literature [103, 104], but for the material used in this thesis, CF/PA11, this is not available. Also, scatter among SERR values reported in literature is high.

2.6.2. Fracture Analysis

For predicting delamination fracture in composite materials, usually either the virtual crack closure technique (VCCT) [10] or the cohesive zone model (CZM) [105] is used. While VCCT relies on the theory discussed in the previous section, CZM is based on the principle of damage mechanics and is particularly useful when the crack path is unknown. Because data required for this method is difficult to obtain and the crack path is know, only VCCT will be discussed.

VCCT is a method to compute SERR for the different modes shown in Figure 2.7 using finite elements and is based on the assumption that the energy released by opening a crack by a small length is identical to the energy required to close the crack of this same length behind the crack tip. The critical value G_c is determined through testing of the composite material. Tests are performed for pure mode I, pure mode II and mixed mode I and mode II loading. From these results a failure criterion is constructed with a critical value G_c for any ratio of mode I and mode II loading at the crack tip, as shown in Figure 2.8 for a typical thermoset composite. Once the calculated SERR G, which is defined as $G = G_I + G_{II} + G_{III}$, exceeds the critical value G_c, the crack is propagated to the next node in the predefined crack path. Pure mode I data is found using the double-cantilever beam (DCB) test and pure mode II data can be obtained using the end-notched fixture (ENF) test. For mixed-mode I and II the mixed-mode bending (MMB) test can be used. Illustrations of these tests are shown in Figure 2.8.

2.6.3. Fatigue Crack Growth

Because joints in aircraft structures are subjected to cycling loading, an approach for analyzing fatigue delamination crack growth is desired. During cycling loading, delamination growth can occur below the critical G_c value. For stable fatigue delamination growth, the crack growth rate can be described using the Paris law [11], a power law function, which is defined as:

$$\frac{\mathrm{d}a}{\mathrm{d}N} = c \cdot G_{\mathrm{max}}^{n} \tag{2.1}$$

where $\mathrm{d}a/\mathrm{d}N$ is the crack growth rate defined as crack length increase, $\mathrm{d}a$, per cycle, $\mathrm{d}N$. G_{max} is the strain energy release rate at the crack tip at peak loading and c and n are constants obtained from experimental data. Below a certain threshold G_{th} value, no crack growth occurs. In Figure 2.9 an example is shown, where the crack growth rate is plotted as a function of G_{max}.

Krueger [11] stated that this approach should only be used for pure mode I loading, but since the L-joint will predominantly be loaded in mode I, it can possibly be used for predicting fatigue life of the skin-stiffener joint. As will be discussed in Section 5.3.2, the contribution of modes I and II are dependent on joint geometry and crack length.

2.7. Concluding remarks

In this chapter several topics related to testing and performance of induction welded joints, with in particular skin-stiffener joints, were discussed. Literature showed that induction welding of TPCs has great potential for the use in primary aircraft structures. However, quicker and more cost-effective production methods are desired. A sizeable amount of research has been performed on in-plane shear joints, also for induction welding, but research on out-of-plane loading is lacking. For this reason in this thesis the focus will be on pull-off loading of skin-stiffener joints.

L-stiffeners and other stiffeners with a simple geometry are particularly interesting for TPCs, because of the relatively quick and low-cost hot press forming process for creating these profiles. However, for highly loaded joints this stiffener shape is not recommended, because of high localized stresses under the stiffener radius, promoting delamination. It was shown for adhesively bonded TSC L-joints that this stress concentration can be reduced and joint strength greatly increased by applying an adhesive fillet [86]. Also for thermoplastic single-lap shear joints it was shown that joint strength can be improved by applying an adhesive fillet [71]. Based on these results an attempt will be made in this thesis to improve induction welded TPC pull-off performance of L-joints by implementing a fillet.

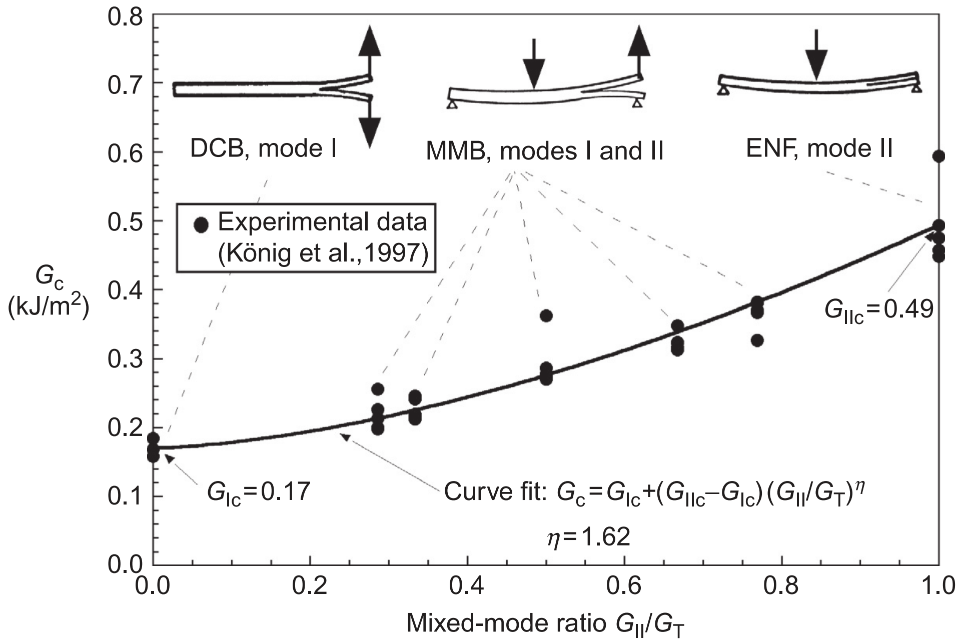

Figure 2.8: Example of critical strain energy release rate fracture criterion for a typical carbon/epoxy material, T300/914C [11]. 1 kJ/m² = 1 N/mm

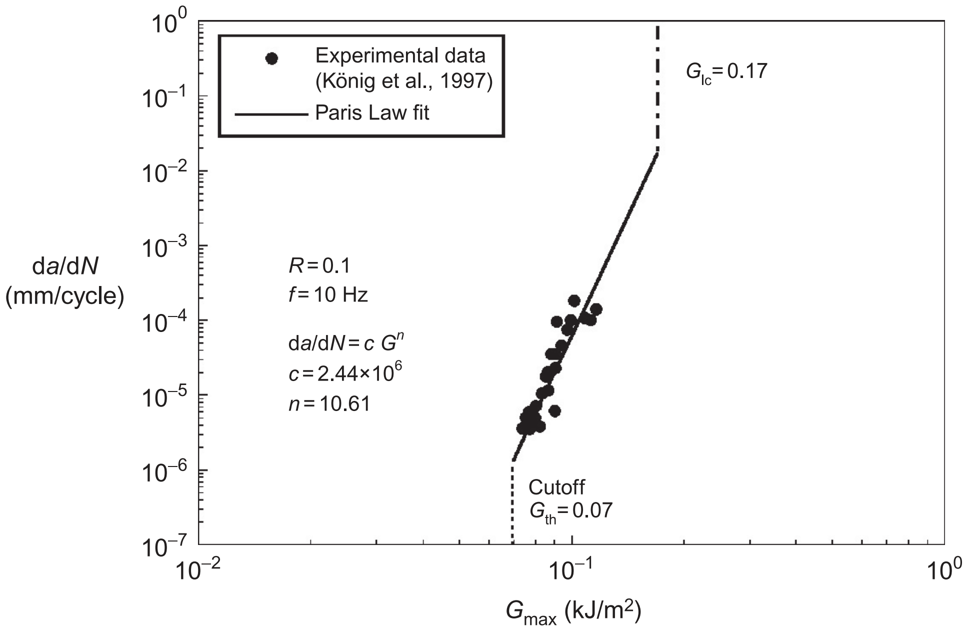

Figure 2.9: Example of fatigue crack growth for a typical carbon/epoxy material, T300/914C [11].

3

Methodology

In this chapter the research methodology is explained. First in Section 3.1 the material selection is discussed and is followed by the joint design in Section 3.2. This contains the selected baseline joint geometry, as well as measures to improve joint performance. In Section 3.3 the welding setup is described and in Section 3.4 the design of a modified pull-off test setup is explained.

3.1. Material Selection

There are four high-performance thermoplastic resin materials used in TPC structural aircraft components: PEKK, PEEK, PPS and PEI. Due to the high cost of these materials, in this thesis a cheaper material was used instead. Several UD CF reinforced nylon/polyamide (PA) composite tapes from different suppliers were looked at and after a trade-off on cost, availability and material properties, two materials were further investigated: CF/PA11 from TenCate Advanced Composites and CF/PA12 from Evonik. The PA11 material had previously been used at KVE for induction welding and showed good welding characteristics and for the PA12 material, laminates were manufactured for a welding test. This test showed that this material requires almost twice the amount of power compared to the PA11 material to reach the same temperature and a temperature increase was observed throughout the laminate, while a more localized heat generation is desired. Based on this study, the TenCate CETEX TC900 CF/PA11 material was selected for this thesis. In Table 3.1 the most important properties of this UD tape material are shown, as well as CF/PEKK for comparison.

Differences can be observed in the properties table, of which the most notable are the tape thickness, fiber volume fraction, glass transition temperature and melting temperature. However, from previous experiments at KVE and from preliminary simulations it had been found that the way the material heats up during induction welding was comparable. The heating pattern around the coil was similar, which for example for the tested CF/PA12 tape was not the case. The relatively low melting temperature of the PA11 material was beneficial for this thesis, because it allowed for quicker processing and for cheaper consumables.

Critical strain energy release rate values for CF/PA11 are not available in literature. Because G_{Ic} in particular is important for accurate finite element analysis of the L-joint, this value was determined experimentally using the double cantilever beam test, according to ASTM D5528-13 [103]. The production of these samples is described in Section 4.2 and the results can be found in Section 5.1.

3.2. Joint Design

Some design parameters in the baseline L-joint were determined from the available tooling, while other parameters were chosen based on industry best practices. This decision process is described in Section 3.2.1. This is followed by a discussion on the implementation of a fillet in the L-joint in Section 3.2.2.

Table 3.1: Material properties of CF/PA11 [12] and CF/PEKK [13].

Property	Units	CF/PA11	CF/PEKK
Material density ρ	g/cm^3	1.36	1.59
Ply thickness t_{ply}	mm	0.20	0.14
Fiber volume fraction V_f	%	45[a]	59[a]
Fiber weight fraction W_f	%	59	66
Glass transition temperature T_g	°C	42	159
Melting temperature T_m	°C	183	337
Longitudinal modulus E_{11}	GPa	106	139
Transverse modulus E_{22}	GPa	9.8[b]	10.3
In-plane shear modulus G_{12}	GPa	4.0[c]	5.2
Poisson's ratio ν_{12} and ν_{13}	—	0.28[c]	0.30[c]
Poisson's ratio ν_{23}	—	0.40[c]	0.45[c]
Longitudinal tensile strength σ_{11}	MPa	1641	2460
Transverse tensile strength σ_{22}	MPa	48[d]	61
In-plane shear strength τ_{12}	MPa	85	52.4
Critical mode I strain energy release rate G_{Ic}	N/mm	—	1.33[e]
Critical mode II strain energy release rate G_{IIc}	N/mm	—	2.0[c]

[a] Calculated using the mixture rule.
[b] Calculated using Halpin–Tsai model.
[c] Assumption based on thermoplastic composite data in [106].
[d] Tensile strength of neat PA11 resin [107].
[e] Assumption based on AS4/PEEK round-robin test data as reported in ASTM D5528-13 [103].

3.2.1. Baseline Specimen

The baseline specimen design parameters are listed in Table 3.2. The thickness of the stiffener and the radius dimension were required as such, because of the already existing tooling used for press forming of the profiles. The flange length was limited at 25.4 mm (1 inch), because of the induction welding setup used. Because it was expected that the joint would fail between the skin and stiffener at the radius section, where the stress concentration is highest, the flange length was not very important, as long as it was at least as wide as the weld bath. Based on previous experience at KVE, the weld would be less wide than 25.4 mm.

The skin thickness and web height were based on discussion in literature [38] and on weld tooling constraints. Because the height of the stiffener was limited to 100 mm in the weld tooling and approximately 50 mm would be needed for sufficient grip during mechanical testing, a baseline height of 50 mm was selected. A quasi-isotropic layup was chosen for the skin laminate and a 45°-dominant stacking sequence for the stiffener. More 45° plies in the stiffener web increases in-plane shear stiffness and bending stiffness in a skin-stiffened panel. 45° plies were placed on the outside, as is recommended for aircraft structures for better damage resistance [38], and the skin and stiffener were placed with the outside 45° plies perpendicular to each other to improve heat generation in this region during welding.

As stated by *Kassapoglou* [38], a common stiffener spacing in aircraft structures is 150–160 mm and by placing a fixed constraint on the skin 160 mm apart this feature was replicated. A coupon width of 50 mm was chosen so that six test samples and one or two microscopy samples could be created from one welded joint. Six samples should be sufficient for obtaining statistically relevant data.

Table 3.2: Baseline L-joint coupon design.

Property	Units	Baseline
Skin stacking sequence	—	$[\pm45 / 0 / 90 / \pm45 / 0 / 90 / \bar{0}]_S$
L-stiffener stacking sequence	—	$[\mp45 / 0 / \mp45 / \overline{90}]_S$
Coupon width	mm	50
Skin thickness	mm	3.4 (17 plies)
Stiffener thickness	mm	2.2 (11 plies)
Distance between grips	mm	160
Flange length from radius	mm	25.4
Web height from skin surface	mm	50
Stiffener inner radius	mm	3.05

3.2.2. Fillet Specifications

As discussed in Section 2.7, the effect of a fillet between the skin and stiffener radius was investigated during this thesis. An illustration of this fillet is shown in Figure 3.1. In the paper by *Feih and Sher-cliff* [86] several fillet sizes were investigated, of which two are shown in Figure 2.6, and it was found that pull-off strength was improved for increased fillet size. In this thesis several techniques were used to manufacture the fillet and for most of these techniques a sufficiently large cross-section was required. On the other hand, increasing the fillet size would increase the area to be welded and would require the coil to be placed further toward the fillet during welding, resulting is a larger unwelded flange section. As a trade-off between these conflicting requirements, the fillet radius was chosen as 2 mm.

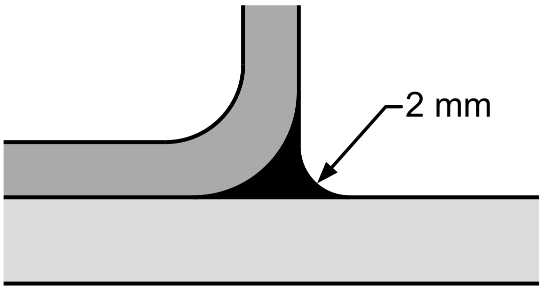

Figure 3.1: L-joint fillet shape

Eight different fillet types and manufacturing methods were considered, which are listed in Table 3.3. Fillets 1–5 were produced and an attempt was made to fabricate a laminate from chopped tape for fillet 6, but this was unsuccessful. Although fillet 5 was produced, it was not used for further tests, because it had poor strength in the vertical direction and peeled easily.

Earlier experiments at KVE had shown that different nylon materials can be blended and therefore nylon types other than PA11 were considered. The PA11 fillet made through selective laser sintering had a melting temperature of 201°C [107], while the PA12 variant had a melting temperature of 176°C [108]. A lower melting temperature in the fillet could be useful in obtaining a good weld. At the skin-stiffener interface more material was available for heat generation than in fillet region and therefore it could be expected that the fillet would be subjected to lower temperatures.

The adhesive material for fillet 4, Araldite 2048-1, was chosen for its good gap filling ability, its relatively low stiffness and large elongation at break. Fillet 7 was not produced, because a neat PA11 fillet could already be made cheaper and quicker by 3D printing and short fiber reinforced nylon was not easily available. Another method for producing short fiber reinforced nylon was the PRIM, Printed Injection Mould, technology by Promolding [109]. With this technology a mold is 3D printed, which is

Table 3.3: Fillet manufacturing methods that were considered. Fillets 1–4 were fabricated and implemented.

Fillet	Manufacturing method
1	SLS 3D printed PA11
2	SLS 3D printed PA12
3	Machined quasi-isotropic CF/PA11 laminate
4	Adhesive: Araldite 2048-1
5	3D printed (very) short fiber reinforced PA12
6	Machined CF/PA11 laminate from chopped tape
7	Machined neat or (very) short fiber reinforced PA11
8	PRIM short fiber reinforced PA6

then used for injection molding to create the product. This fillet was not produced, because of the high cost for very small batches compared to some of the other techniques.

In Table 3.4 the most important properties of fillets 1–4 are given. Fillets 1 and 2 had similar mechanical properties, but the PA12 material was less flexible and had a lower melting temperature. Compared to the neat resin material, the stiffness and strength of the quasi-isotropic composite material was much higher, but the maximum strain was very low. The adhesive fillet had a lower stiffness and tensile strength than the neat PA11 material, but it could plastically deform significantly.

Table 3.4: Fillet material properties.

Property	Unit	Fillet 1 [107]	Fillet 2 [108]	Fillet 3 [12]	Fillet 4 [110]
Density ρ	g/cm^3	0.99	0.93	1.36	1.0
Melting temperature T_m	°C	201	176	183	—
Young's modulus E	GPa	1.6	1.7	43[a]	0.36
Tensile strength σ	MPa	48	50	540[b]	13
Elongation at break ϵ_T	%	45	20	1.4[c]	91

[a] Calculated from skin laminate stacking sequence.
[b] From experimental data of quasi-isotropic CF/PA6 material with similar UD properties [111].
[c] Assumption based on other thermoplastic composites with the same fiber type [106].

In this thesis three methods for attaching fillets 1–3 were considered. Initially, attempts were made to place the skin, stiffener and fillet in the weld tooling separately, but insufficient heat was generated between the fillet and stiffener radius. For the next two approaches the fillet was attached to the stiffener before welding using a hot air tool. A further explanation of the procedure is given and micrographs are shown in Chapter 4 and test results are discussed in Chapter 5. The results were compared to an autoclave co-consolidated joint with a 3D printed PA11 fillet.

3.3. Welding Setup

The weld tooling was developed by KVE and a photo of the setup is shown in Figure 3.2a. A schematic of the tooling is given in Figure 3.2b. Two pressure bellows pushed the skin, stiffener and fillet, if used, together, after which an induction coil moved along the weld, heating up the material. A passive KVE-patented heat sink was positioned between the coil and laminate, in order to prevent the skin surface from overheating.

(a)

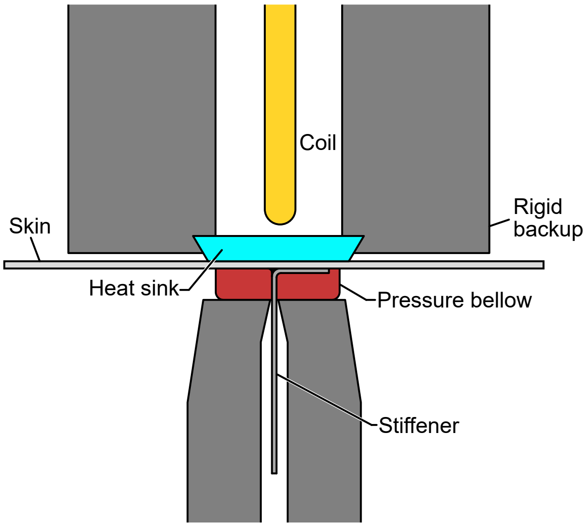

(b)

Figure 3.2: (a) Induction welding setup [112]; (b) Schematic of the weld tooling.

The main input parameter for this system was electric current with a maximum of 700 A and frequency was automatically regulated by the generator for maximum efficiency. This frequency was dependent on the laminate material, as well as the geometry and temperature of the workpiece. The coil speed, the speed at which the coil moves over the joint, could also be adjusted. The coupling distance, the distance between the coil and laminate, and pressure could also be changed, but these were kept constant during this thesis. These were chosen based on previous experience at KVE.

3.4. Pull-off Test Setup

As discussed in Section 2.6.1, no standardized tests are available for pull-off loading of skin-stiffener joints. In literature, most commonly these joints are loaded as shown in Figure 3.3, where the skin is fixed and the web is clamped preventing horizontal displacement and rotation [86, 113–116].

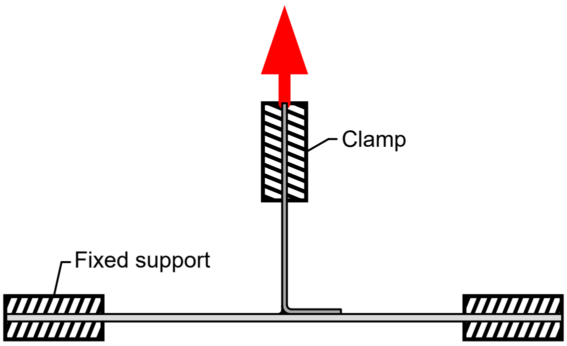

Figure 3.3: Pull-off test setup commonly used in literature.

There are a number of disadvantages with this setup, though. While T-joints behave mostly symmetrically under pull-off loading, an L-joint does not. Asymmetric bending occurs in the skin, because the stiffener flange adds stiffness off-center to the horizontal section. Also, the stiffener web bends during loading. Therefore, clamping the web and preventing rotation leads to additional internal moments and stresses in the joint. In a skin-spar or skin-rib joint, the web extends to the adjacent skin and can indeed be approached by this clamped boundary condition, but in the case of skin-stiffener joints this is different. The highest pull-off loading in a skin-stiffened panel can be expected away from other stiffening elements, such as ribs, and in case of skin buckling or pressure pillowing, stiffeners with limited torsional stiffness can experience some twisting and bending. In case of the setup shown in Figure 3.3, no such deformation at the top of the stiffener web is possible.

Furthermore, L-joints are more likely to encounter spring back in the stiffener during production compared to T-joints, due to its asymmetric geometry. For joints in aircraft structures this spring back angle should be below a specified tolerance, but in the case of research studies a larger deviation could be acceptable. For example, in this thesis in the worst case a deviation of 3.5° from a perfect right angle was measured. Using the setup as shown in Figure 3.3 would lead to additional internal stresses, because the stiffener web should be bent in order to place the joint in the grips correctly. A sensitivity study was performed using the finite element model, as further described in Section 5.3.1, on the influence of the stiffener spring back angle on the pull-off strength of the baseline joint in Table 3.2. A setup in which the stiffener web was clamped, as shown in Figure 3.3, was compared with a setup where the top edge of the web was free to rotate. As shown in the graph, the failure load using this new setup was less sensitive to deviations from a perfect 90° angle between the skin and stiffener web than the more commonly used setup. While for the first setup the highest strength value in the plot is 37.8% more than the lowest, for the new setup this is only 3.7%. This means that more consistent results can be obtained despite spring back in the stiffener.

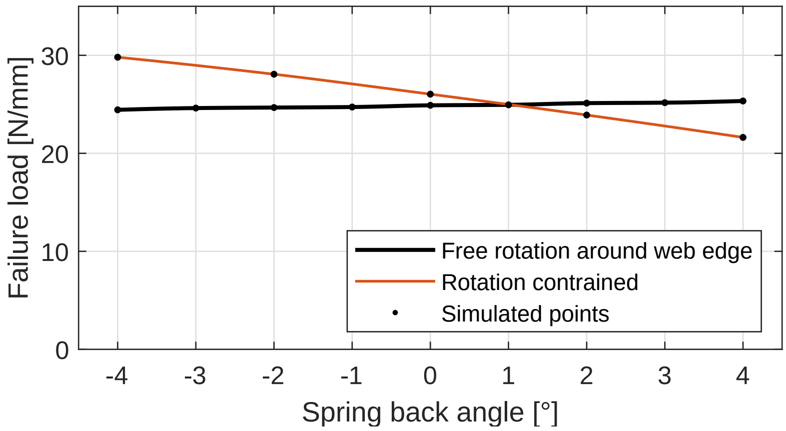

Figure 3.4: The effect of stiffener spring back angle on the failure load for the baseline joint geometry, as given in Table 3.2, for the test setup without (Figure 3.3) and with (Figure 3.5) free rotation around the stiffener top edge. A positive angle means that the angle between the stiffener flange and web is larger than 90°.

For these reasons, the pull-off test setup was modified, as shown in Figure 3.5. A pivot axis was implemented at the web height of 50 mm, as defined in Table 3.2, and vertical loading was to be applied at this axis. The design of this setup also allowed for horizontal repositioning of this axis by using shims. Moving this pivot axis with respect to the stiffener web could be useful if finite element analysis on a skin-stiffener panel shows that in the joint section with the highest pull-off loading an additional internal bending moment is present due to, for example, twisting of the stiffener. Moving of the loading axis or FE analysis on a skin-stiffener panel had not been performed and was outside the scope of this thesis.

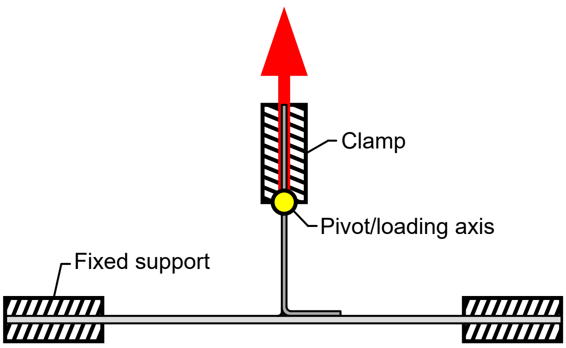

Figure 3.5: Pull-off setup developed for this thesis.

4
Production

In this chapter production processes used during this thesis are outlined. In Section 4.1 the fabrication of laminates used for the DCB test and the L-joint is described, followed by a further discussion on the DCB test coupons in Section 4.2. In Section 4.3 the various procedures associated with creating the L-joints are given, including fillet implementation and induction welding. This chapter is concluded with the new test setup design in Section 4.4.

4.1. Laminates

The unidirectional CF/PA11 tape material, of which the properties are given in Table 3.1, was provided in 50 mm wide rolls. From these rolls, laminates were made by stacking the tape in the orientations defined in Table 3.2 for the skins and stiffeners and unidirectional for the DCB samples. This procedure is described in Section 4.1.1. Following this, the laminates were consolidated in a hot press and this processing step is discussed in Section 4.1.2.

4.1.1. Preparation

The maximum laminate size that could be produced with the available tooling was 475 by 475 mm. Laminates for the stiffener were made at this size, from which two stiffeners could be created and the skin laminates were made at 475 by 300 mm. Tape was cut using a paper cutter and with a soldering iron with a flat tip the material was joined to form plies. The seams between the tapes were visually inspected to ensure no layers overlapped. These plies were then thoroughly cleaned with acetone, aligned and connected at two corners on one side with a sonotrode. After this, the laminates were wrapped in paper until they were press consolidated to prevent contamination. This way 13 skin laminates and 11 stiffener laminates were produced, as well as 2 laminates for the double cantilever beam test.

4.1.2. Press Consolidation

For press consolidating the laminates, the Joos press in the Delft Aerospace Structures and Materials Laboratory (DASML) at TU Delft was used. The edges of each laminate were wrapped with 75 µm thick aluminium foil in order to prevent squeeze-out and the laminates were placed between two 2 mm thick, 500 by 500 mm steel plates, which were coated with release agent. A first attempt at press consolidation was made at a temperature of 220°C and 10 bar pressure, but the aluminium foil ripped and the material squeezed out of the the tooling.

After this, two layers of aluminium foil were wrapped around the edges instead and the temperature and pressure were lowered to 210°C and 7 bar to reduce flow of the material. The temperature and pressure cycles are shown in Figure 4.1. The temperature was first held at 210°C for 10 minutes to ensure good flow of the resin throughout the laminate, after which pressure was applied until the end of the cycle. The heating rate was set at 7°C/min and the cooling rate at 15°C/min. The press was not able to achieve this cooling rate and required an additional 25 minutes to cool down the tooling to 30°C, after which pressure was removed.

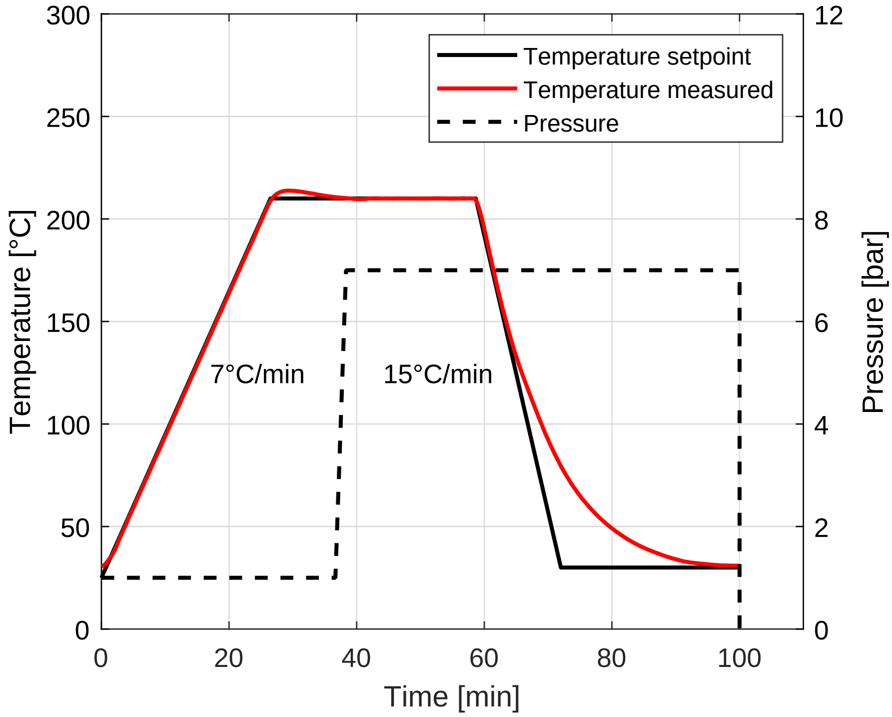

Figure 4.1: Temperature and pressure profile during the hot press cycle for the production of the skin, stiffener and DCB laminates. The Joos press in the DASML at TU Delft was used. The cooling rate of the tooling was lower than defined in the program.

After every second cycle, release agent was reapplied on the steel tool plates. This was not done after every cycle to reduce manufacturing time. The laminate surface of each second laminate was less glossy and a faint white haze was observed, but no detrimental effect on material properties was expected.

4.2. Double Cantilever Beam

The DCB coupons were manufactured according to ASTM D5528-13 [103]. In Figure 4.2a a schematic is shown of how the samples were positioned in a 250 by 250 mm laminate. In this figure, the lighter edge indicate aluminium foil wrapped around the laminate to prevent squeeze-out. In Figure 4.2b the laminate is shown, placed on the bottom steel tool plate before the other plate was positioned on top. The laminate consisted of 20 plies with all fibers in the same orientation, as indicated in the figure, with a 13 μm thick polyimide/Kapton film inserted in the middle in order to create a pre-crack. Release agent was applied to both sides of film. From this laminate 7 samples were created.

The laminate was 4 mm thick and the coupons were 153 mm long and 25 mm wide. The polyimide film was positioned so that the pre-crack was 73 mm long, resulting in a pre-crack of slightly more than 50 mm with respect to the loading axis after loading blocks were bonded to the coupons.

The first attempt at press consolidation of the DCB laminate was unsuccessful due to tearing of the aluminium foil, causing material to squeeze out at the sides. Regardless, coupons were cut from this laminate for testing the bonding procedure of the loading blocks and for trial runs of the DCB test. The second attempt was better, with only limited deformation of the laminate, but fiber waviness was observed, as shown in Figure 4.3a. Because this defect was mostly present some centimeters away from the crack front and because it would only affect two of the samples, this result was deemed acceptable.

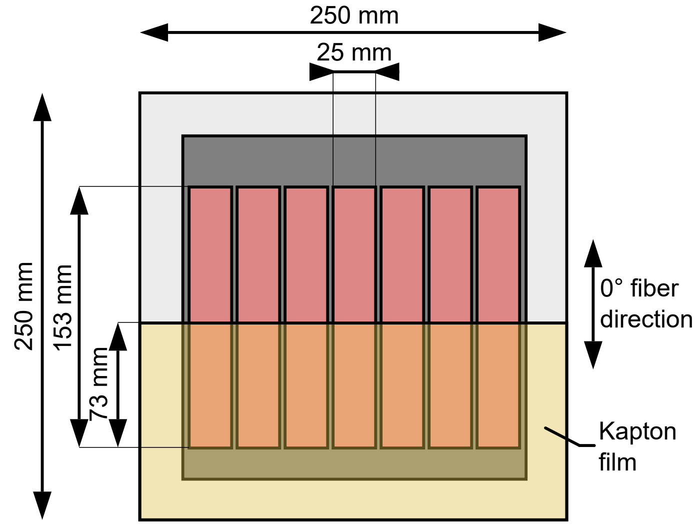

(a)

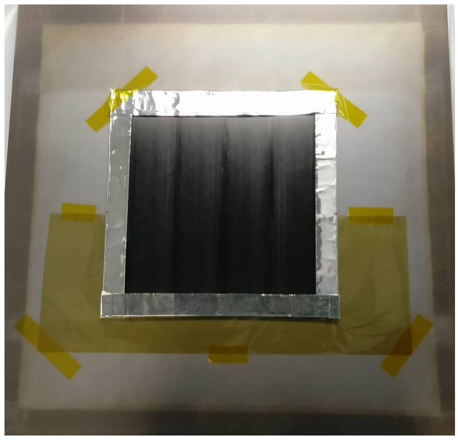

(b)

Figure 4.2: (a) The seven DCB coupons as created from a 250 by 250 mm laminate. A 13 µm polyamide film was used to create a pre-crack in the laminate; (b) The DCB laminate positioned on one of the steel tool plates. The laminate and film were taped to the plate to prevent sliding while in the hot press.

After the laminate was cut using a water cooled diamond blade saw to the dimensions shown in Figure 4.2a, aluminium loading blocks were bonded to the coupons. Because thermoplastics, with in particular nylon, have poor bonding characteristics, additional processing steps had to be taken. Araldite 2011, a two-component epoxy paste adhesive, was used. In a first attempt, the bonding areas of a coupon and loading block were only roughened using 120-grit sandpaper before bonding, but this proved to be insufficient, as the adhesive bond failed before crack propagation of the laminate finished when load was applied.

(a)

(b)

(c)

Figure 4.3: (a) Fiber waviness in the DCB laminate after hot pressing; (b) Jig used for bonding the loading blocks to the coupons; (c) The DCB coupons after the loading blocks were bonded. Samples A2–A5 were made from the first pressed laminate and were not used for determining the fracture toughness of the material.

In a second attempt, the DCB coupons were thoroughly cleaned with acetone, roughened using 120-grit sandpaper and again thoroughly cleaned with acetone, after which they were plasma treated with compressed air in an ambient environment. For this, a 600W Tigres V06 power supply was used with three Tigres Plasma MEF nozzles, positioned in parallel. The DCB laminates were positioned 30 mm below the nozzles on a computer controlled movable surface. This surface moved at 15 mm/s and after each pass it was moved by 8 mm until all bonding surfaces had been treated. The aluminium loading blocks were also cleaned with acetone and one side was sandblasted, followed by another cleaning step. Glass beads with a 0.05 – 0.10 mm diameter were added to the adhesive to create an even thickness distribution across the bond. The coupons were placed in a jig, shown in Figure 4.3b, and a clamp was placed on each specimen to apply pressure on the bond line. The adhesive was cured at room temperature for 5 days and post-cured at 50°C for a further 3 hours. Excess adhesive was then removed using a file and sanding belt. A razor blade was used to carefully remove any adhesive at the sides of the pre-cracked region, without opening the laminate too much and affecting the crack front. The coupons are shown in Figure 4.3c and a schematic of the specimen cross-section is shown in Figure 4.4.

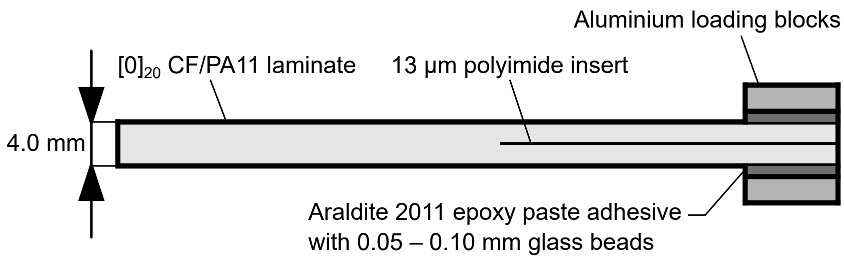

Figure 4.4: Schematic of the DCB coupon cross-section.

4.3. L-joint

The main focus in this thesis was the production and testing of L-joints and this involved various manufacturing steps. In Section 4.3.1 processing of the skin and stiffener laminates is discussed, followed by manufacturing of the fillets in Section 4.3.2 and the implementation of these fillets in the L-joint in Section 4.3.3. The induction welding process for joining the skin and stiffener is reviewed in Section 4.3.4. One joint with neat PA11 fillet was autoclave co-consolidated for comparison with the induction welding process and this is described in Section 4.3.5. Preparation of the coupons for testing is discussed in Section 4.3.6.

4.3.1. Skin and Stiffener

Some fiber waviness was observed in most skin and stiffener laminates, as shown in Figure 4.5. This occurred consistently in the same corner of the laminates and thickness measurements showed that the right side of laminates as seen in the photo were slightly thicker than the left side. This could possibly be caused by misalignment of the consolidation press setup. Because this happened in a corner, this was not a problem, because after welding this edge was trimmed off. Therefore, this fiber waviness was not present in the weld line of the test coupons.

A diamond blade saw was used to cut the skin laminates to a width of 250 mm, removing the aluminium covered long edge as shown in Figure 4.5. These trimmed edges were later reused for the production of a quasi-isotropic fiber reinforced fillet, which is further discussed in Section 4.3.2. Initially, aluminium foil on the short edges was kept in place, with the intention of using them as a method to reduce edge effects during welding, but after this turned out to be ineffective, the foil was removed.

The 10 successfully produced stiffener laminates were cut in half and hot press formed into L-profiles by Dutch Thermoplastic Components (DTC), resulting in 20 stiffeners. One of these stiffeners was found unsuitable for further practical use, because it was pressed in an incorrect orientation and the

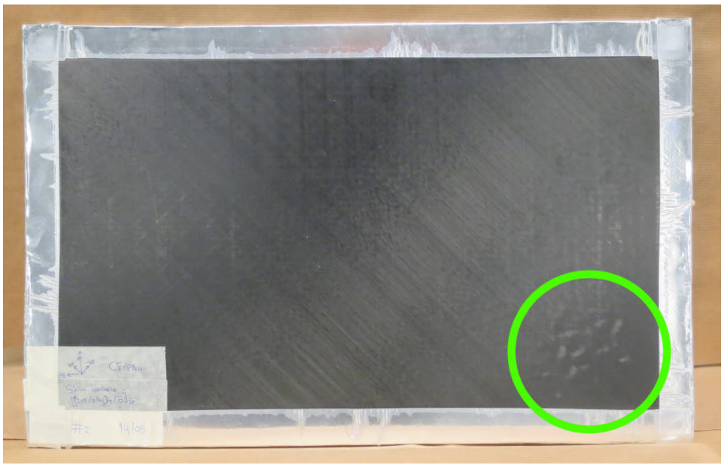

Figure 4.5: Fiber waviness was visible in nearly all skin and stiffener laminates in the bottom right corner, possibly caused by misalignment in the press setup.

surface quality was poor. A varying degree of fiber waviness was observed in the remaining stiffeners and spring-back up to -1° was measured. The stiffener flange was very flat, but the web had bent and twisted slightly during the press forming process. Because this warping had occurred at the sides of the profile, this would fall within the scrapped region after induction welding and was therefore not regarded as a major issue. The L-profiles were sorted into those used for trial welding runs and those for the final runs, based on the amount of fiber waviness, variation in thickness throughout the component and warping.

4.3.2. Fillet

Four different fillet types were developed as explained in Section 3.2.2. Neat PA11 and PA12 fillets were 3D printed using the selective laser sintering (SLS) technique and a fillet was made from quasi-isotropic CF/PA11 material. Also, an adhesive fillet was tested. The fillets were designed to the geometry shown in Figure 3.1. Using the density of the fillet materials listed in Table 3.4 the weight increase with respect to the baseline joint was calculated. For the neat PA11 and PA12 fillets this was 0.47% and 0.44%, respectively. For the composite fillet this was 0.64% and for the adhesive fillet 0.47%.

SLS Printed PA11/PA12

The PA11 and PA12 fillets were printed by Parts on Demand [117], a company specialized in 3D printing of various polymers. Because for the SLS technique a laser is used to sinter powder and fuse it into a structure, corners cannot accurately be created with a smaller radius than that of the laser itself. Regardless, the theoretically exact dimensions were used for printing the fillets and the resulting shapes are shown in Figure 4.6. The fillets were printed at a length of 230 mm, because any longer could potentially lead to warping of the part. This meant that two fillets were needed for each joint. The resulting geometry of the two fillet types was slightly different, with the PA11 variant having sharper corners and being thinner than its PA12 counterpart. The PA11 fillet was more flexible and its surface was smoother. While this component could be bent and twisted without observing any damage, the PA12 fillet would tear when deformed too much. Based on these observations the PA11 variant seemed more practical for this application, because it had a higher resistance to tear, a property desired for preventing failure of the skin-stiffener joint under pull-off loading. Also, during application of the fillet, as described in Section 4.3.3, it was less prone to failure.

Quasi-Isotropic Machined CF/PA11

Quasi-isotropic CF/PA11 fillets were made from trimmed edges of the skin laminates, as mentioned in Section 4.3.1. The aluminium foil was removed and three of these edge strips of equal width were selected. After cutting them to a length of 470 mm, they were placed in a tool. This tool consisting of a

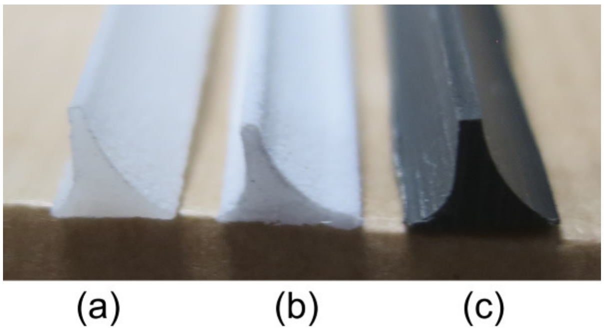

Figure 4.6: (a) PA11 fillet; (b) PA12 fillet; (c) CF/PA11 fillet

steel plate and four aluminium beams surrounding the three stacked strips, connected to the plate using Teflon tape. A thin caul plate was placed on top of the laminate and beams, after which the workpiece was vacuum bagged and oven cured at 210°C for approximately 30 minutes. Following this, two fillets were created from each beam using a CNC milling machine. The resulting parts were trimmed using a knife and sandpaper. The quality of the components varied strongly, so only the best fillet was used for further processing. A CF/PA11 fillet is shown in Figure 4.6.

Araldite 2048-1 tough flexible adhesive

The Araldite 2048-1 adhesive [110] was selected for its good gap filling ability, its relatively low stiffness and large elongation at break, as highlighted in Section 3.2.2. The adhesive fillet was applied after welding the skin-stiffener joint, which is discussed in Section 4.3.4. Two layers of Flashbreaker tape were used to mask the region where the fillet was to be located and the joint was thoroughly cleaned with acetone. It was then roughened with 120-grit sandpaper. The tape was then replaced and the fillet region was cleaned with acetone again. Following this, the bonding region was plasma treated using the same equipment as was used for the DCB coupons, as described in Section 4.2, but due to size limitations of the plasma treatment apparatus, only half the length of the joint was treated. This likely affected the strength and failure mode of the joint, which is further discussed in Section 5.2. The adhesive was applied using an applicator gun and the fillet radius was created by moving a small aluminium plate with a 2 mm radius along the joint. The tape was then removed and the adhesive was cured at 40° for 16 hours. A micrograph of the joint with adhesive fillet is shown in Figure 4.11a.

4.3.3. Fillet Implementation

In a first attempt to implement a PA12 neat resin fillet in the joint, the skin, stiffener and fillet were placed separately in the weld tooling, as shown in Figure 3.2b. A PA12 fillet was chosen because it had a lower melting temperature than the laminate material and PA11 fillet. During this first attempt the induction coil was positioned halfway above the stiffener flange and after welding, a 10 mm wide section of the joint was cut and separated to investigate the fracture surface and the size of the welded region. This showed that the region around the fillet was barely affected by the welding process. This was also observed in a micrograph of the fillet region, shown in Figure 4.7a. Therefore, this approach was repeated, but the coil was moved 6 mm closer to the fillet region and the electric current input was increased by 6%. A thermocouple was placed between the fillet and stiffener radius and this showed that this region was barely, if at all, affected by the induction coil and the measured temperature remained far below the melting temperature. Again a 10 mm wide section was separated and from the fracture surface it was concluded that this approach was not effective for implementing a resin fillet in an L-joint. A micrograph of the fillet region for this attempt is shown in Figure 4.7b. As can be seen, the fillet joined with the skin successfully, but a gap was present between the stiffener and fillet due to insufficient heat generation. The temperature in this region can potentially be increased by changing the coil geometry, reducing the laminate thickness or by moving the coil closer to the workpiece, but this was not further investigated. Varying the coil geometry was outside the scope of this thesis and the fillet implementation method should not be strongly dependent on the laminate thickness. It was also not possible to move the coil much closer to the joint.

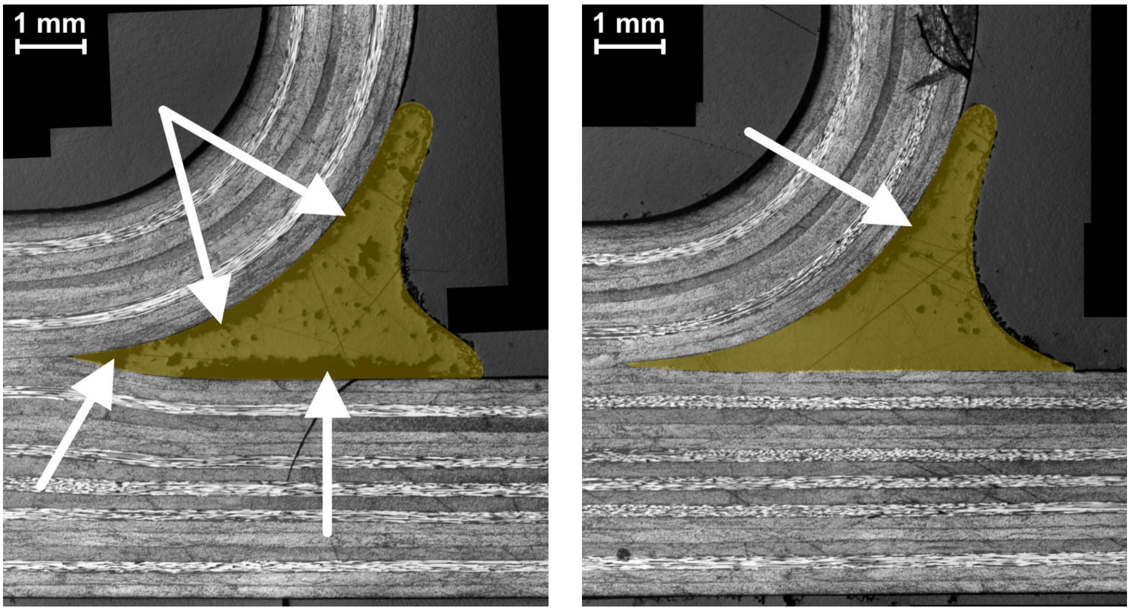

(a) (b)

Figure 4.7: Micrographs of joint 2 (a) and joint 3 (b). During welding of joint 3, the input current was 6% higher and the coil was positioned 6 mm closer to the fillet region than for joint 2. The fillets are highlighted in yellow for better visibility. The arrows point to regions where the fillet did not weld to the laminate material.

Because the main problem during this approach was joining the fillet to the stiffener, it was decided to attach the fillet to the stiffener radius before welding. In this second attempt, a hot air tool was used with a setup as shown in Figure 4.8a. Initially this was tried with a PA12 fillet, because of its lower melting temperature, but it snapped due to its limited flexibility. Thus, from this point onward a PA11 fillet was used, which was more flexible. Because in this setup the hot air tool was not guided well, the fillet was not positioned straight. Also, because of the rectangular shape of the hot air tool nozzle, through which the fillet was guided, the edges of the fillet overheated and deformed before attaching to the stiffener, which is shown in Figure 4.9a. A custom steel nozzle was 3D printed with the guiding tube in the shape of the fillet and although this reduced the deformation somewhat, the issue with aligning the fillet remained. Despite these defects, pull-off tests showed this method greatly increased joint performance, which is discussed in Section 5.2. For this reason a third approach was investigated with the aim to further improve joint performance and to better maintain the shape of the fillet.

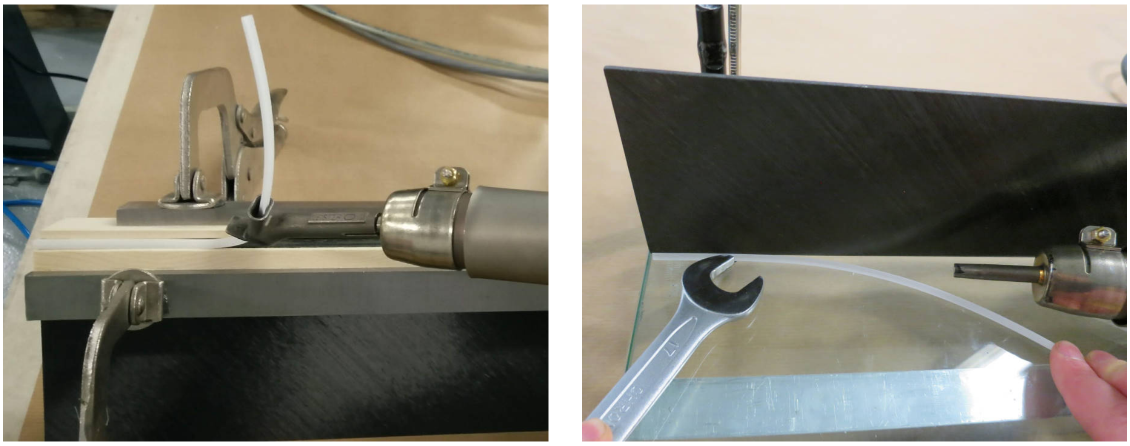

(a) (b)

Figure 4.8: Two methods used for joining the fillet to the stiffener radius with a hot air tool. The method in (a) caused deformation of the fillet and the method in (b) lead to the fillet shape being maintained better.

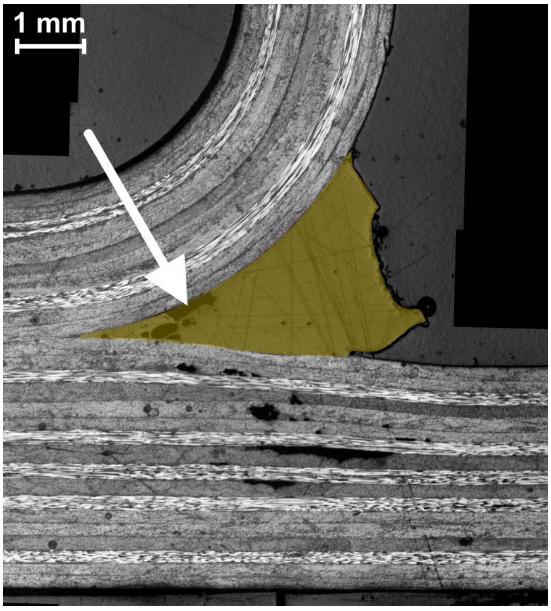

(a)

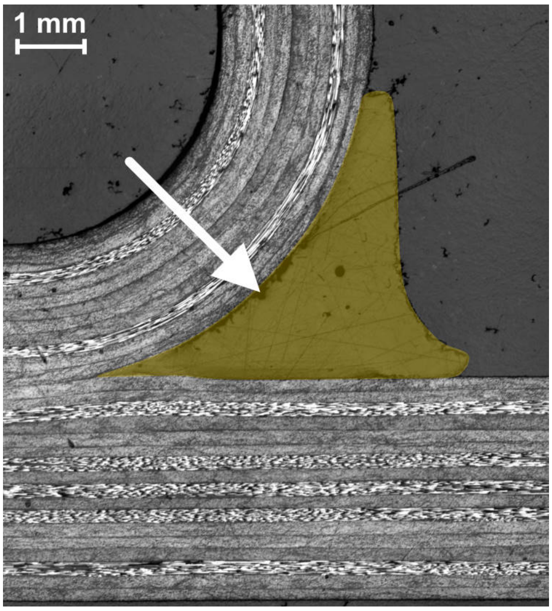

(b)

Figure 4.9: Micrographs of joint 4 (a) and joint 8 (b). Both fillets were attached to the stiffener using a hot air tool before welding, but because in joint 4 the fillet was guided through a steel nozzle it was badly deformed. The fillets are highlighted in yellow for better visibility. The arrows point to regions where the fillet did not weld to the laminate material.

In the third attempt the stiffener was clamped to a glass plate, after which hot air was blown between the stiffener radius and fillet, as shown in Figure 4.8b. When both surfaces were in a molten state the fillet was pushed against the stiffener with a wrench. The glass plate ensured correct alignment of the fillet and because the fillet was not in contact with a nozzle, there were no signs of overheating or large deformations. The fillet was positioned straighter than with the previous approach. In Figure 4.9b a micrograph is shown after the joint was welded. A small gap between the stiffener and fillet is visible, which shows that further improvement is possible. The same method was used for the machined CF/PA11 fillet.

4.3.4. Induction Welding

The welding setup used for this thesis was described in Section 3.3. Before welding, the skin, stiffener and fillet, if used, were dried at 80°C for 16 hours to remove any moisture absorbed by the nylon matrix and before placing them in the weld tooling, they were degreased with acetone to prevent contamination in the weld line. In total, 9 skin-stiffener joints were welded and these are listed in Table 4.1. The parameters that were varied during these experiments were the electric current in the coil and the speed at which the coil moved along the weld. Also, after the second welded joint the coil was repositioned and moved closer to the fillet region, in order to increase the temperature at the skin-fillet interface, as mentioned in Section 4.3.3. In the table, the current and speed are displayed relative to the baseline joints 5 and 6. The absolute values are not shown, because they are intellectual property of KVE. Temperature in the weld line were monitored for joints 1–4 using thermocouples between the skin and stiffener and they were positioned as shown in Figure 4.10. From joint 2 onwards, the speed at which the coil moved between the outermost thermocouples was kept the same, but until joint 3 the dwell times at the start and end of the weld and the speed at which the coil moved outside the outermost thermocouples was varied. For joints 1–3 a total of 18 weld runs were performed, most of which at lower current values to prevent the laminates from melting and affecting the heating behaviour for further trial runs. After these trial runs, settings were found for which the temperature profile along the weld was fairly consistent. For joint 4 the maximum temperature among the 5 thermocouples ranged from 226°C to 251°C and the material stayed above the melting temperature of 183°C for between 28 and 43 seconds. The maximum processing temperature was defined by the material manufacturer as 260°C and was not exceeded.

Table 4.1: L-joints with fillet type. The electric current and coil speed are shown relative to the baseline joints 5 and 6.

Joint	Fillet[a]	Relative current[b]	Relative speed[b]	Notes
1	—	0.88	0.67	Coil positioned 6 mm further away from stiffener radius than baseline
2	PA12	0.94	1	Coil positioned 6 mm further away from stiffener radius than baseline
3	PA12	1	1	—
4	PA11	1	1	Fillet joined to stiffener before welding[c]
5	—	1	1	Baseline
6	—	1	1	Baseline
7	Adhesive	1	1	Fillet applied after welding
8	PA11	1	1	Fillet joined to stiffener before welding[d]
9	CF/PA11	1	1	Fillet joined to stiffener before welding[d]
10	PA11	—	—	Autoclave co-consolidated joint

[a] PA11/PA12 = SLS 3D printed neat PA11/PA12
CF/PA11 = machined quasi-isotropic CF/PA11 laminate
Adhesive = Araldite 2048-1 two component epoxy paste adhesive
[b] Compared to baseline joints 5 and 6
[c] Method as shown in Figure 4.8a
[d] Method as shown in Figure 4.8b

Wrinkling of fibers at the surface of the stiffener flange was observed in each joint, as shown in Figure 4.10 at arrow (b). These so-called chicken tracks were created by a combination of temperature, pressure and the material of the pressure applicator, but investigating the cause of this phenomenon was outside the scope of this thesis. Also, they did not influence the behavior of the joint, because they were not at a critical location, such as near the fillet region or under the skin. Fiber waviness in the skin, as discussed in Section 4.3.1, is highlighted in Figure 4.10 by arrow (a) and was located near the side of the laminate, which was trimmed off when cutting the test coupons.

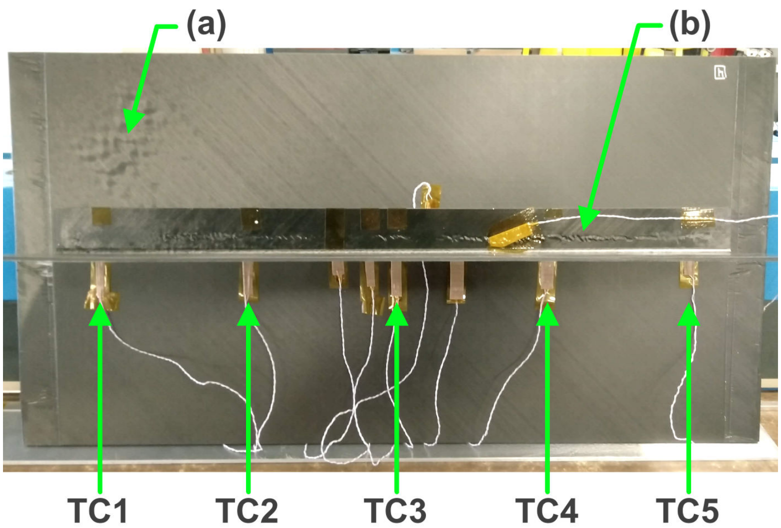

Figure 4.10: Joint 3 after welding. Thermocouples 1–5 were used for joints 1–4 to monitor the temperature in the weld line during welding and in this joint additional thermocouples were used. (a) Fiber wrinkling in the skin and (b) chicken tracks on the stiffener flange were observed in each joint.

While before welding the angle between the stiffener flange and web was 1° smaller than a perfect right angle, after welding this had increased to 2°–3°. This was probably caused by the way the tooling was designed. As can be seen in the schematic of the tooling in Figure 3.2b, there was some space around the stiffener web and when the radius section was heated while pressure was applied, the stiffener web had some freedom to move. Because the stiffener was already slightly bent before welding, as previously discussed in Section 4.3.1, this problem could not easily be solved by placing a shim plate next to the stiffener web. Also, because several joints had been welded before this was suggested as the possible cause of this problem, it was decided to not adjust the tooling, in order to maintain consistency between the samples.

In joint 4, shown in Figure 4.9a, the skin laminate under the fillet deconsolidated during the welding process. In joint 8, shown in Figure 4.9b, on the other hand, no delaminations were visible, even though the same weld settings were used. A possible explanation for this is that insufficient pressure was applied between the plies in the laminate, because the fillet was positioned incorrectly. Further examination of the interface between the skin and fillet for these two joints showed that good diffusion of the resin material had been achieved for joint 4, but that a faint boundary was present in joint 8. This could have been caused by some sort of contamination in the interface, but this is unlikely, because the material was cleaned with acetone before welding. An alternative theory could be that because in joint 8 the skin and fillet were in contact during the entire welding process, heat dissipated through the fillet, cooling down the skin. This could have led to the temperature in the interface being too low for good diffusion. In this theory, the temperature in the skin surface in joint 4 was higher, because it was not in contact with the fillet material and was insulated by a thin layer of air. Once the skin started deconsolidating, it came in contact with the fillet and heated the interface sufficiently for good diffusion of resin material between the skin and fillet.

In micrographs of joints 5–7, in which no fillet was implemented during welding, a small resin fillet had formed under the stiffener radius due to resin squeeze-out. This is pointed out by the arrow in Figure 4.11a. Although small, it decreases the stress concentration at this point and it could be expected to better resist crack initiation than when a pre-crack is present after welding, which was the case for joint 1.

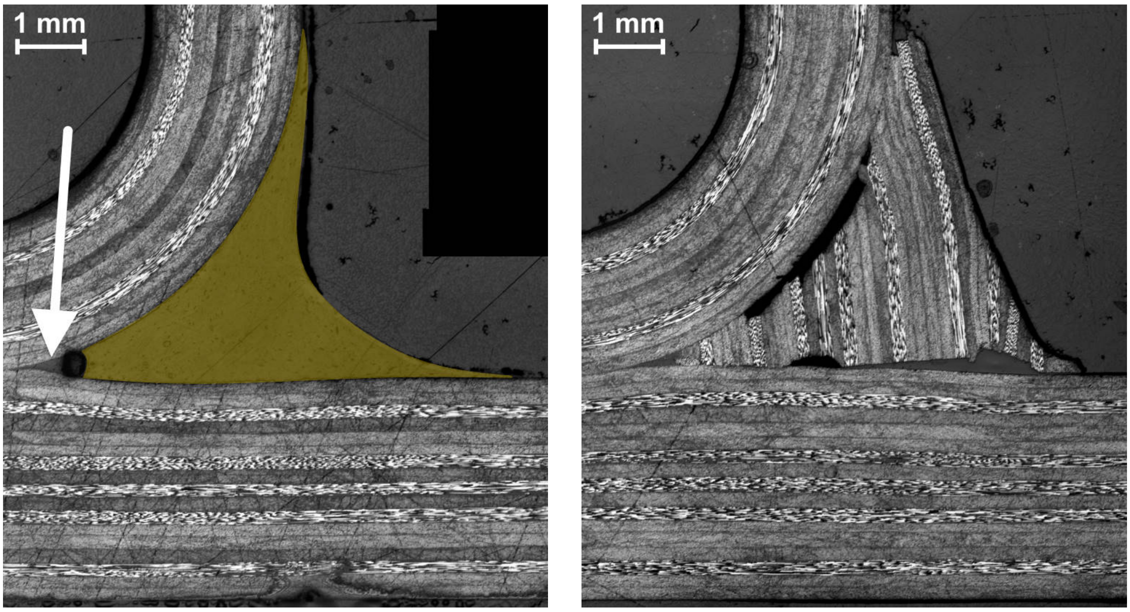

(a) (b)

Figure 4.11: Micrographs of joint 7 (a) and joint 9 (b). A small squeeze-out resin fillet was formed during welding in joint 7 as pointed out by the arrow. The adhesive fillet in joint 7 is very close to the designed shape. The fillet quality of joint 9 is poor, with air gaps present around the fillet. The fillet in (a) is highlighted in yellow for better visibility.

In Figure 4.11a it is shown that the shape of the adhesive fillet is close to the designed shape. This is, however, not the case for joint 9 with the machined CF/PA11 fillet in Figure 4.11b. Also, large gaps were present around the fillet material. The gap between the stiffener and fillet was created when the fillet was joined to the skin using the hot air tool, as described in Section 4.3.3. This could probably have been prevented if the temperature of the hot air was increased and more pressure was applied. The space between the skin and fillet could probably also be removed if the fillet was positioned lower on the stiffener radius. In that case, more pressure would be exerted between the skin and fillet during welding.

4.3.5. Co-consolidation

An autoclave co-consolidated joint was created with a neat PA11 resin fillet, in order to compare the pull-off strength values with joints 4 and 8. Because a near-perfect fillet geometry and a high degree of diffusion between laminate matrix and fillet material could be achieved, it was expected that this joint could indicate a joint strength upper boundary. The aluminium tooling consisted of two large milled blocks, two water-jet cut picture frames and a 1 mm thick caul plate, as shown in Figure 4.12. A 215 mm wide joint was created with this tooling, half the length of the other joints, which allowed for the creation of 3 test coupons and a microscopy sample. The pocket for the stiffener flange in one of the tooling blocks was measured 2.06 mm deep, so a stiffener was selected with a flange thicker than this. This ensured that there would be pressure between the skin and stiffener when outside pressure was applied. Although the stiffener was designed to be 2.2 mm thick, during the two hot pressing steps this thickness had decreased to an average 2.09 mm in the stiffeners, with the flange being slightly thinner at 2.06 mm. The flange thickness of the selected stiffener ranged between 2.08–2.12 mm.

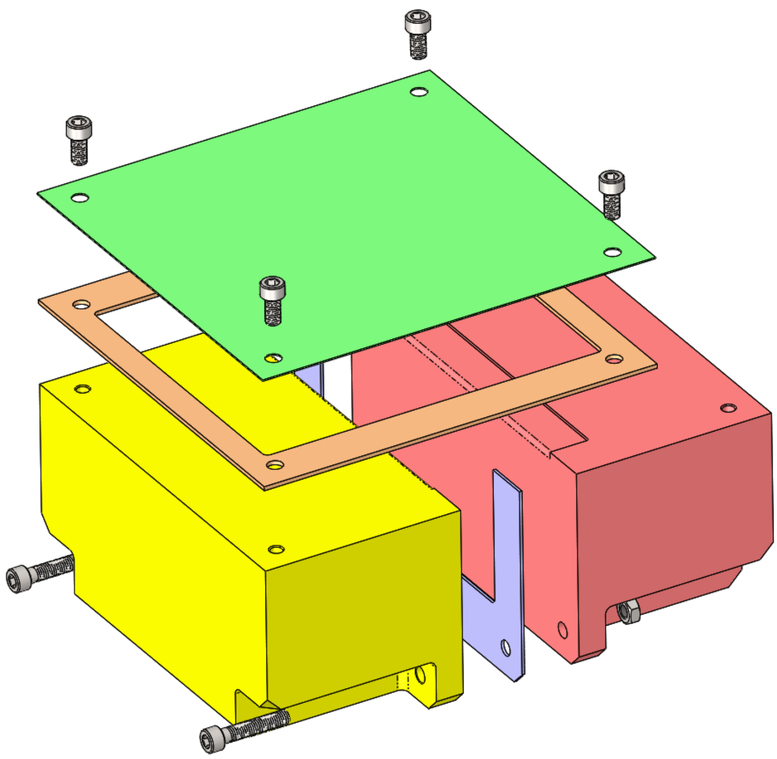

Figure 4.12: Aluminium autoclave co-consolidation tooling design consisting of two CNC machined blocks, two water-jet cut picture frame plates and one water-jet cut caul plate. Fasteners were loosely tightened and were used only for aligning of the components.

Because of the high mass and volume of the tooling blocks, a test was performed to study the temperature distribution in the tooling during heating. The tooling was assembled without components inside and thermocouples were placed at various locations on the inside and outside. It was then placed in an oven set to 180°C and the tooling was heated until the blocks reached 120°C. This test showed that the blocks heated uniformly, but that the temperature of the caul plate increased quicker, as was expected. For this reason it was decided to first set the autoclave to 175°C, below the melting temperature, and when this temperature was reached in the tooling blocks, the temperature was increased to 200°C.

The skin, stiffener and fillet were cut to the required dimensions with a diamond blade saw and any sharp edges on the tooling were removed with sandpaper. Release agent was applied to the tooling and the joint components were cleaned with acetone. The tooling was then assembled and five thermocouples were taped to the outside of the tooling at various locations to monitor the temperature during the process. After this, the assembly was vacuum bagged and placed in the autoclave. The set temperature and pressure, as well as the measured temperature on one of the loading blocks during the autoclave cycle are shown in Figure 4.13.

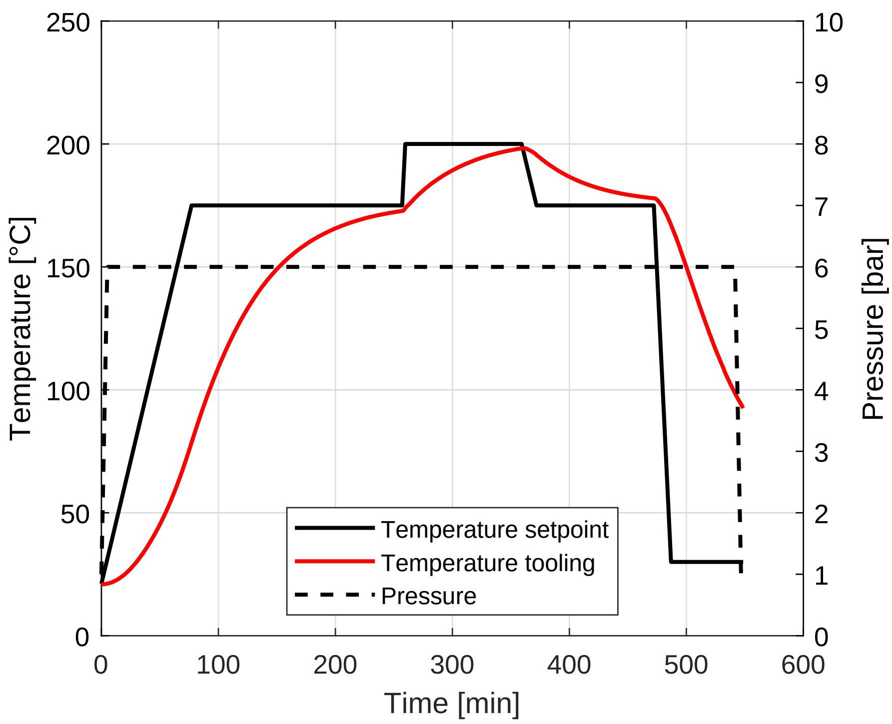

Figure 4.13: Temperature and pressure profile during autoclave co-consolidation of joint 10. Tooling temperature shown here was measured by a thermocouple taped to the outside of one of the aluminium blocks. The autoclave in the DASML at TU Delft was used.

After the autoclave cycle, the tooling was disassembled and the joint was removed. Although extra care was taken to minimize warping and spring back during the autoclave process by ramping up and down the temperature in steps, it was not avoided. The angle between the intended stiffener position and the actual position was 3°–3.5°, while it was 1° beforehand. Also, the skin had bent upwards as shown in Figure 4.14. The fillet material had squeezed out of the tooling at the edges and this resulted in an uneven distribution of fillet material along the joint, which can been is Figure 4.15. A micrograph taken approximately halfway the joint is shown in Figure 4.16. Some of the fillet material had squeezed out of the fillet region and ended up on top of the skin. Also, the stiffener radius had deconsolidated, expanding to nearly 150% of its origin thickness. Near the edges of the joint this effect was even more pronounced. These defects suggest that the caul plate exerted insufficient pressure on the joint. The fillet shape was as designed and better than joints 4 and 8, as shown in Figure 4.9. Also, no interface between the laminates and fillet was observed, suggesting good diffusion of the resin material.

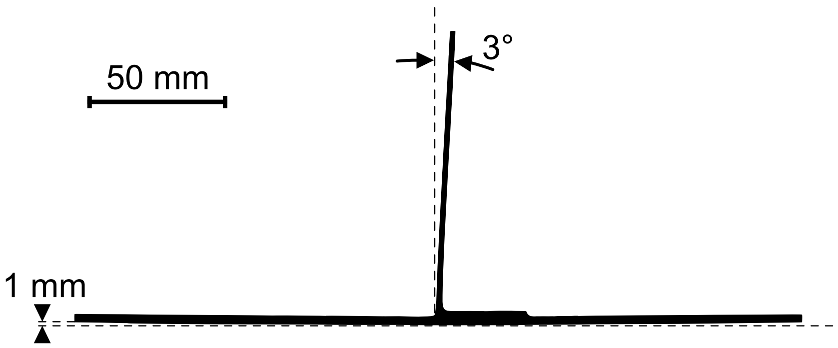

Figure 4.14: Cross-section of the co-consolidated joint after the autoclave cycle. Some warping had occurred during the process.

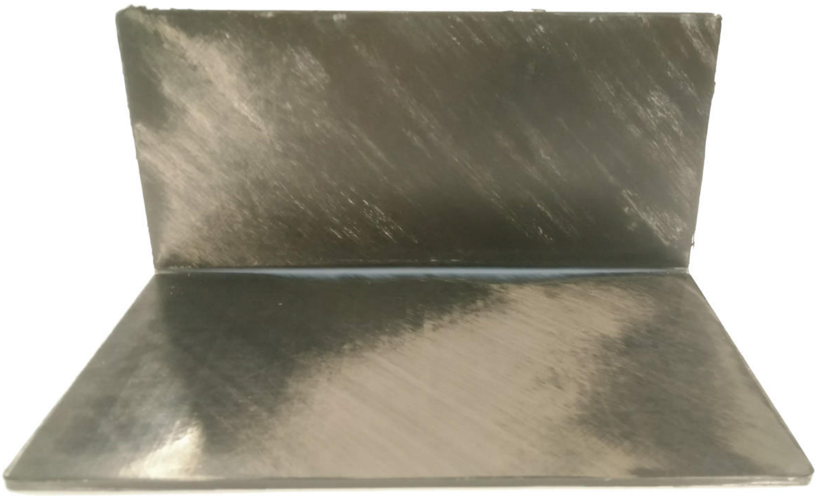

Figure 4.15: The co-consolidated joint after the autoclave cycle. Fillet material had squeezed out at the side of the joint and this can be noticed from the lack of white resin material away from the center of the joint.

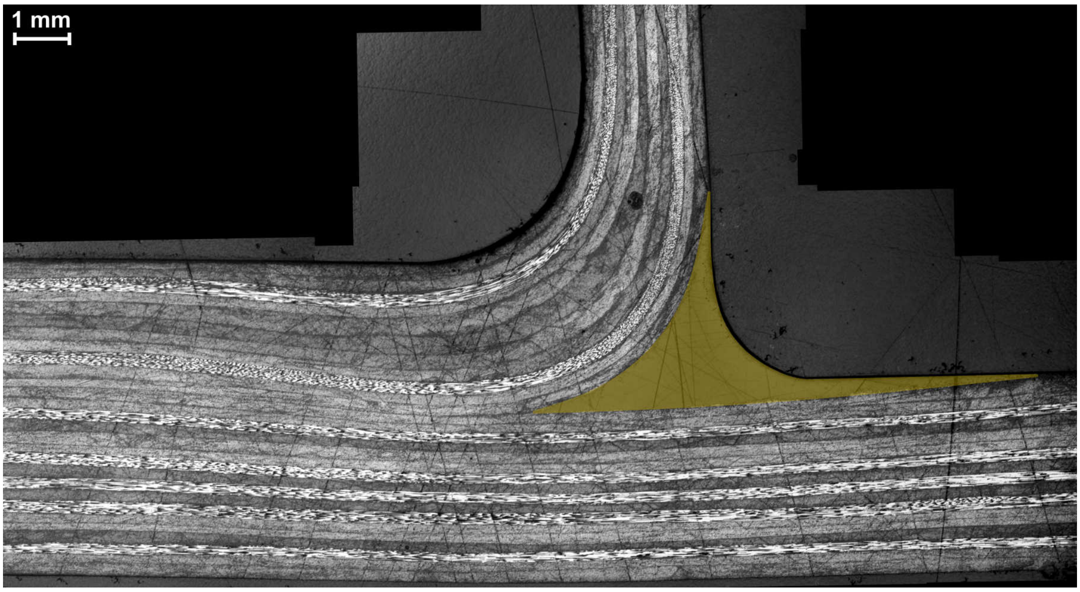

Figure 4.16: Micrograph of joint 10. Fillet material flowed onto the skin laminate and the stiffener radius expanded to 150% of its initial thickness and filled a part of the fillet region. The fillet is highlighted in yellow for better visibility.

4.3.6. Coupons

Because thermocouples were used in joints 1–4, only a limited number of 50 mm wide coupons could be created, with in particular joint 3, in which ten thermocouples were used, as shown in Figure 4.10. The remaining material, from which no pull-off coupons could be produced, was used for other purposes. For example, small samples were made which were pulled apart to study the fracture surface before the coupons were tested using a tensile machine. This information was used to tune the weld settings. For the autoclave co-consolidated joint only three samples could be produced, as explained in Section 4.3.5. The number of coupons created for each joint is given in Table 5.2. In Figure 4.17 it is shown for joints 5–9 how the coupons were cut, with six 50 mm wide coupons and one microscopy sample. The start and end region were scrapped. The coupons were cut with a water cooled diamond blade saw. The sharp edges of the coupons were then removed using 60-grit sandpaper, followed by 240-grit and 500-grit.

Joints 1–5 were pull-off tested using the regular setup in which the stiffener web was clamped in place, shown in Figure 3.3. Joints 6–10, however, were loaded using a new setup as discussed in Section 3.4 and 4.4 and for this the web height was reduced from 100 mm to 90 mm using the diamond blade saw and two 8 mm holes were drilled in the coupons, as is shown in Figure 4.17. A drill jig was 3D printed in which two drill bushings were placed, ensuring that the holes in each coupon were positioned correctly. A drill bit for CFRPs was used and the holes were deburred after drilling.

Figure 4.17: Six test coupons and one microscopy sample were cut from joint 6. The start and end zone were scrapped. Holes were drilled in the stiffener web of the test coupons for the new test setup.

4.4. Pull-off Test Setup

As discussed in Section 3.4, the regular pull-off test setup was modified for this thesis and in Figure 4.18 an exploded view of the web clamp design is shown. The setup consisted of four steel component, all manufactured by the electronic and mechanical support division at TU Delft. The outer component, brown in the figure, was made from a U-beam section and a plate, which were welded together. This component could be clamped in a regular mechanical grip. For improved grip the vertical section was roughened using 120-grit sandpaper, after which a sheet of paper was bonded to it. The block on the right side in the figure, in green, and the spacer, in red, were knurled to improve its grip on the stiffener web and to reduce the bearing load on the holes. The spacer block thickness was chosen so that the rotation axis, the bolts through the two larger components, was aligned with the midplane of the stiffener web. As discussed in the methodology chapter, this thickness could be modified in order to introduce an additional bending moment, but this was not done in this thesis. The skin grips were not modified for the new test setup.

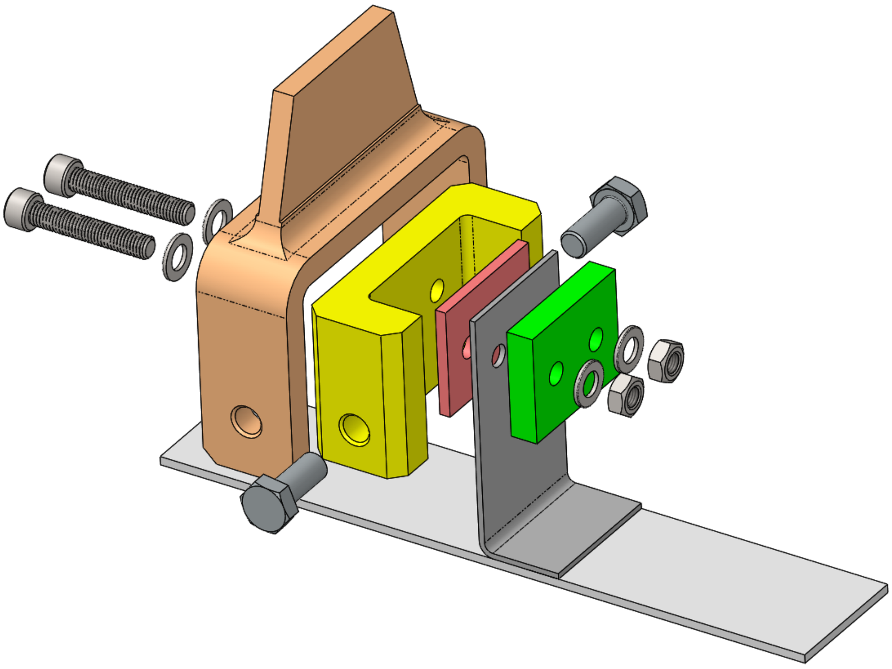

Figure 4.18: Stiffener grip design for the new pull-off test setup, consisting of four steel components manufactured by the electronic and mechanical support division at TU Delft.

5
Testing and Results

In this chapter the test procedures and results are discussed. The results from the double cantilever beam test are given in Section 5.1 and the L-joint pull experiments in Section 5.2. Finite element analysis performed on these joints is analyzed in Section 5.3 and this chapter is concluded with a discussion on the results in Section 5.4.

5.1. Double Cantilever Beam

Double cantilever beam tests were performed on the CF/PA11 material used in this thesis to obtain the mode I fracture toughness data needed for the virtual crack closure technique in finite element analysis. This test was done according to ASTM D5528-13 [103] and the production of the samples was described in Section 4.2. Two batches of DCB coupons were created, of which the first was only used for trial runs. The test setup is shown in Figure 5.1.

Figure 5.1: Double cantilever beam (DCB) test setup. The laminate side was covered with water based type writer correction fluid for better visibility of the delamination front and a raster was bonded to the edge, so that the delamination length could be measured accurately.

Water based type writer correction fluid was applied to the side of the coupons to better show the crack and a raster was bonded to it so that the crack length could be tracked accurately. The loading rate was 2 mm/min and a photo was taken ever 5 seconds. The crosshead displacement and applied loading was measured by the tensile machine and crack length was measured after the test using the photos. Load was applied until the initial crack length had increased by 3–5 mm after which the coupon was unloaded and reloaded. When during initial loading the crack propagated in an unstable manner, reloading was initiated once the crack had propagated a further 3–5 mm. After testing, the load and displacement values were recorded at delamination onset and at increments of 1 mm during the first 5 mm of crack growth. Then, until a crack length of 45 mm was reached, values were recorded every 5 mm and again at increments of 1 mm until a total crack length of 50 mm was reached. If any of these measuring points were passed during unstable crack growth, the values were omitted. In the left plot in Figure 5.2 the force displacement curve of one of the samples is shown. The markers indicate points at which a crack length was reached in the increments as described above. As pointed out in the plot the crack propagated in an unstable manner once for this specimen. For some other specimens this occurred more often and over a greater length. After testing, the regions of unstable crack growth could be observed on the fracture surfaces. These areas were darker than the surfaces on which the delamination grew slowly. This was studied more in depth by *Leach et al.* [118] and with a scanning electron microscope they observed greater ductility in the polymer for stable crack growth. The optical differences on the fracture surface were caused by this difference in texture.

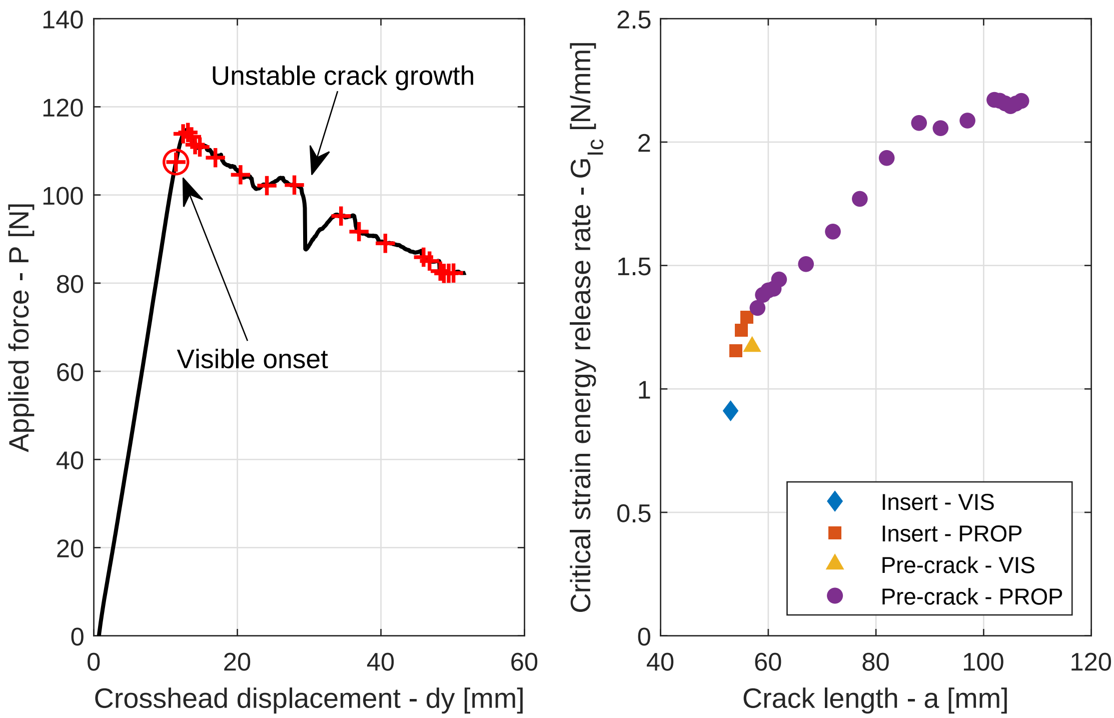

Figure 5.2: Left: force-displacement curve for sample B5 after creating a pre-crack. Markers are placed at the visible delamination onset and crack at 1 mm increments in the first and last 5 mm and at 5 mm increments in between. Right: G_{Ic} at these increments, calculated using the modified beam theory. VIS = visible onset; PROP = propagation.

The mode I critical strain energy release rate G_{Ic} for each of these recorded points was calculated using the modified beam theory (MBT), the compliance calibration (CC) method and the modified compliance calibration (MCC) method, as described in the ASTM standard [103]. These values were divided into four categories as shown in the right plot in Figure 5.2. G_{Ic} values were calculated for visual onset of crack growth from the polyimide insert and from the pre-crack after reloading. Values during crack propagations from the insert and pre-crack were also calculated, which were then averaged. Note that the left plot in Figure 5.2 only contains the period after reloading. Because the average G_{Ic} values over all specimens, calculated using the three data reduction methods, did not differ by more than 2.8%, the method with the most conservative results, MBT, was selected. In this method, strain energy release rate is calculated as follows:

$$G_I = \frac{3P\delta}{2b(a + |\Delta|)} \tag{5.1}$$

where P is the applied force, δ the load point displacement (here equal to the crosshead displacement dy), b the coupon width, and a the delamination length measured from the load point. Because some rotation may occur at the delamination front, this equation includes the correction factor Δ, which can be found experimentally.

In Table 5.1, the G_{Ic} values for visual onset and propagation after creating the pre-crack are given. As can been be seen in the right plot in Figure 5.2, during crack propagation the fracture toughness of the material increased. This effect can be attributed to fiber bridging, a process where during delaminations, fibers from one side of the laminate remain attached to the other half. This is shown in Figure 5.3. Additional force was therefore required to pull apart the bridged fibers, effectively increasing the measured fracture toughness. For this reason, the reliability of G_{Ic} values calculated ahead of the front of the pre-crack were questionable. Also, during L-joint pull-off experiments it was observed that the joint failed abruptly after crack initiation. Thus, the G_{IC} value of 1.25 N/mm at visible crack onset was used for finite element analysis. This value is very close to 1.33 N/mm as assumed for CF/PEKK in Table 3.1.

Table 5.1: G_{Ic} values calculated from the DCB test using the modified beam theory. VIS = visible onset; PROP = propagation.

Sample	Width [mm]	Thickness [mm]	Pre-crack length [mm]	G_{Ic} (VIS) [N/mm]	G_{Ic} (PROP) [N/mm]
B1	25.69	3.90	56	1.10	1.46
B2[a]	25.63	3.92	57	1.09	1.67
B3	25.58	3.86	66[b]	1.20	1.69
B4	25.57	3.83	57	1.35	1.97
B5	25.60	3.82	57	1.17	1.83
B6	25.70	3.82	56	1.23	1.84
B7	25.69	3.83	57	1.59	2.02
Average	25.64	3.85	58	1.25	1.78

[a] Upper skin failed at 36 mm delamination length from pre-crack.
[b] Crack propagated abruptly from insert during initial loading.

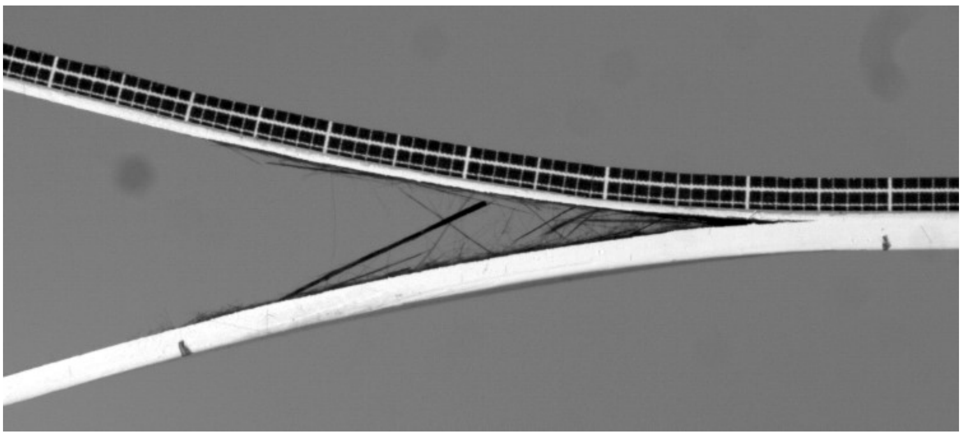

Figure 5.3: Fiber bridging during the DCB test. This increased the force required to further propagate the delamination crack, which resulted in a higher calculated critical strain energy release rate during the propagation phase.

5.2. L-joint

A total of 46 L-joint coupons were tested under quasi-static pull-off loading and the 10 tested joints were listed in Table 4.1 with a very short summary of the production process. The number of coupons that were created for each joint are given in Table 5.2. Joints 1–5 were tested with the old setup, as shown in Figure 5.4a, which was available in the DASML. For joints 6–10 the new setup, as shown in Figure 5.4b, designed for this thesis, was used. In both setups horizontal displacement of the stiffener web was constrained, but the new setup allowed rotation around the loading axis.

Table 5.2: Quasi-static pull-off test results of the ten manufactured L-joints. Joints 1–9 were produced using the induction welding process and joint 10 was created by autoclave co-consolidation. The complete test results are given in Appendix A.

Joint	No. of samples	Fillet	Test setup	Failure load[a] [N/mm]	CV[b] [%]
1	4	—	Old	23.0	4.1
2	3	PA12	”	25.8	1.2
3	2	PA12	”	29.2	0.6
4	4	PA11	”	41.8	7.8
5	6	—	”	30.8	1.6
6	6	—	New	31.5	2.8
7	6	Adhesive	”	33.7	6.0
8	6	PA11	”	35.4	4.1
9	6	CF/PA11	”	32.5	8.5
10	3	PA11	”	56.9[c]	13.2

[a] Load measured by the tensile machine divided by coupon width.
[b] Coefficient of variation = (standard deviation / mean) × 100%.
[c] Skin-stiffener separation. Skin bottom surface failed in compression at 47.0 N/mm (CV = 2.3%).

The thickness and width of the skin and stiffener laminates were measured at multiple locations, so that accurate coupon geometry data was available for comparison with finite element analysis. Before testing, each coupon was dried in an oven at 80°C for at least 16 hours to remove moisture absorbed by the polyamide resin, except for joint 7 with the adhesive fillet. The drying temperature was higher than the operating temperature of the adhesive, so the joint was dried before applying the adhesive, three days prior to testing. For sample 1.1 (the coupon nearest to the weld start zone in joint 1) a loading rate of 0.5 mm/min was used, but due to time considerations this was increased to 1.0 mm/min for further tests. Displacement was measured by the 20 kN Zwick tensile machine, but in order to account for any slip between the skin and clamp or the clamp and mechanical grip, for joints 5–10 an external displacement sensor was positioned under the skin, as can be seen in Figure 5.4b. During testing of joints 5–10, a camera was used to take photos of the joint every 2 seconds.

The average failure load of the joints is listed in Table 5.2 and displayed in Figure 5.5. The complete test results are provided in Appendix A. Because for joints 1 and 2 the induction coil was positioned further away from the fillet region during welding than for the other welded joints, a crack was already present between the skin and stiffener before testing. This can be seen on the fracture surface of sample 2.3 in Figure 5.6a, where the surface until approximately 1 mm ahead of the PA12 fillet does not show any damage. For two of the three tested samples of joint 2 the fillet fell out of the joint during testing and the fillet shown in the photo was only very loosely connected. This was also shown in the micrograph in Figure 4.7a. Because the weld bath was located away from the fillet region, the failure load was lower than for baseline joint 5, which was loaded using the same test setup. This result agrees with expectations from the literature review [5] in Section 2.5.2. For joint 3 the induction coil was located in the same position at for baseline joint 5, but because the fillet was not connected to the stiffener radius, as was shown in Figure 4.7b, no significant difference in joint strength was measured.

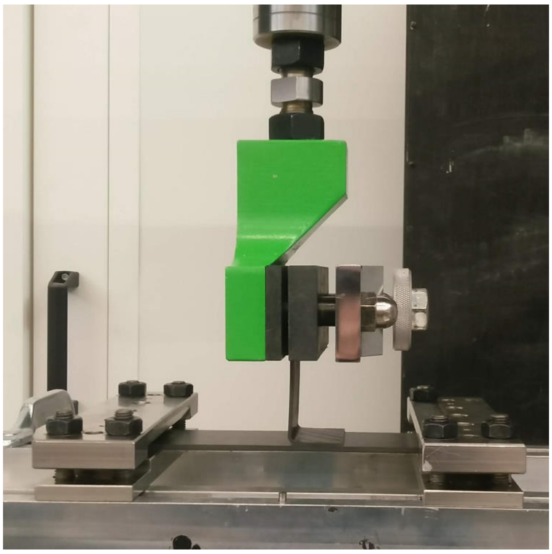

(a)

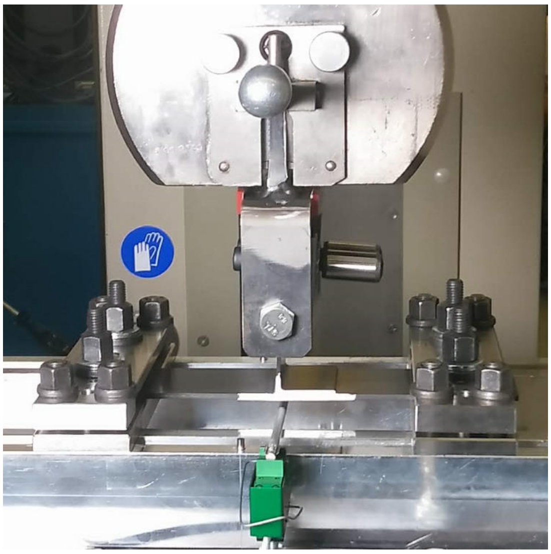

(b)

Figure 5.4: (a) Old test setup in which rotation around the top of the stiffener web was constrained. This setup was available in the DASML. (b) New test setup in which the joint was free to rotate around the loading axis. The skin grip design was not changed for this new setup.

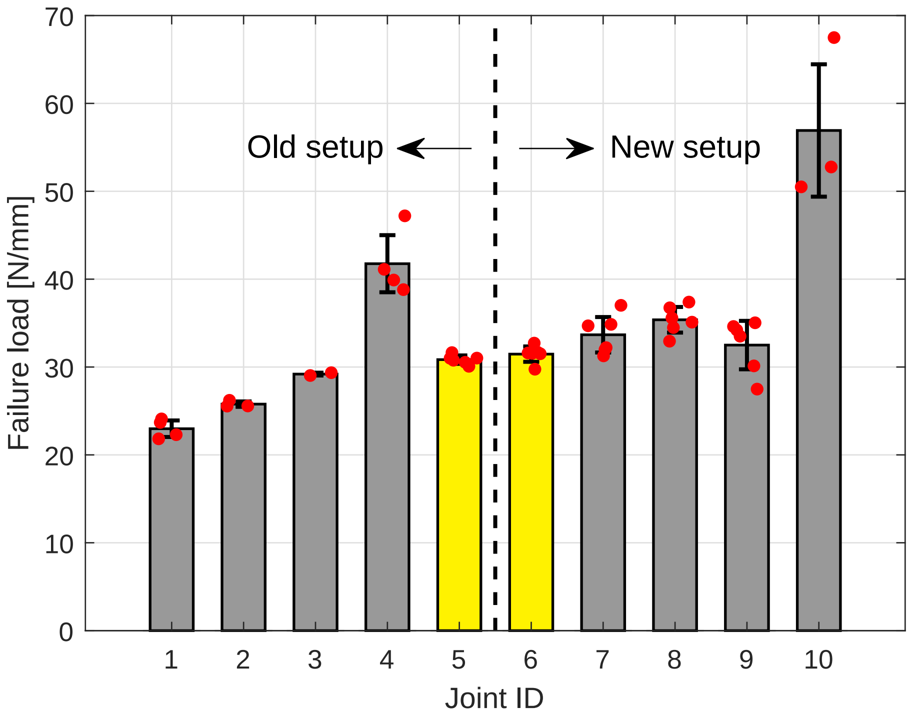

Figure 5.5: Quasi-static pull-off test results for the ten manufactured L-joints. A short description of the fillet type used for each joint is given in Table 5.2. Joints 1–5 were tested using the old test setup and joints 6–10 using the new setup. Joints 5 and 6 were baseline joints without fillet.

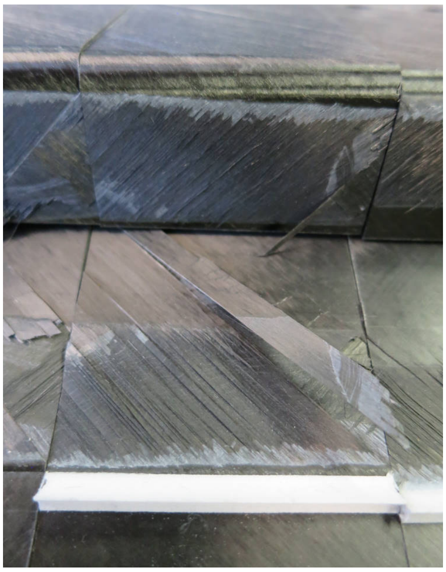

(a)

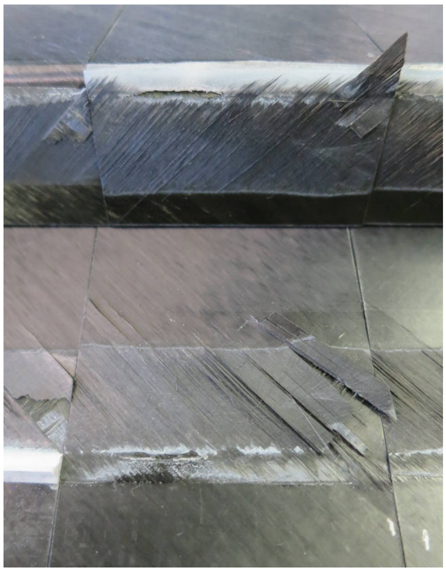

(b)

Figure 5.6: (a) Fracture surface of specimen 2.3. The fillet was very poorly connected to the skin laminate, because the welded region did extend far enough. From joint 3 onward, the induction coil was positioned closer to the fillet region. (b) Fracture surface of specimen 4.1. This batch delivered the highest joint strength of the induction welded joints. Inconsistency in the fillet placement was observed, leading to some poorly welded regions.

Joint 4, for which a PA11 fillet was attached to the stiffener before welding, using the method as shown in Figure 4.8a, a significantly higher joint strength than the previous joints and baseline joint 5 was found (Tukey honestly significant difference (HSD) test with $\alpha = 0.05$). This was the first indication during testing that a neat resin fillet could lead to increased joint strength. The measured strength values for the four tested samples were 38.8, 39.9, 41.1 and 47.2 N/mm, so the scatter between the coupons was high, with the strongest sample being 21.6% stronger than the weakest. This was expected, because the fillet was not positioned straight and was deformed when it was joined to the stiffener with the hot air tool, as discussed in Section 4.3.3 and shown in the micrograph in Figure 4.9a. The fracture surface of coupon 4.1 (41.1 N/mm) is shown in Figure 5.6b. The joint failed between the skin and fillet and after initiation the crack propagated abruptly along the weld line. Fibers were transferred from the skin to the fillet, indicating good diffusion between resin in the skin and fillet. However, on the left side of the joint, as seen in the figure, the skin and stiffener did not connect well, which was likely caused by poor contact between the skin and fillet during welding. Similar defects were observed in the other coupons, but was very limited in the strongest (47.2 N/mm) specimen.

Based on these observations, an attempt was made to implement this resin fillet more consistently in joint 8, as described in Section 4.3.3. Although the strength increase of 12.4% compared to baseline joint 6 was statistically significant (Tukey HSD test with $\alpha = 0.05$), not the same improvement was found as for joint 4. The fracture surface of coupon 8.4 (37.4 N/mm) is shown in Figure 5.7a and although the fracture between the skin and fillet was more consistent, fewer fibers had transferred from the skin to the fillet and a less pronounced imprint from the fillet was visible on the skin. Also, because the skin and fillet were not as well connected, before abrupt skin-stiffener separation, a crack was present between the skin and fillet and is shown in Figure 5.7b. As discussed in Section 4.3.4, in micrographs a faint boundary was observed between the skin and fillet in joint 8, indicating that no good diffusion between the resin material had been achieved. This could also explain how this crack could have propagated before final failure of the joint. Crack growth before failure was not observed in joint 4. On the fracture surface of joint 8 in Figure 5.7a, ahead of the fillet, a white haze can be seen, which indicates slow crack propagation or at least some stretching of the resin material, as discussed in Section 5.1. This is visible to only a very limited extend on the fracture surface of joint 4. This also indicates that joint 4 failed abruptly and the skin and fillet did not separate before failure.

(a)

(b)

Figure 5.7: (a) Fracture surface of specimen 8.4. Limited transfer of fibers from the skin laminate to the fillet occurred, but the fillet was positioned consistently. (b) Photo taken during testing of specimen 8.4 shortly before failure. A crack between the skin and fillet is visible. The crack under the flange tip was present from the start.

Because with joint 4 a pull-off strength 35.4% higher than with the baseline joint 5 was obtained and more consistency in the application of the fillet was achieved in joint 8, a third joint with neat PA11 fillet was produced. Joint 10 was autoclave co-consolidated, as described in Section 4.3.5, and three coupons were created. Some warping of the laminates had occurred during the autoclave cycle, as shown in Figure 4.14, but because the new test setup was used, limited internal stresses were introduced when positioning the joint in the setup. The force-displacement curves of the three samples of joint 10 are shown in Figure 5.8. The average ultimate failure load, 56.9 N/mm, was 80.9% higher than baseline joint 6 and specimen 10.3 failed at 67.5 N/mm, 114.5% higher than the baseline average. The scatter between these failure loads was much higher than for any of the other joints, though. Due to the high strength of the joint, the skin bent further than the laminate was able to support and the lower surface of the skin failed in compression with out-of-plane fiber buckling (b) at an average of 47.0 N/mm (CV = 2.3%). Splitting of the stiffener laminate in the radius section (a) was observed at an average load of 28.9 N/mm (CV = 5.6%), which was caused by delamination in this region during the autoclave cycle. At point (c) skin damage on the lower surface propagated and in coupon 10.1 a crack was developed in the fillet at (d). Delamination propagated abruptly at point (e), but this did not lead to total separation between the skin and stiffener, as was the case for all other joints. Probably because the skin was bent excessively at this point, the interlaminar shear strength of the material played a dominant role in preventing the joint from separating completely.

The fractured fillet of specimen 10.2 is shown in Figure 5.9 and it can be seen that the crack initiated in the fillet radius, as was expected for a well implemented fillet. This was observed in experiments on CF/epoxy L-joints with an adhesive fillet [86], as discussed in Section 2.5.2. What can be noted from the force-displacement plot, is that although the load at final failure displays large scatter, the vertical displacement at failure differs less. The displacement at failure for the three samples was 21.8, 22.7 and 21.1 mm (CV = 3.0%). This could suggest that excessive deformation of the joint, in particular in the region above the buckled section of the skin, resulted in additional localized stresses in the fillet, which lead to failure of this fillet and therefore the joint. Based on these findings, it could be expected that scatter among the ultimate failure load values would be smaller if compressive failure in the skin and excessive deformation of the joint was avoided. Some methods to achieve this would be to increase the skin thickness or reduce the distance between the skin grips. The behavior of specimen 10.3 was different from the other two coupons, as is shown in the force-displacement plot. After testing of the first two samples, it was noted that the skin grips had moved closer towards each other, due to the

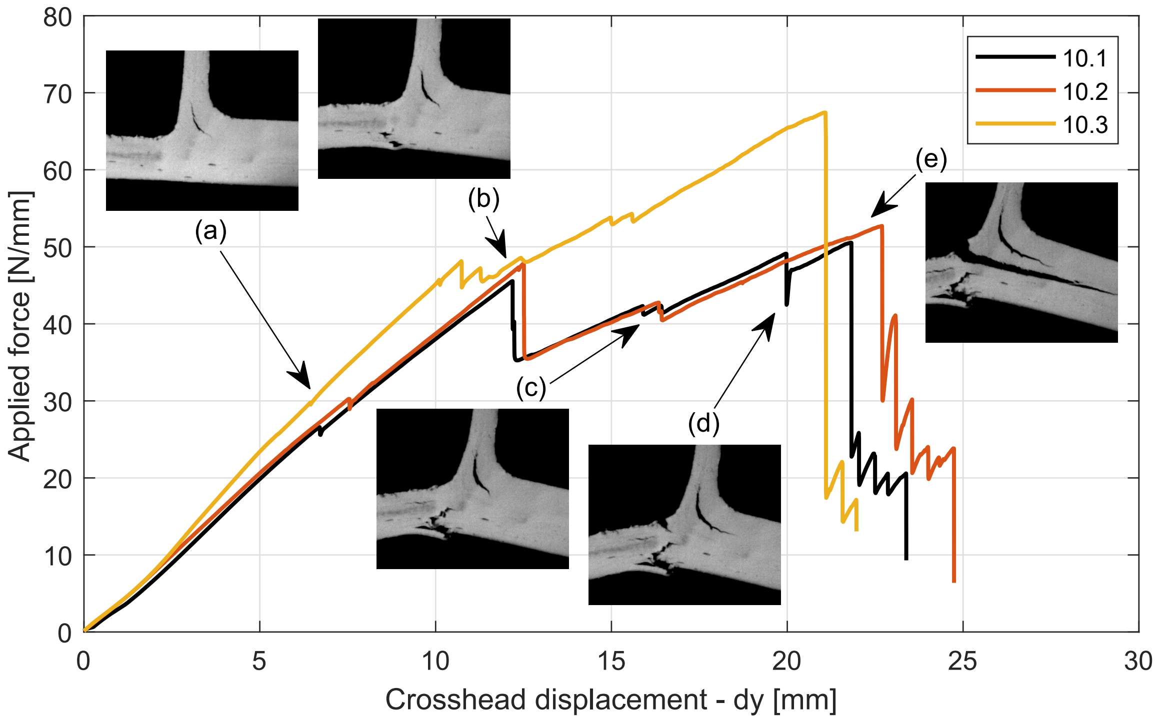

Figure 5.8: Force-displacement curves of autoclave co-consolidated joint 10. A crack appeared in the stiffener radius at (a) due to deconsolidation in the autoclave. The skin failed in compression at (b) and the failure propagated at (c). In specimen 10.1 a crack appeared in the fillet at (d) and final failure occurred at (e). The displacement was measured by the tensile machine.

high tensile loads exerted by the skin while bending. Because of this, the bolts holding the skin grips in place were tightened more strongly for the third sample. This reduced the displacement of the grips, resulting in a stiffer joint. This could have also changed the effect of the failure at point (b) in the graph, but this can not be determined with certainty from this limited number of specimens. In Section 5.3 the movement of the skin grips will be discussed further.

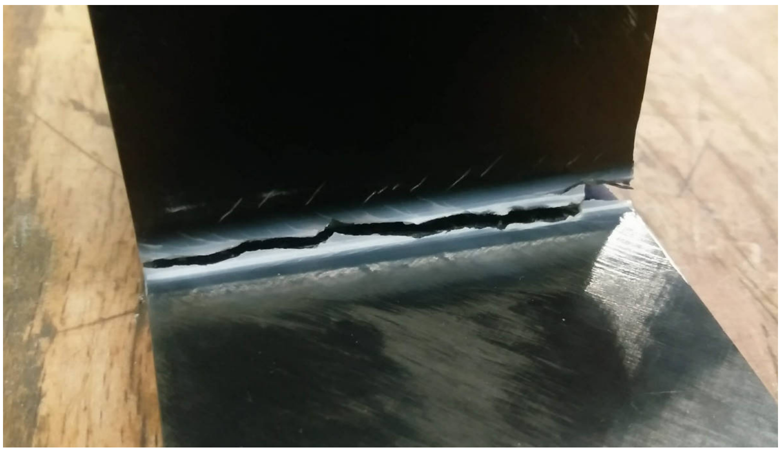

Figure 5.9: Crack in the neat PA11 fillet of the autoclave co-consolidated specimen 10.2.

No statistically significant improvement in joint strength was measured for joints 7 and 9, with an adhesive and CF/PA11 fillet, respectively. The composite fillet may have slightly increased the joint strength in some cases, but this can probably be attributed to an increased amount of resin material available to form a bead of resin in front of the point where the skin and stiffener radius meet, which would reduce the stress concentration. This would be comparable to the small resin fillet in the baseline joints, as pointed out in Figure 4.11a. The fillet quickly separated from the skin or stiffener during testing and after failure of the joint the fillet was still connected to the stiffener in 4 instances and to the skin once. In one sample the fillet separated from the joint completely.

As mentioned in Section 4.3.2, for only three of the six samples with adhesive fillet, the laminate surfaces were plasma treated before bonding, due to size limitations of the plasma treatment equipment. While the samples without plasma treatment failed at a similar applied load as the baseline joint (31.3, 32.0 and 32.2 N/mm), a higher strength was measured for the other samples (34.7, 34.9 and 37.0 N/mm). The specimens that were not plasma treated failed between the skin and fillet, but the other coupons failed between the stiffener and fillet. This failure mode was unexpected, because the stiffener-fillet interface was subjected to lower stresses than the skin-fillet interface, as was determined with finite element analysis. This suggests that plasma treatment of the skin surface led to improved adhesion of the fillet. That adhesion with the stiffener radius was weaker can probably be attributed to a poor setup during the plasma treatment process in which the stiffener surface could not be treated sufficiently. So, although insufficient data is available to conclude that an adhesive fillet could lead to performance increase of a TPC L-joint, it could be worth investigating further. Polyamide is also notoriously difficult to bond, so potentially better results can be achieved for other thermoplastics, such as PEKK or PEEK, as long as good surface treatment before bonding is ensured.

5.3. Finite Element Analysis

This section contains various aspects of the skin-stiffener L-joint studied using the finite element method. In Section 5.3.1 the approach and boundary conditions used are explained and FEM results are compared to the physical test results. The influence of various geometric parameters on joint performance is analyzed in Section 5.3.2 and in Section 5.3.3 the effect of joint geometry and a resin fillet on the shear and out-of-plane stresses in the weld line is studied. A model developed for fatigue analysis of L-joints is briefly described in Section 5.3.4.

5.3.1. Failure Prediction and Crack Growth

Finite element analysis was performed using the ANSYS Parametric Design Language (APDL), which allowed for good control over the mechanical and geometric design parameters in the L-joint. The fundamentals of the code were similar to that described by *Krueger* [119]. The skin-stiffener joint was reduced to a 2D model and plane strain conditions were assumed. Thus, in this model 3D effects were not taken into account, but with a coupon width of 50 mm this was deemed acceptable. By performing 2D instead of 3D analysis, computational time was reduced. Non-linear geometric analysis was performed, which meant that the effects of large deformations were taken into account. 2D 4-node solid PLANE182 elements were used to mesh the skin and stiffener laminates. Plies were modelled with one element in the thickness direction and an in-plane mesh size of between 0.5 mm and 3 mm was used, with the highest mesh density in the weld region. A convergence analysis was performed and when compared to an in-plane mesh length of 0.25 mm throughout the joint, the difference in failure load for the baseline geometry shown in Table 3.2 was less than 0.4% with failure initiating at the same crosshead displacement. Orthotropic material properties were calculated for the 0°, 45° and 90° plies and input separately. The ply material properties used for the CF/PA11 material are listed in Table 5.3.

During testing, the skin was clamped constraining horizontal and vertical displacement, and rotation. However, in photos taken during the tests it was observed that the skin clamps were not perfectly stiff. Therefore, in the finite element model not horizontal fixed constraints were used, but instead COMBIN14 spring elements were attached to the skin nodes on the edges connected to nodes fixed in space. This replicated the deflection in the grips during testing. The stiffness of these springs was determined by comparing the horizontal displacement of the clamps in the finite element model with that observed during testing. In the photos taken during testing of coupon 5.1 a 0.6 mm position difference of the grips was measured right before and after failure of the joint and the same behavior was found in the FE model when a spring stiffness k of 80 (N/mm)/mm was used, equally divided over the nodes at the skin edge. This corresponds to a stiffness of 4.0 kN/mm for a 50 mm wide coupon. A simplified schematic of the boundary conditions applied to the skin in the model is shown in Figure 5.10.

Table 5.3: Material properties of CF/PA11 used in the APDL finite element model.

Property	Units	CF/PA11
Longitudinal modulus E_{11}	GPa	106
Transverse modulus E_{22} and through-thickness E_{33}	GPa	9.8
In-plane shear modulus G_{12} and G_{13}	GPa	4.0
Interlaminar shear modulus G_{23}	GPa	3.5[a]
Poisson's ratio ν_{12} and ν_{13}	—	0.28
Poisson's ratio ν_{23}	—	0.40
Critical mode I strain energy release rate G_{Ic}	N/mm	1.25
Critical mode II strain energy release rate G_{IIc}	N/mm	2.0[b]

[a] G_{23} = 0.5 E_2 / (1 + ν_{23}).
[b] Assumption.

The boundary conditions on the stiffener web were different for the two test setups used during this thesis. For the old setup, in which both horizontal displacement and rotation were restricted, a horizontal constraint was applied to all nodes in the top edge of the web and the vertical displacement was applied to all these nodes. Because this defined the same vertical displacement of the nodes in this edge at any given time, rotation was prevented. However, because in the physical experiments the angle between the skin and stiffener web was not perfectly 90° and because the stiffener grip required the web to vertical, the web first had to be bent into place. This was done by applying a horizontal displacement on the middle node, allowing vertical displacement and rotation, until the top of the web was completely vertical. It was found that this was the case when the applied horizontal displacement was approximately 80% of the distance between the imperfect and ideal position of the web top edge. A schematic of the applied boundary conditions and displacements for the old setup is given in Figure 5.11.

For the new test setup, in which the stiffener web could rotate freely around the load application axis, the horizontal constraint and vertical displacement were applied only to the middle node in the edge. This allowed for rotation of the stiffener around this node. A simplified schematic this new setup is shown Figure 5.12.

For simulating crack growth, the virtual crack closure technique (VCCT) was used, as explained in Section 2.6, with INTER202 2D 4-node cohesive elements in the welded interface. Critical mode I and mode II strain energy release rate values were assigned in the APDL code. G_{Ic} was obtained from the DCB test outlined in Section 5.1 and G_{IIc} was assumed the same as for PEEK. This assumption was deemed acceptable, because the influence of G_{II} on the onset of unstable crack growth was reasonably small (less than 20%) compared to G_I when a G_{IIc} value of 2.0 N/mm was used for the baseline case. The effect of the G_{IIc} value on the failure load is also shown in Figure 5.18 in the next section. When comparing FEA results with physical test results, the size of the welded region was measured from the used test coupon and in the model only the skin and stiffener in the welded region were connected. A parameter was implemented in the code for the unwelded length at the side of the stiffener radius and of the flange tip. As can be seen in Figures 5.6 and 5.7a for none of the welded joints the entire stiffener flange was welded to the skin, which influenced the stiffness and strength of the joint. The crack in the weld line was propagated to the next interface node once the index f in the following linear fracture criterion exceeded 1.0 at the crack tip.

$$f = \frac{G_I}{G_{Ic}} + \frac{G_{II}}{G_{IIc}} \tag{5.2}$$

A linear fracture criterion and relation between the mode I and II failure modes was used, instead of a more complex relation, as, for example, shown in Figure 2.8, because for this CF/PA11 material insufficient data was available. In order to use a more precise fracture criterion, the pure mode II and

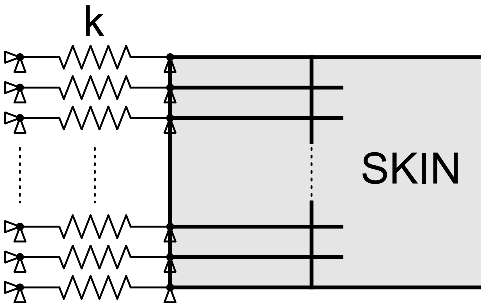

Figure 5.10: Finite element model boundary conditions on skin edges. Each edge node was constrained in the vertical direction and horizontal spring elements were connected between these nodes and nodes fixed in space. A spring stiffness k of 80 (N/mm)/mm was equally divided over these spring elements. Springs were used because in the experiments the skin grips were not perfectly stiff.

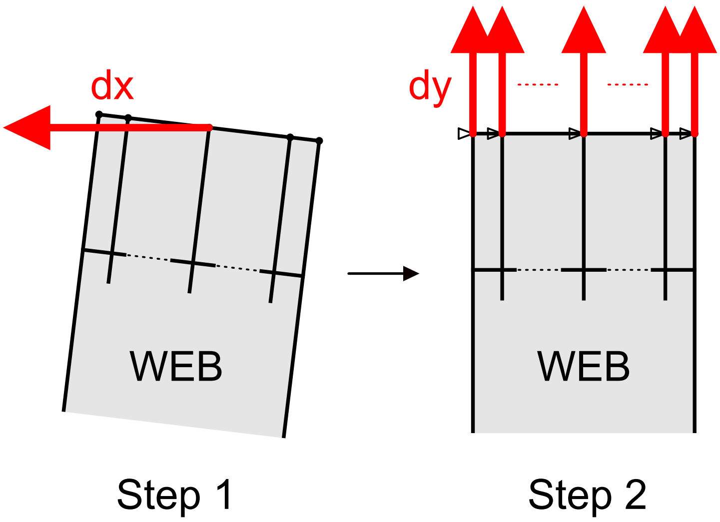

Figure 5.11: Finite element model boundary condition and applied displacement on stiffener web with the old setup. In step 1 a horizontal displacement was applied to the middle node on the top edge until the top section is vertical, as required for the grip. In step 2 a horizontal constraint and vertical displacement was applied to all top edge nodes, preventing rotation of the web.

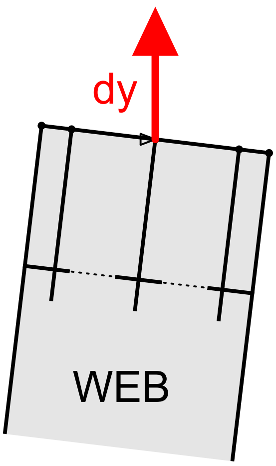

Figure 5.12: Finite element model boundary condition and applied displacement on stiffener web with new test setup. The web was free to rotate around the loading axis, so only a horizontal constraint and vertical displacement was applied to the top edge middle node.

mixed-mode I and II critical strain energy release rate values would need to be obtained, using the end-notched fixture (ENF) and mixed-mode bending (MMB) tests, respectively. These tests, however, were outside the scope of this thesis. It is not possible to state what effect this linear criterion assumption had on the predicted failure behavior of the joints, because the mode I and mode II interaction varies between different materials [120].

In Figure 5.13 force-displacement plots are displayed with the experimental test results of joints 1 and 5 and with the values obtained from the FE model. Because of scatter among the G_{Ic} values obtained from the DCB test, failure was also simulated for the 5% and 95% confidence values, 0.99 N/mm and 1.51 N/mm, respectively. The simulated curves agree well with the experimental data at low displacement, but after a crosshead displacement of approximately 4 mm, the finite element model calculated a stiffer behaviour of the joint. However, this can be explained by a variety of possible causes. The implemented stiffness at the skin grips strongly influenced the curve shape at higher displacements, so if a lower spring constant was used, the finite element results would follow the experimental data more closely. Another possible cause could be the accuracy of the applied boundary conditions in the model at the stiffener web. Some horizontal displacement in the stiffener grip was observed during testing, because the setup was not perfectly stiff, which could have contributed to the difference in stiffness. The FE analysis results are also shown with the assumption that the skin grips are perfectly stiff. As stated previously, this led to a higher joint stiffness and also increased strength. These results show that it is crucial to apply accurate boundary conditions in the finite element model.

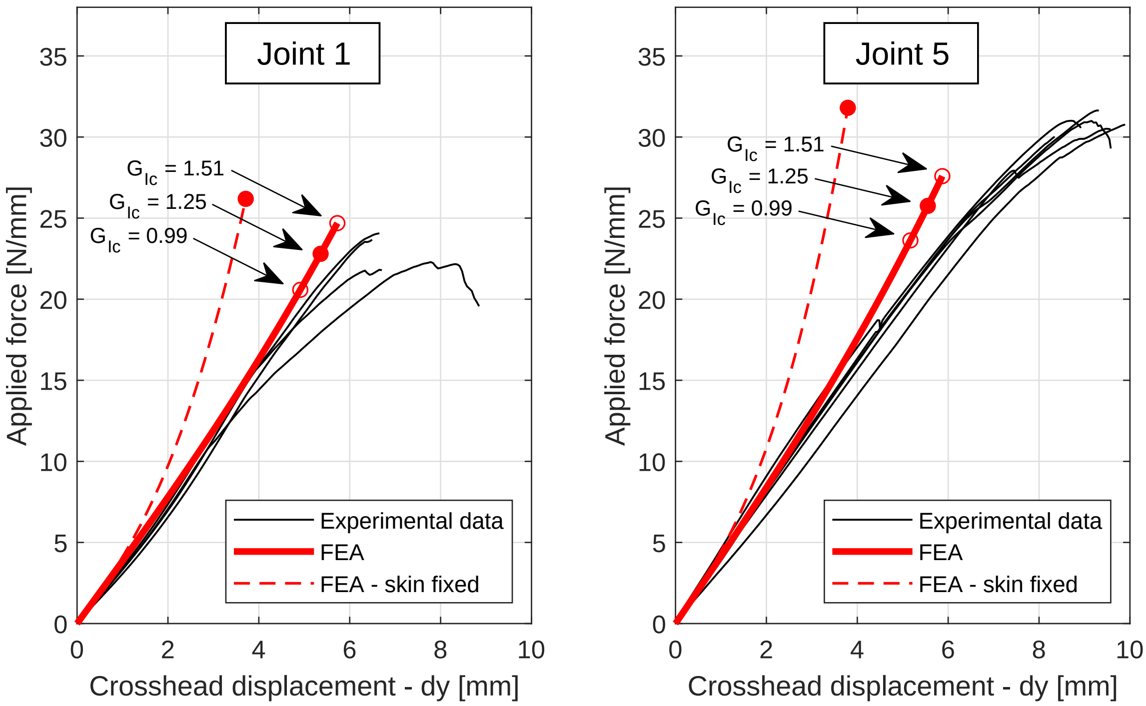

Figure 5.13: The experimental and simulated force-displacement curves of joint 1 and joint 5. The dashed line shows the simulated results when the skin grips were assumed to be fixed (perfectly stiff). The failure loads were calculated for the mean critical strain energy release rate G_{Ic} of 1.25 N/mm obtained from the DCB test, as well as the upper and lower bound of the 95% confidence interval. The experimental displacement was measured by the tensile machine.

For joint 1 the average failure load was 23.0 N/mm and with the finite element model a failure load of 22.8 N/mm was calculated, only 0.8% lower. Using the G_{Ic} 95% confidence interval upper and lower bounds, failure loads of 24.7 N/mm and 20.6 N/mm were found, respectively. The simulated joint strength agrees very well with the test results.

For joint 5 a difference between measured and calculated failure load was found. An average failure load of 30.8 N/mm was measured in the experiments, while from the simulations, using a G_{Ic} value of 1.25 N/mm, a failure load of only 25.8 N/mm was found, 16.5% lower than the experimental results. Even when the upper bound of G_{Ic} in the 95% confidence interval was used, a failure load of only 27.6 N/mm was calculated, 10.5% below the physical test results. This difference can likely be explained from the small squeeze-out resin fillet formed during the induction welding process, as displayed in Figure 4.11a. This geometry at the crack initiation location was different from the pre-crack in the DCB test and in joint 1 and it probably reduced the stress concentration and increased the fracture toughness. A potential approach to implement this small resin fillet would be to appoint a higher G_{Ic} value to the first 1 mm of the fracture path. This was, however, not further investigated in this thesis.

Another APDL finite element model was created in which a fillet was implemented with the geometry shown in Figure 3.1. The fillet was also modelled using 2D 4-node solid PLANE182 elements and the mesh a fine mesh was used, as shown in Figure 5.14a. For this model the VCCT was not used, because the crack path through the fillet was unknown and because the PA11 resin fillet displayed significant plastic behavior, which made the use of the VCCT ineffective. Prediction of the failure load was not attempted for the adhesive and CF/PA11 fillets, because, as was seen in the experiments, failure occurred at the interface with the skin or stiffener and not within the fillet, which only the case for the autoclave co-consolidated joint. The full stress-strain curve of the neat PA11 fillet material was unknown and only the properties related to the elastic-plastic behavior as listed in Table 5.4 were available. A bilinear isotropic hardening model was assumed and the stress-strain properties as shown in Figure 5.14b were used in the model. A Poisson's ratio of 0.42 was assumed.

Table 5.4: Material properties of PA11 fillet [107].

Property	Unit	PA11
Young's modulus E	GPa	1.6
Tensile strength σ	MPa	48
Elongation at break ϵ_T	%	45

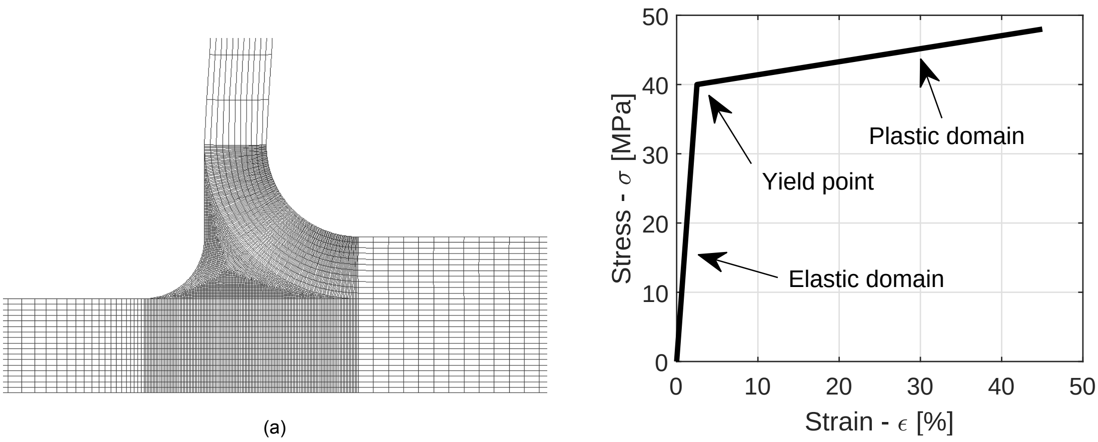

(a)

(b)

Figure 5.14: (a) Mesh of the fillet region used for simulating the force-displacement behavior of the joint (b) Bilinear isotropic hardening model used for the stress-strain behavior of the PA11 fillet in the finite element model.

It was found that failure of the joint with fillet could not be predicted reliably using this model. The high compressive stresses in the lower surface of the skin laminate could be observed, but in order to predict buckling of the lower few plies, as was seen in the test coupons, a failure criterion was needed that would incorporate the interaction between the plies with various orientations. Furthermore, simulating failure in the fillet, which exhibited a strong plastic behavior, was complex and even more so because of high localized bending under the fillet due to the compressive failure in the skin. Investigating and implementing failure criteria for these failure modes were outside the scope of this thesis.

Although failure could not be simulated using the model, it was used to compare the force-displacement curve with the experimental data, as was previously done for joints 1 and 5 in Figure 5.13. The results for the autoclave co-consolidated joint 10 are shown in Figure 5.15. The results from the finite element model are shown for various stiffness values applied to the skin grips, because, as stated in Section 5.2, after testing the second specimen, it was noticed that the grips had moved, so the bolts connecting the skin grips to the base plate were tightened. It can be observed from these simulations that the boundary conditions on the joint during testing have an large influence on the test results.

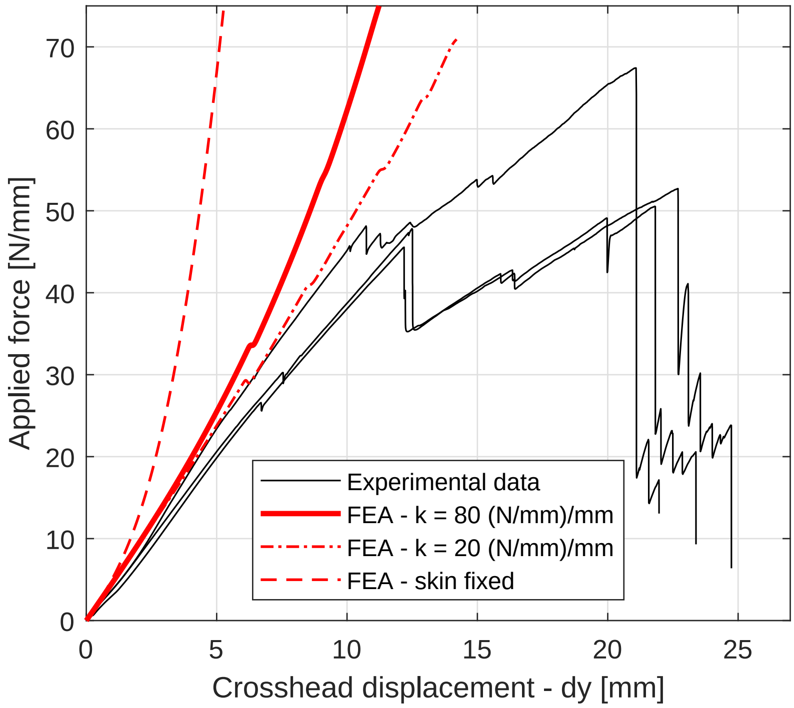

Figure 5.15: The experimental and simulated force-displacement curves of joint 10. Finite element analysis was performed for different assumed stiffness values k for the skin grips. k = 80 (N/mm)/mm had previously been determined in this section. The dashed line shows the simulated results when the skin grips were assumed to be fixed (perfectly stiff) and the dash-dotted line when the grips were assumed less stiff. Failure was not predicted.

5.3.2. Influence of Geometric Parameters

A sensitivity analysis was performed to investigate the influence of various geometric joint parameters on joint strength and displacement until failure. One geometric parameter was changed at a time and the results were compared to the baseline geometry as listed in Table 3.2. The boundary conditions for the new test setup were used, which meant that the stiffener web was free to rotate around the load application point. Thus, the baseline joint for this sensitivity analysis was the same as joint 6. The welded region was assumed to start immediately under the stiffener radius and had a width of 15.5 mm. This left a 10 mm region unwelded, as was measured from the fracture surface of the tested joint. This is also visible in the fracture surface of joint 8 in Figure 5.7a. The same spring constant of 80 (N/mm)/mm for the skin clamps was used, as previously described in Section 5.3.1. The mode I critical strain energy release rate G_{Ic} of 1.25 N/mm was used, as was obtained from the DCB test. As shown in Figure 5.13, this led to an underprediction of the joint strength, but this was deemed acceptable, because this sensitivity analysis was used for comparison between results only. The influence of the following parameters was studied: skin thickness, stiffener thickness, grip length (the separation between the skin grips), web height, the location of the weld bath front and the stiffener corner radius. The influence of an offset in the angle between the skin and stiffener web for the old and new test setup was previously shown in Section 3.4. In the simulations in this section a perfect 90° angle was assumed between the skin and stiffener web. The ply stacking sequence in the laminates was kept constant, so for different skin and stiffener thickness, only the ply thickness was changed.

In Figure 5.16 the results from the sensitivity analysis are shown. In the plots in the left column the calculated failure load and crosshead displacement at failure are shown for the six different tested geometric parameters. The small dots indicate the simulated values and the circle shows the baseline case. The curves are an interpolation from the simulated results. It was found in the simulations that when for the baseline geometry the stiffener thickness was increased beyond 3.5 mm, the delamination crack would first propagate slowly, after which failure occurred abruptly. In the plot the failure load and displacement at failure at the onset of this slow delamination growth is displayed with a solid line. The point of abrupt failure after the crack growth phase is indicated with a dashed line.

In Equation 5.2 the linear failure criterion for this finite element model was given, which showed that failure was dependent on both the mode I and mode II strain energy release rate at the crack tip. In the right column in Figure 5.16 the contribution to failure of both modes is displayed. Thus, for the G_I curve $G_I/G_{Ic} \times 100\%$ is shown and for the G_{II} curve $G_{II}/G_{IIc} \times 100\%$. The value of G_{IIc} was assumed to be 2.0 N/mm, but if this assumption was incorrect and if it was instead lower, the contribution of mode II on failure would be higher, and vice versa. Also, these plots would be different if a non-linear fracture criterion was used. The values are shown for the point at which the delamination crack started propagating, either in a stable or unstable manner. For a stiffener thickness beyond 3.5 mm the crack first propagated slowly before failure occurred, but the curves are shown for the start of stable delamination growth. These plots give an indication on how much the joint is subjected to out-of-plane tension and in-plane shear at failure. Note that when the contribution of G_{II} to failure of the joint is high, it is important to experimentally determine its critical value G_{IIc}. When they joint is almost exclusively subjected to mode I crack opening, only knowing the G_{Ic} should be sufficient. It is important to note the only failure mode that was investigated in this sensitivity study was delamination between the skin and stiffener through the weld line. Compressive failure in the lower skin surface, matrix cracking in the skin and interlaminar tensile failure in the stiffener radius were not taken into account.

The influence of skin thickness on the joint strength was found to be large. For this joint, changing the skin thickness from 3.4 mm to 10.0 mm resulted in a 94.4% failure load increase. Because of the higher bending stiffness of the skin, the deformation of the joint was limited resulting in a reduced peeling effect between the skin and stiffener. This can also be seen in the plot in the right column, which shows that the contribution of mode II was reduced for increased skin thickness. However, for a skin thicker than 6 mm the influence of this interlaminar shear sliding mode was negligible, but an increase in joint strength was still measured. This can be attributed to improved distribution of out-of-plane tensile stresses over the welded region, because of increased stiffness of the skin, thus reducing the peak stresses at the crack tip. This is also visualized in Figure 5.20.

Increased stiffener thickness also showed an improvement in joint strength, but contrary to the previous case, this increased strength occurred with a higher contribution of failure mode II. With increased stiffness of the stiffener the stiffener flange was less compliant with skin deformation, leading to interlaminar shear at the crack tip. That despite this larger mode II contribution the joint became stronger can likely also be attributed to a better stress distribution throughout the weld line as mentioned in the previous paragraph. After the stiffener thickness was increased beyond 3.5 mm, stable crack growth occurred before abrupt failure. For a 4 mm thick stiffener, the crack propagated slowly until a crack length of 12 mm was reached and for the 5 mm thick stiffener, stable crack growth took place throughout the entire weld. It was found that when the stiffener thickness was further increased, eventually the crack would initiate at the other edge of the weld line. This was because the distance between that side of the weld line and the skin grip was shorter than between the crack tip at the stiffener radius and the grip. Therefore, the deformation of the skin at that side was larger and the peeling effect was higher.

Reducing the skin grip separation resulted in a stiffer joint and a smaller displacement before failure. As was the case for increased skin thickness, this reduced skin deflection led to a stronger joint. The difference in joint strength beyond a grip length of 200 mm is very small and this can be attributed to large non-linear deformation of the skin laminate at high crosshead displacements.

The influence of the web height was less pronounced than for some of the other geometric parameters and some joint strength increase was found for a very short web. For taller stiffeners the web

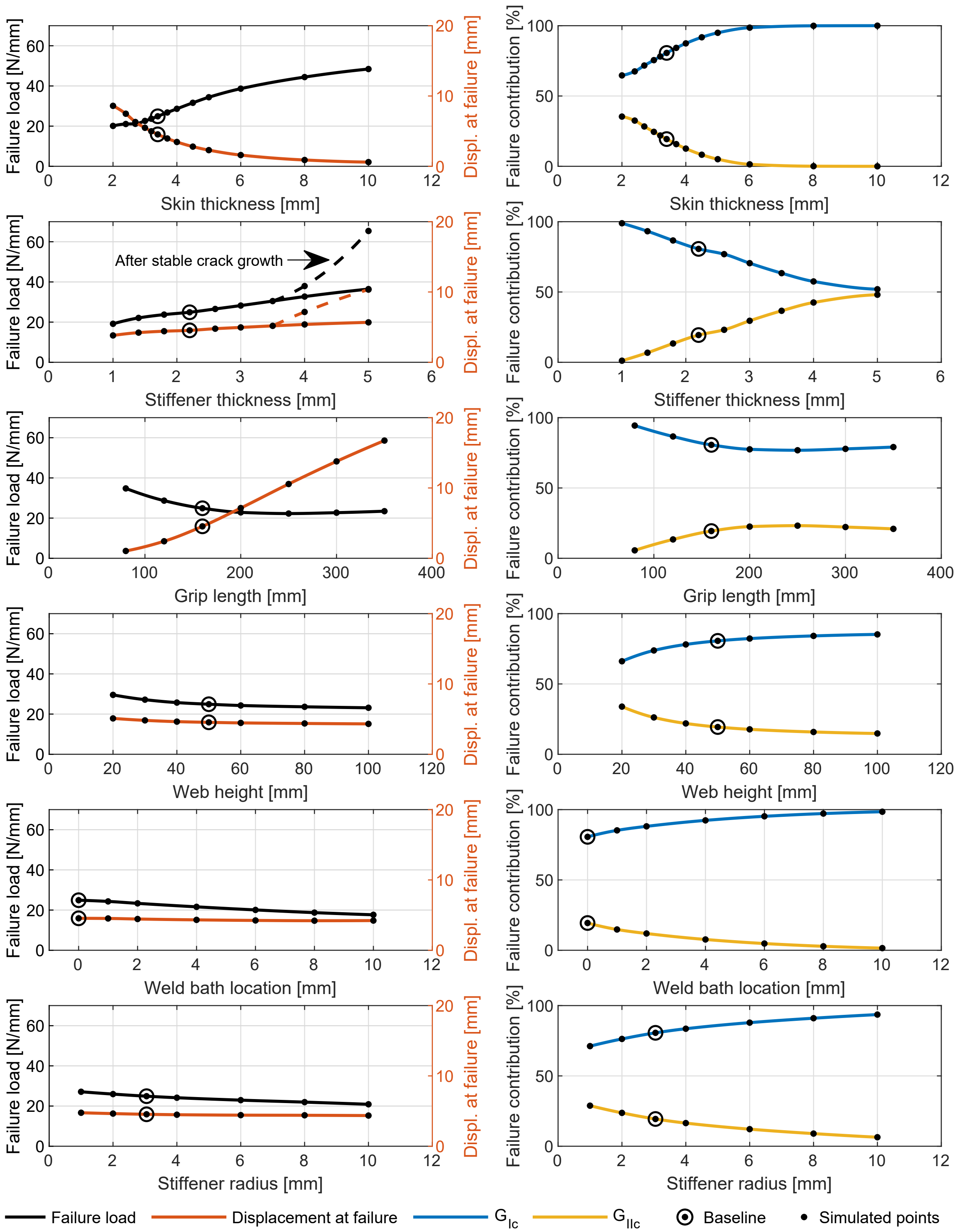

Figure 5.16: The influence of various geometric parameters on the joint failure. Parameters were varied with respect to the baseline geometry and the boundary conditions of the new test setup were used, in which the top edge of the stiffener web was free to rotate. The only failure mode taken into account was crack growth in the weld line. When the stiffener thickness was increased beyond 3.5 mm, the crack propagated slowly before final, abrupt failure. The onset of stable crack growth is shown with a solid line, failure after stable growth with a dashed line.

bent in order to minimize the change in the angle between the flange and web, with the stiffener radius working as a torsional spring. For a very short web, insufficient length was available to comply with the deformation of the skin and stiffener flange and the stiffener radius opened slightly, effectively closing the crack tip. Thus, this effect is strongly dependent on the test setup. Had the stiffener web not been constrained for horizontal displacement, then this strength increase for a shorter web had not occurred.

For the sensitivity analysis on the weld bath location, the weld bath width was 15.5 mm for each simulated point. For example, a weld bath position of 4 mm meant that 4 mm of the skin-stiffener interface remained unwelded near the stiffener radius. As was previously discussed in Section 2.6.2 moving the weld away from the stiffener radius resulted in a weaker joint. As pointed out in Section 5.3.1, the actual joint strength at the 0 mm location should be higher, because a small squeeze-out resin fillet would be formed ahead of the crack, reducing the stress concentration at the crack tip and increasing the fracture toughness at crack initiation.

A similar trend was observed when the stiffener corner radius was increased. The value shown in the figure is the inner radius dimension. When the stiffener radius became larger, the horizontal distance between the loading axis and the weld line was increased. This was similar to the case in which the weld bath location was moved. An advantage, however, of increasing the radius dimension is that it leads to reduced interlaminar tensile stresses in this region, but this was not further investigated.

Because of the large influence of skin and stiffener thickness on joint performance, a sensitivity analysis was performed in which both values where varied. The results of this study are shown in Figure 5.17. The thickest skin and stiffener used for the simulations, 10 mm and 5 mm thick, respectively, resulted in the highest failure load of 85.2 N/mm. When a 2 mm thick skin and 2.2 mm thick stiffener were used, a failure load of only 20.1 N/mm was calculated. As was previously observed, when the stiffener thickness increased beyond a certain point, the crack in the weld line would propagate slowly before final failure. In these cases this seemed to occur once the stiffener thickness exceeded the skin thickness. It was found that the higher this ratio was, the further the crack would propagate before abrupt failure. In this analysis it was assumed that once the remaining connected width reached 2 mm, failure would occur due to in-plane shear and transverse tensile stresses. Due to this assumption, a decrease in failure load was found when the skin thickness was very small compared to the stiffener. This is possibly the result of large non-linear deformations of the skin, because of its low bending stiffness.

In Figure 5.18 the simulated failure load is shown for different values of G_{Ic} and G_{IIc} for the baseline joint geometry. This plot shows that for this geometry the influence of the mode I fracture toughness value on the failure load is larger than the mode II value. If the assumption of G_{IIc} was incorrect and it was 1.0 N/mm instead of 2.0 N/mm the failure load would be only 8% lower for this baseline case. The failure load was also calculated using the G_{Ic} and G_{IIc} values of several thermoset and thermoplastic composites and adhesive materials [120, 121]. These results highlight that the pull-off strength of thermoplastic L-joints is higher than that of their thermoset counterparts, assuming they are both co-consolidated or welded. It should be noted here that for all materials a linear fracture criterion was used, which could have led to a too conservative prediction of the thermoset material failure load, according to the mixed-mode behavior reported by *Reeder* [120].

5.3.3. Weld Line Stresses

An APDL code was developed in which the in-plane shear and out-of-plane tensile stresses in the weld line could be calculated. The purpose of this model was to determine the stress distribution within the weld line and the influence of geometric parameters and fillet implementation on these stresses. The finite element model was largely the same as described in Section 5.3.1, with a few differences. VCCT was not incorporated in the model, but instead the baseline joint failure load determined from the previous model was used as input. A 0.1 mm thick skin-stiffener interface divided into ten element rows was created in the model, because this provided more reliable results than when this interface layer was not used. When the skin and stiffener were connected directly, as was the case in the FE model in the previous sections, the difference between the total interface stresses and reaction forces at the clamps was very high in this model. When this thin interface layer was modelled, this error was

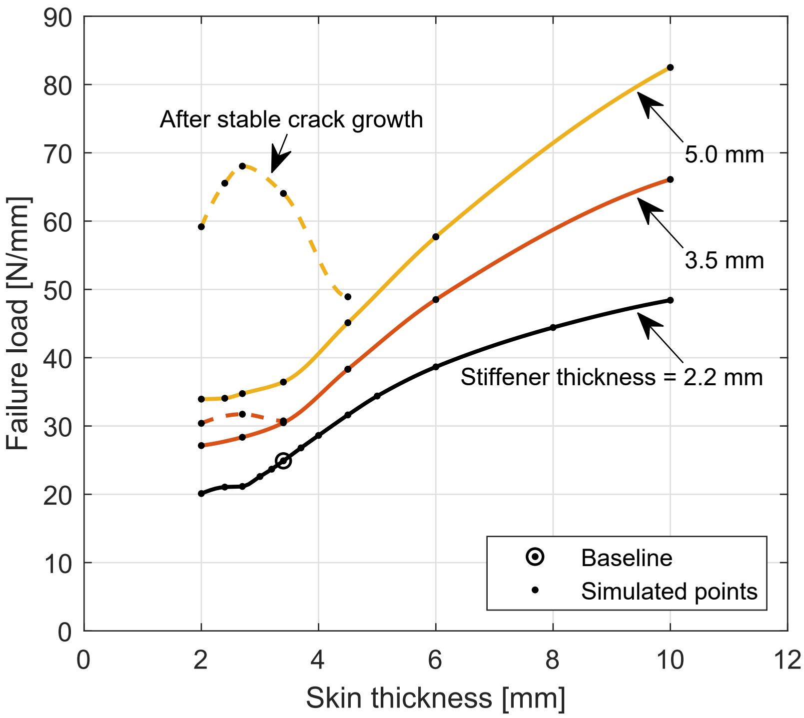

Figure 5.17: The effect of skin and stiffener thickness on failure load. The solid line shows the onset of stable crack growth or the load at which abrupt failure occurred. The dashed line represents the ultimate failure load after a phase of stable crack propagation. If, through stable crack propagation, a crack length of 13.5 mm was reached (of the 15.5 mm weld width), failure was assumed due to in-plane shear and transverse tensile stresses.

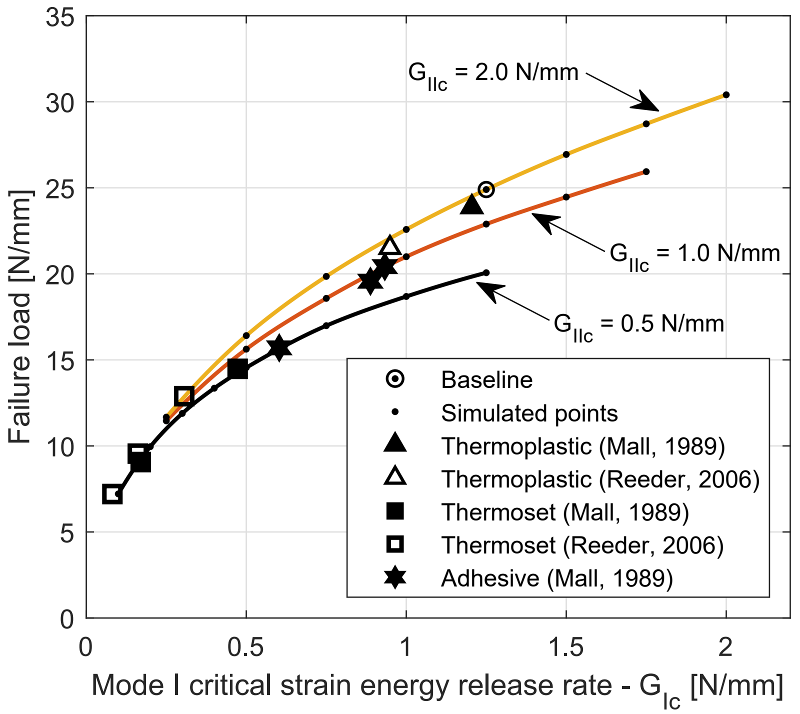

Figure 5.18: The effect of mode I and II fracture toughness on failure load for the baseline joint geometry. The joint strength was also calculated using the reported fracture toughness values of several thermoset and thermoplastic composites and adhesive materials [120, 121]. For all simulations a linear failure criterion was assumed, which could have led to a too conservative prediction of the joint performance.

reduced to less than 1%. Because no actual resin rich weld line was present in the physical coupons, the modelled interface was appointed only the elastic material properties of a neat PA11 resin, as given in Table 5.4. If the plastic behavior of the resin material was used, then the plastic zone and redistribution of stresses would be too large and not comparable to the experiments. A 15.5 mm wide weld bath was used, the same as in Section 5.3.2, and it was divided into 310 elements with the highest mesh density near the edges of the weld, as shown in Figure 5.19a. The stresses were measured in the middle of the interface layer, between the fifth and sixth element.

This model was then expanded so that the stresses in the skin-fillet interface could be obtained as well. Also in this case a 0.1 mm thick interface was modelled, but instead the same plastic material properties as the fillet were assigned. The bilinear isotropic hardening model as shown in Figure 5.14b was used. The fillet mesh was made very fine and the elements were refined near the edges of the interfaces as shown in Figure 5.19b.

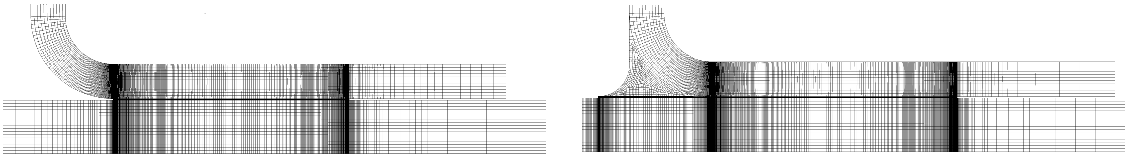

(a) (b)

Figure 5.19: (a) Mesh without fillet (b) Mesh with fillet.

In Figure 5.20 the out-of-plane tensile stresses are shown for the skin-stiffener joint with a skin thickness of 3.4 mm, 6 mm and 10 mm. The applied loading for each of these cases is 24.9 N/mm, the failure load of the baseline joint with a 3.4 mm thick skin, as shown in the first plot in Figure 5.16. As mentioned in Section 5.3.2, the joint strength increase when a thicker skin was used could be attributed to a better distribution of stresses within the weld line, reducing the peak stresses. This can be seen in the plot, in which the peaks are lower and the out-of-plane tensile stresses are more constant in the middle. Because the thicker skin is stiffer, its deformation under the same applied loading is less, leading to less deformation near the edges of the weld line and therefore a better distribution throughout the joint. Also, the transverse tensile strength of PA11 is shown in the figure, but due to plasticity of the resin material, failure does not occur as soon as the transverse tensile strength is exceeded at the crack tip.

In Figure 5.21 the effect of the neat PA11 resin fillet on the out-of-plane tensile and in-plane shear stresses in the weld line are shown. In these plots x = 0 mm represents the position of the weld line edge nearest to the stiffener radius. When a resin fillet was used in the model, the high out-of-plane tensile stress peak at this location was completely removed. The minor stress peak at x = 15.5 mm remained unchanged. The peak shear stress increased, but still remained far below the material in-plane shear strength of 85 MPa. These results indicate that failure is more likely to occur at the stiffener flange tip when a resin fillet is used, particularly when the stiffener is relatively thick, as discussed in Section 5.3.2, so this should be kept in mind when using a fillet in the joint design. If these stresses become critical in the design, they could be reduced by chamfering the stiffener flange or by adding an additional fillet here, as mentioned in Section 2.4.2.

5.3.4. Fatigue Analysis

Using the finite element model described in Section 5.3.1, a procedure was developed for predicting the fatigue life of the L-joint and the crack length after a certain number of cycles. Software is available for performing such analysis, also to a certain extend in APDL using the `CGROW,FCG` command, but this does not always give a full insight on the underlying calculations. For the procedure developed in this thesis, first the mode I and II strain energy release rates were calculated at the crack tip for a range of crack lengths and applied displacements, after which this data was processed in a Excel spreadsheet using the Paris law described in Section 2.6.3. Because no fatigue tests were performed in this thesis and no relevant data was available in literature, the results found using this model were not validated. For this reason the procedure and the results are provided in Appendix B.

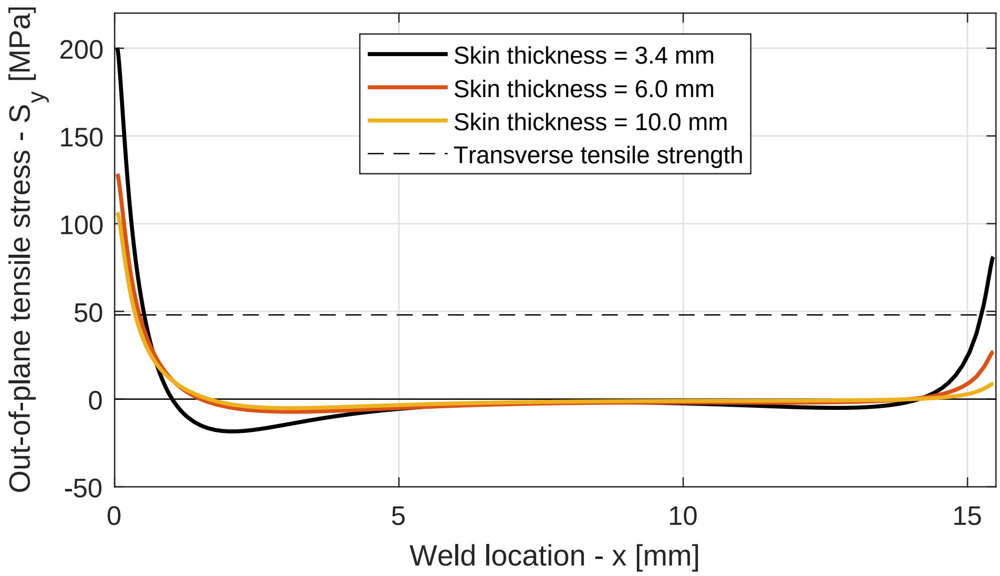

Figure 5.20: Out-of-plane tensile stresses in the weld line for a skin thickness of 3.4 mm, 6.0 mm and 10.0 mm. x = 0 is located at the edge of the skin-stiffener interface near the stiffener radius. For increase skin thickness, the peak stresses were reduced and the stresses were better distributed over the joint.

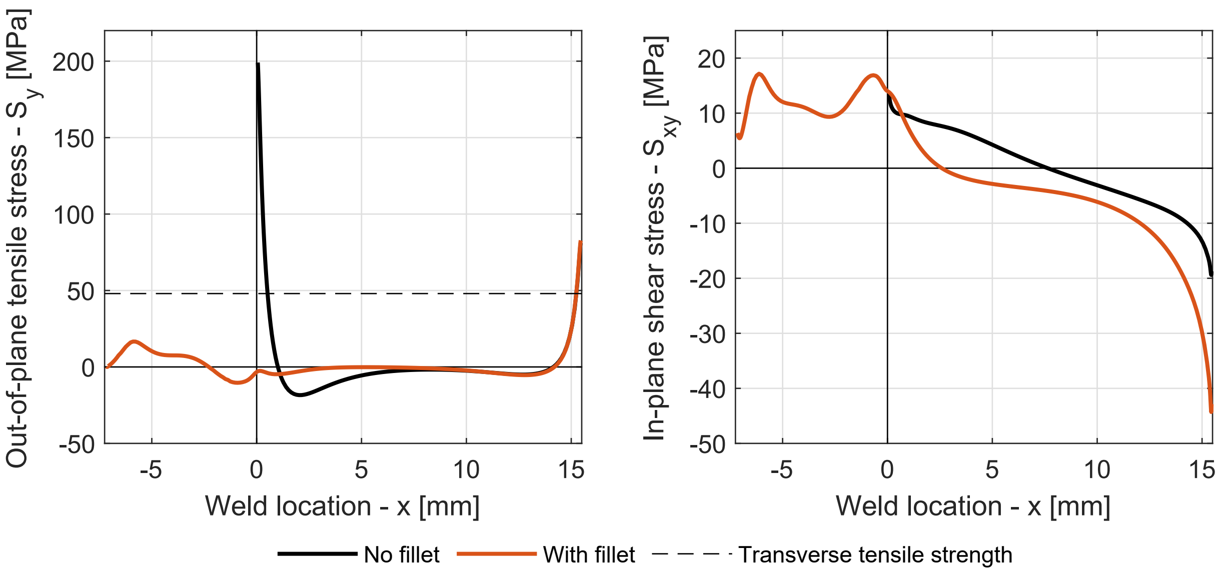

Figure 5.21: Out-of-plane tensile and in-plane shear stresses in the weld line with and without near resin fillet. x = 0 is located at the edge of the skin-stiffener interface near the stiffener radius. The out-of-plane tensile stress peak at this location was completely removed when a neat PA11 resin fillet was used. The peak shear stress increased, but remained below the in-plane shear strength of the CF/PA11 material of 85 MPa.

5.4. Discussion

In this chapter the experimental test results were provided and the finite element models were described. From the experimental test results it was concluded that by implementing a neat thermoplastic resin fillet in an induction welded L-joint, joint strength can be increased significantly. For the autoclave co-consolidated joint, an average failure load 80.9% higher than the baseline configuration was found and for one of the induction welded joints in which the neat resin fillet was attached to the stiffener with a hot air tool before welding, a performance increase of 35.4% was measured. The consistency of this fillet along the joint and the shape after processing were poor, so through better process control while attaching the fillet to the stiffener radius, better results can be expected. During testing of the autoclave co-consolidated joint, the lower skin surface failed in compression before ultimate failure in the fillet and due to this compressive failure, the skin laminate bent excessively under the fillet, which resulted in high localized stressed in the fillet. A larger performance increase from the resin fillet can likely be achieved if compressive failure in the skin is prevented. In their study on the effect of adhesive fillets in adhesively bonded CF/epoxy L-joints, *Feih and Shercliff* [86] used a 10 mm thick skin and 3.7 mm thick stiffener. In their experiments no compressive failure in the skin occurred, because the amount of bending was small, but instead matrix cracking in the skin and stiffener and delamination in the skin were observed before ultimate failure. These did, however, not lead to large deformations in the joint, as was the case for the co-consolidated joint in this thesis. Although increasing the stiffness of the joint by increasing the skin thickness can help in determining the ultimate strength of the fillet in an L-joint, it can also lead to the test being less representative of a realistic joint. Also, in the case of induction welding, a joint with a thick skin could be difficult to fabricate. So, if the purpose of the test is to find the ultimate strength of the fillet, based on the sensitivity analysis in Section 5.3.2, it would be recommended to increase the skin and stiffener thickness to its practical limit and to use a small separation between the skin grips to minimize bending of the skin. If the goal of the experiment is to find the design allowables of a specific joint geometry, it would be acceptable or even desirable that the fillet is not the critical failure location. In order to limit the weight penalty for a skin-stiffener panel, the skin can also be thickened only locally under the stiffener. This would reduce bending at the weld interface and the increased stiffness of the skin in that region would lead to better distribution of stresses in the weld line and reduce the peak stresses. This was, however, not further studied in this thesis.

After the experiments it was noted that the skin grips were not perfectly stiff, which led to the grips being pulled towards each other during testing. Because of this, the crosshead displacement until failure measured during the experiments was nearly twice as high as calculated using finite element analysis for the baseline joint. To account for this, the fixed horizontal constraints in the finite element model were replaced by spring elements and the stiffness of these element was determined by comparing the grip displacement in the model for various stiffness values with photos taken during testing of one of the baseline joints. Comparison between the experimental and simulated data showed that this approach was effective in reducing the difference in joint stiffness, but it was not possible to determine this spring stiffness with high accuracy. The experiments were performed on several different days during which the grips were repositioned and the bolts were retightened multiple times and the pretension in the bolts was not measured or controlled. During testing of the autoclave co-consolidated joint after the second coupon it was observed that the grips had moved, so they were realigned and the bolts were fixed tighter. This then resulted in the third test coupon exhibiting a stiffer behavior. If the grips would have been perfectly stiff, the amount of bending of the skin would have been less, which would have prevented the lower skin surface from failing in compression, or at least this would have occurred at a higher load. Thus, for reliable, consistent and predictable test results, the skin grip design is very important. Particularly when comparing this test to a section of a skin-stiffened panel in an aircraft for determining design allowables, it is important to prevent any horizontal displacement of the grips, because such displacement does not take place in this real-life structure. This flaw in the test setup can be avoided using a variety of solutions. A stiff beam could be placed between the grips if a clamping system is used where the grips rely on friction in a guide rail, as was the case for this thesis. Better would be to use a setup where the clamps are positioned through mechanical interlocking or with thick bolts directly through holes in the guide rail.

The APDL finite element model developed for predicting failure of the induction welded L-joint worked well and was efficient, requiring no more than a few minutes per simulation, but further improvement is possible. As discussed previously, when the skin-stiffener interface near the stiffener radius is heated sufficiently during welding, a small squeeze-out resin fillet can be formed, as shown in Figure 4.11a, resulting in an increased fracture toughness. This was shown in Figure 5.13, where in joint 1 an unwelded region, effectively a pre-crack, was located under the stiffener radius, while in joint 5 a small resin fillet was formed. A method for implementing this in the finite element model would be to choose a semi-empirical fracture toughness value for the first 1 mm of the weld line, higher than for the rest of the interface. This value could be selected through trial and error in which the resulting failure load is compared to experimental data, for example of baseline joints 5 or 6. The only failure mode investigated using the finite element model was delamination fracture growth through the weld line, which was acceptable for joints without fillet, but during testing of the autoclave co-consolidated joint with a neat PA11 fillet, other failure modes occurred. Compressive failure in the skin and failure of the resin fillet could not be accurately predicted. In the model it could be calculated when the axial compressive stress in the 0° ply closest to the lower skin surface exceeded the compressive failure strength, but this occurred far before failure was observed in the experiments. The surrounding plies delayed fiber buckling in this 0° ply and this ply interaction is complex to simulate and was outside the scope of this thesis. Also, predicting failure in the fillet is difficult, as outlined by *Feih and Shercliff* [86], particularly because of the strongly plastic behavior of the neat PA11 material. Furthermore, no data on the plastic behavior of this fillet material was available.

The results found in the sensitivity study agree well with available literature. *Van Ingen et al.* [5] had reported that for an induction welded L-joint the coil position and therefore the weld bath position directly affects the joint strength under pull-off loading. They showed that the failure load decreases when the welded region is located further away from the stiffener radius. This corresponds with the results shown in Figure 5.16. *Pappadà et al.* [28, 52] reported pull-off strengths for induction welded L-joints of 9.6 and 12.9 N/mm and *Feih and Shercliff* [86] measured an average failure load of 79.6 N/mm for adhesively bonded L-joints when the small fillet as shown in in Figure 2.6 was used, up to a maximum of 252 N/mm with a fillet radius of 3 mm. In the first case a 1.2 mm thick skin and stiffener were used, while in the second case the skin and stiffener were 10 and 3.7 mm thick, respectively. As shown in Figure 5.17 the influence of the skin and stiffener thickness on the joint strength is large and for this reason the test results in this thesis can not be compared directly with those in literature, where test configurations vary widely. Because in [86] no results where provided for a specimen without adhesive fillet, the performance increase from such a fillet compared to a baseline geometry can not be compared with the results found in this thesis.

The work performed in this thesis could be expanded to other joint types without major obstacles. As was previously discussed in Section 2.3, simple stiffener geometries are preferred for thermoplastic composites and for C- and Z-stiffeners, only the weld tooling should be modified and the method for implementing a resin fillet could be the same. Also for omega-stiffeners, a fillet could be added before welding, but this would require a complete redesign of the tooling, in order to apply sufficient pressure on the fillet region from within the omega-profile. Furthermore, for testing of this joint the stiffener grip setup should be vastly different, but due to its symmetry, its horizontal and rotational constraints are less relevant. Also, for the finite element model no major changes would be required and only the geometry of the joint and boundary conditions of the stiffener grip would have to be modified. For T- and J-joints a neat resin fillet could also be used and it could be autoclave co-consolidated with the stiffener in a tool before welding.

In this thesis only one fillet shape was used, with a 2 mm radius. However, as shown by *Feih and Shercliff* [86], a larger fillet could lead to a higher joint strength. As explained in Section 3.3, increasing the fillet size would lead to a larger area that should be welded, but this issue can be solved in different ways. The coil geometry could be changed in order to increase the weld bath width or two weld runs can performed over the joint, instead of one. This would also allow for using different power settings for both runs, one at the skin-fillet interface and one at the skin-stiffener interface. This was not further investigated in this thesis.

6

Conclusion and Recommendations

In this chapter the work performed during this thesis is summarized and the conclusions that can be drawn from the processes and results are stated. This is followed by recommendations for future work on the use of a fillet in induction welded carbon fiber reinforced joints and on failure prediction of L-joints. First, the goals of this thesis are reiterated.

6.1. Research Goals and Objectives

The primary goals of this thesis were to estimate the expected static joint strength of induction welded unidirectional carbon fiber reinforced thermoplastic L-joints under pull-off loading and to develop a methodology to manufacture and test specimens which can approach or exceed this strength. The following objectives were met to achieve these goals:

1. Find testing methodologies that can be used or modified to test these joints under pull-off loading.
2. Estimate the expected static joint strength based on data available in literature or experiments.
3. Determine which geometric parameters have the largest influence on joint performance.
4. Determine to what extend physical tests approach or exceed the predicted joint strength.

6.2. Summary and Conclusions

Summary

Unidirectional carbon fiber reinforced thermoplastic nylon/polyamide-11 (PA11) skin and L-stiffener laminates were hot pressed and were joined using the induction welding technology developed at Kok & Van Engelen Composite Structures (KVE). In an attempt to increase joint performance by reducing or removing the high stress concentration at the edge of the weld line under pull-off loading, various methods of implementing a fillet between the skin and stiffener radius were investigated. This procedure had previously been used to greatly increase the pull-off failure load of adhesively bonded CF/epoxy joints [86]. Experiments were performed with neat PA11 and PA12 thermoplastic resin, toughened methacrylate Araldite 2048-1 adhesive and quasi-isotropic CF/PA11 fillets. In a first attempt to implement a fillet, a selective laser sintered (SLS) 3D printed PA12 profile was placed in the weld tooling with the skin and stiffener, but insufficient heat was generated between the fillet and stiffener radius. In two subsequent attempts an SLS neat PA11 fillet was connected to the stiffener before induction welding using a hot air tool. In the first case, the fillet was not positioned straight and the fillet was badly deformed, but good diffusion between the resin material in the skin and fillet had been achieved. In the second case, the fillet shape was more consistent, but diffusion between the skin and fillet material was limited. The results from these experiments were compared with an autoclave co-consolidated joint, also with a neat PA11 fillet. The CF/PA11 fillet was attached to the stiffener using a hot air tool before inducting welding as well and the adhesive fillet was applied after the welding process. Due to size limitations of the plasma treatment apparatus the laminate surfaces of only three of the six coupons with adhesive fillet were plasma treated before bonding.

Two test setups were used with different boundary conditions on the stiffener web. A setup that was available at the Delft Aerospace Structures and Materials Laboratory (DASML), in which the stiffener web was constrained in horizontal displacement and rotation, was compared with a new setup in which the web was free to rotate around the loading axis. The aim of this new setup was to eliminate some of the internal stresses introduced by the web grip and to reduce the effect of undesired spring back in the stiffener, created during the press-forming and welding processes, on the joint failure load.

An ANSYS Parametric Design Language (APDL) finite element model was developed, which relied on the virtual crack closure technique (VCCT) for predicting the strength of an induction welded L-joint without fillet. A sensitivity analysis was performed using this model to determine the influence of geometric joint parameters on joint strength. A baseline configuration was used in which one parameter was changed at a time. A delamination crack propagated once the strain energy release rate at the crack tip exceeded a critical value and this consisted of an out-of-plane tension mode I component and an in-plane sliding shear mode II component. The CF/PA11 critical mode I value, G_{Ic}, was obtained experimentally using the double cantilever beam (DCB) test and was found to be 1.25 N/mm (CV = 12.8%) at visible crack onset after creating a pre-crack. The critical mode II value, G_{IIc}, as well as some other material properties, were assumed based on literature. This was deemed acceptable, because failure of the joint was dominant in mode I. A finite element model for predicting failure in a joint with fillet was not developed. Firstly, no validation data was available, because all welded joints with PA11 fillet failed in the skin-fillet interface and not within the fillet due to imperfections and the autoclave co-consolidated joint experienced compressive failure in the skin, strongly affecting the subsequent failure of the fillet. Secondly, accurately predicting compressive failure in the skin under bending and failure of the fillet, which exhibits a strong plastic behavior, is complex [86] and was outside the scope of this thesis.

Conclusions

For the joint with the deformed and poorly positioned neat PA11 fillet, but in which good diffusion had been achieved between the skin and fillet material, the average pull-off failure load was 41.8 N/mm (CV = 7.8%), 35.4% higher than the baseline joint without fillet. For the joint with a more consistent fillet, but with limited diffusion between fillet and skin, the average failure load was 35.4 N/mm (CV = 4.1%), 12.4% higher than the baseline. The lower failure load for the second case was attributed to insufficient heating in the skin-fillet interface. Further welding trials are required to improve the quality of the fillet region. For the autoclave co-consolidated joint an average ultimate strength of 56.9 N/mm (CV = 13.2%) was recorded, 80.9% higher than the baseline. Higher values could have been reached if the bottom side of the skin laminate had not failed in compression, causing out-of-plane fiber buckling at 47.0 N/mm (CV = 2.3%). These experiments showed that there is potential for significant performance increase compared to the baseline joint when the process of implementing the fillet in the induction welded joint is improved and the fillet is placed on the stiffener correctly and consistently, its geometry is retained and good diffusion between the fillet and laminate materials is achieved.

For the adhesive and CF/PA11 fillets, no statistically significant improvement in joint performance compared to the baseline joints was measured. In both cases, failure occurred between the fillet and the skin or stiffener laminates, while in the co-consolidated joint, which had the highest strength, failure took place within the fillet. For the three specimens with adhesive fillet, where the laminates had been plasma treated, a 11.6% higher average failure load was measured than for those that had not been plasma treated. This suggests that with high quality surface treatment some improvement can be expected when an adhesive fillet is used in a CF/thermoplastic L-joint, but this was not proven in this thesis. It should be noted that nylon exhibits very poor bonding characteristics, worse than most other thermoplastics, so potentially better results can be obtained for other thermoplastic composites. Although possibly some strength improvement can be achieved with an adhesive fillet, it is not the preferred method for various reasons. It requires elaborate pre-treatment steps, it is susceptible to contaminants and moisture and inspection can be difficult.

The simulated and experimental force-displacement curves agreed well for joint 1, in which a small unwelded region was present near the stiffener radius, and the failure load calculated using the finite element model (22.8 N/mm) was only 0.8% lower than the average experimental strength (23.0 N/mm). For joint 5, the simulated failure load (25.8 N/mm) was 16.5% lower than the average failure obtained from the experiments (30.8 N/mm), but this can likely be attributed to a small squeeze-out resin fillet formed ahead of the welded skin-stiffener interface during the induction welding process. This error can be reduced by attributing a higher mode I critical strain energy release rate to the first part of the crack path in the model.

The sensitivity analysis showed that increasing the skin and stiffener thickness results in a stronger joint. Simulations were performed in which both skin and stiffener thickness were varied and for a joint with a 2.0 mm thick skin and 2.2 mm thick stiffener a failure load of 20.1 N/mm was calculated, while for a joint with a 10.0 mm thick skin and 5.0 mm thick stiffener a failure load of 82.5 N/mm was found. This increase in joint strength can be attributed to a reduction in bending of the skin and stiffener due to increased stiffness, which leads to less pronounced peeling effects at the weld line edge. Also, the higher stiffness of the laminates leads to a better distribution of out-of-plane tensile stresses within the weld line and a reduction of the peak stresses at the crack tip. Reducing the separation between the skin grips also leads to increased joint strength, because the amount of skin bending is reduced, but for the baseline geometry there is almost no difference in failure load once the grip separation is above 200 mm, because of non-linear bending effects in the skin.

If the skin-stiffener interface cannot be welded over its full width, the position of the weld bath is important. The highest joint strength is obtained when the weld bath starts directly under the stiffener radius, also because this can lead to a small squeeze-out resin fillet ahead of the weld line, which reduces the stress concentration and therefore delays fracture onset. The sensitivity analysis also showed that the new test setup developed for this thesis, in which the joint is free to rotate around the loading axis at the stiffener web, greatly reduces the effect of spring back in the stiffener on the pull-off failure load. For the old setup, in which this rotation is constrained, the pull-off failure load with a spring back angle of -4° is 37.8% higher than with a spring back angle of 4°. With the new setup this difference is only -3.6%. Because for the old setup the web has to be at a 90° angle in the web grip with respect to the skin, internal bending moments are introduced, causing either opening or closing of the weld line crack tip, depending on the spring back direction.

Although increasing the skin and stiffener thickness results in a higher joint strength, along with changing these parameters comes a weight penalty. This penalty can be reduced by increasing the skin thickness only locally under the stiffener, but this also adds some complexity to the structure and joint. Also, increasing the skin and stiffener thickness can make induction welding more difficult. Reducing stiffener spacing, comparable to reduced grip length in a coupon test, will likely also lead to increased weight of the structure, because more stiffeners are required. Implementing a resin fillet, however, has a very small effect on the mass of the overall structure. The neat PA11 fillet increased the weight of the baseline skin-stiffener joint used in this thesis by less than 0.5%. If an efficient and cost-effective method is developed to join the fillet to the stiffener before welding, little extra cost and complexity would be added to the process. A thermoplastic resin fillet can also be applied to other stiffener types, as well as other structural elements, such as ribs and spars.

6.3. Recommendations

Various aspects related to induction welded CF/thermoplastic L-joints were studied in this thesis. However, due to limitations in time and resources, boundaries had to set. Therefore, recommendations for future work related to this topic are provided in this section.

Carbon fiber reinforced polyamide was used in this thesis, but this material is not one of the aerospace grade high performance thermoplastics used in primary aircraft structures. It is recommended to further expand on this research with PEKK or PEEK, with in particular the fillet implementation process. The fiber volume fraction in most CF/PEKK and CF/PEEK tapes is higher than in the material used in this research and also the melting temperature is higher. The melting temperature of PA11 is 183°C [12] and for PEKK this is 337°C [13]. These properties, as well as strength and stiffness characteristics, have an influence on for example bending of the skin laminate and the onset of compressive failure in the skin, as was observed in this thesis. Also, the formation of a small resin fillet ahead of the weld line due to resin squeeze-out during welding can be affected by the material fiber volume fraction and other material properties.

Further investigation on implementing the neat resin fillet in the joint is recommended. In this thesis it was attempted to join a neat resin fillet to both the skin and stiffener during welding, but due to insufficient heating in the stiffener-fillet interface this was not successful. However, only a limited number of induction welding parameters were varied during these experiments, so it can not be said with certainty that this method can never lead to a good joint. Possibly by using a different coil geometry or by moving the coil closer to the laminate a better temperature distribution around the fillet can be achieved. For further experiments, the fillet was attached to the stiffener radius before welding, by blowing hot air between the components and then pressing them together. This was effective, but placement of the fillet was not very consistent and the fillet did not fully retain its cross-sectional profile. Also, because the neat thermoplastic resin fillets in this thesis were fabricated by 3D printing, the edges were slightly rounded and the material was somewhat porous. For a good joint, however, it is important that the fillet profile perfectly transits into the skin and stiffener surface, as was observed in micrographs of the autoclave co-consolidated joint. Overmolding is a promising method for placing a fillet on the stiffener in a consistent manner and with a good surface profile. This method would also allow for the use of short fiber reinforced material in the fillet, which was not used in this research. Furthermore, only one fillet geometry was studied in this thesis, while research performed by *Feih and Shercliff* [86] showed that a larger fillet leads to increased joint performance. For this reason it is recommended to study the effect of different thermoplastic fillet geometries as well.

During the course of this thesis project, only quasi-static pull-off tests were performed. For aerospace structures, however, fatigue design allowables are very important, so it is recommended to perform fatigue experiments on the joints with fillet. Also, in this thesis a method for predicting the fatigue life of L-joints without fillet was described, but this method was not validated. This method could be a valuable tool for predicting the influence of various geometric and material parameters on the fatigue performance of the joint, but for this, pull-off experiments under cyclic loading should be performed. Also worth investigation would be the effect of the fillet under shear or mixed-mode loading conditions. Possibly a modified Arcan test setup can be used for this.

A

L-joint pull-off test results

Table A.1 lists the quasi-static pull-off test results for joints 1–5, which were tested using the old test setup, in which the stiffener web was constrained in horizontal displacement and rotation. In Table A.2 the results are given for joints 6–10, for which the new test setup was used, in which the stiffener web was free to rotate around the loading axis. A negative spring back angle means that the angle between the stiffener flange and web was smaller than 90°.

Table A.1: Quasi-static pull-off test results of L-joints 1–5. These joints were loaded using the old test setup.

Sample	Width [mm]	Skin thickness [mm]	Stiffener thickness [mm]	Spring back angle [°]	Failure load [N]	Failure load [N/mm]
1.1	51.56	3.23	2.00	-2.0	1150	22.3
1.2	51.07	3.16	2.03	-3.0	1115	21.8
1.3	49.36	3.13	2.05	-3.0	1189	24.1
1.4	48.94	3.12	2.07	-2.0	1160	23.7
2.1	51.02	3.26	2.15	-2.5	1304	25.6
2.2	50.99	3.18	2.15	-3.0	1337	26.2
2.3	50.86	3.14	2.13	-3.0	1300	25.6
3.1	51.41	3.24	2.11	-2.0	1509	29.4
3.2	50.77	3.14	2.13	-2.0	1474	29.0
4.1	51.08	3.21	2.21	-2.0	2100	41.1
4.2	51.05	3.17	2.18	-2.5	2410	47.2
4.3	50.86	3.12	2.15	-2.0	1974	38.8
4.4	50.92	3.11	2.12	-2.0	2032	39.9
5.1	50.31	3.19	2.00	-2.0	1560	31.0
5.2	50.23	3.16	2.00	-2.5	1511	30.1
5.3	50.30	3.14	2.00	-2.5	1548	30.8
5.4	50.27	3.13	2.01	-2.5	1535	30.5
5.5	50.38	3.12	2.03	-2.0	1562	31.0
5.6	49.93	3.13	2.02	-2.0	1580	31.6

Table A.2: Quasi-static pull-off test results of L-joints 6–10. These joints were loaded using the new test setup.

Sample	Width [mm]	Skin thickness [mm]	Stiffener thickness [mm]	Spring back angle [°]	Failure load [N]	Failure load [N/mm]
6.1	50.23	3.21	2.01	-2.5	1591	31.7
6.2	50.34	3.16	2.02	-2.5	1589	31.6
6.3	50.29	3.14	2.02	-2.5	1589	31.6
6.4	50.31	3.14	2.06	-2.5	1497	29.7
6.5	50.21	3.12	2.07	-2.5	1582	31.5
6.6	50.09	3.12	2.08	-2.0	1639	32.7
7.1	50.16	3.18	2.03	-2.5	1604	32.0
7.2	50.22	3.13	2.06	-3.0	1617	32.2
7.3	50.19	3.11	2.08	-3.0	1569	31.3
7.4	50.14	3.08	2.07	-3.0	1739	34.7
7.5	50.16	3.08	2.10	-2.5	1748	34.9
7.6	50.18	3.07	2.10	-2.0	1858	37.0
8.1	50.26	3.16	2.09	-2.0	1847	36.7
8.2	50.18	3.12	2.07	-2.0	1762	35.1
8.3	50.19	3.10	2.08	-2.0	1653	32.9
8.4	50.09	3.08	2.08	-2.0	1873	37.4
8.5	50.24	3.07	2.07	-1.5	1733	34.5
8.6	50.27	3.07	2.08	-1.5	1789	35.6
9.1	50.21	3.17	2.04	-1.5	1718	34.2
9.2	50.24	3.14	2.04	-2.0	1739	34.6
9.3	50.19	3.11	2.04	-2.0	1682	33.5
9.4	50.08	3.09	2.05	-2.0	1754	35.0
9.5	50.27	3.09	2.05	-2.0	1382	27.5
9.6	50.22	3.10	2.06	-1.0	1513	30.1
10.1	50.10	3.20	2.03	-3.0	2530	50.5
10.2	50.03	3.16	2.03	-3.5	2640	52.8
10.3	50.08	3.14	2.04	-3.5	3380	67.5

B

L-joint fatigue simulation

A procedure was developed for predicting the fatigue behavior of L-joints. In this model the mode I and II strain energy release rates were calculated at the crack tip for a range of crack lengths and applied crosshead displacements using APDL, after which this data was analyzed in an Excel spreadsheet. In this appendix the steps for this procedure are described and results are provided. Due to the lack of available data, these results were not validated using a real-world example. The input parameters in the APDL model were from joint 1, in which a 3.5 mm pre-crack was present between the skin and stiffener near the stiffener radius. A section of 5.0 mm remained unwelded near the flange tip. A schematic of the weld line is shown in Figure B.1. In Figure 5.13 it was shown that the simulated results for this joint agree well with the experimental results. In the finite element model for the fatigue simulation the boundary conditions of the new test setup were used, instead of the old setup, which was used during experimental testing of joint 1. This was done to reduce the complexity of the model in this example, because for the new setup only one load step was required instead of two for the old setup, as was shown in Figure 5.11 and 5.12. This led to an underprediction of the failure load, as shown in Figure 3.4. For constants c and n in the Paris law, described by

$$\frac{\mathrm{d}a}{\mathrm{d}N} = c \cdot G_{\text{max}}^{n} \tag{B.1}$$

where $\mathrm{d}a/\mathrm{d}N$ is the crack growth rate and G_{max} is the strain energy release rate at the crack tip at peak loading, experimental CF/PEEK data from literature was used [121–123], because no fatigue data on CF/PA11 was available.

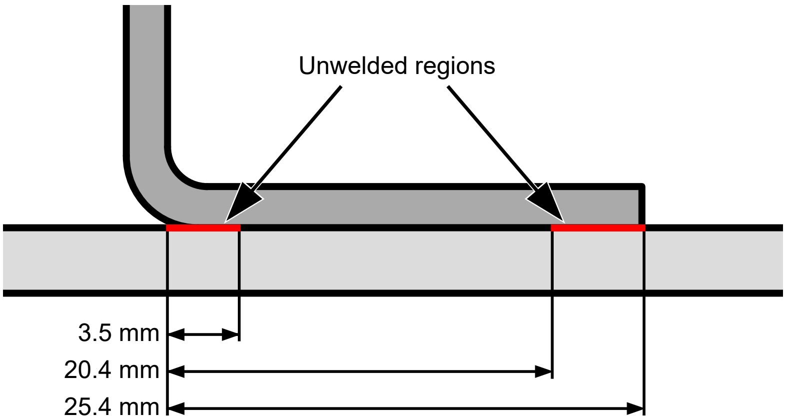

Figure B.1: Schematic of welded and unwelded regions in skin-stiffener interface.

Mall [121] and *Martin and Murri* [122] showed that the Paris law parameters for mode I and II are different, but because in this example the contribution of mode II on for the simulated joint was less than 15% at the initial crack tip and reduced for higher crack lengths, only the mode I delamination growth parameters were used in the model. However, the mode II strain energy release rate was taken into account when determining the mode I value at which abrupt failure would occur for a given crack length. For a crack tip subjected to pure mode I, G_{Ic} was used, but it was reduced for increased contribution of G_{II}. The G_I at which abrupt failure was assumed, was calculated using the following equation:

$$G_{Ic,actual} = \frac{G_{Ic}G_{IIc}}{R_1 G_{Ic} + G_{IIc}} \tag{B.2}$$

where R_1 is equal to G_{II}/G_I for a given crack length. This equation was derived from the linear fracture criterion given in Equation 5.2.

1) The APDL code as developed in Section 5.3.1 was modified, so that the portion in which the calculations were performed and the output file was created, was looped over a range of crack length values. In this example, simulations were done for applied crosshead displacements of [1, 2, 3, 4] mm and for crack lengths of [0, 1, 2, 3, 4, 5, 7, 9, 11, 13, 15, 16, 17, 18, 19, 20] mm. As mentioned previously, the initial crack length was 3.5 mm, but this was implemented during post-processing in the Excel spreadsheet. An output file was created at each of these crack lengths and consisted of columns for applied displacement, applied load and G_I and G_{II} at the crack tip. These output files were then merged into a single file using a Windows batch script. The content of this file was then pasted into the Excel spreadsheet.

2) The ratio R_1, as shown in Equation B.2, was calculated for each crack length. This value was nearly constant over the range of applied displacements. Then, for each crack length, $G_{Ic,actual}$ was calculated and the ratio R_2, defined as $G_{Ic,actual}/G_{Ic}$, was plotted and is shown in Figure B.2. As mentioned previously, this ratio was used to correct the G_I value at which abrupt failure would occur in the fatigue analysis. A third order polynomial trend line was created, in order to calculate this ratio at any given crack length.

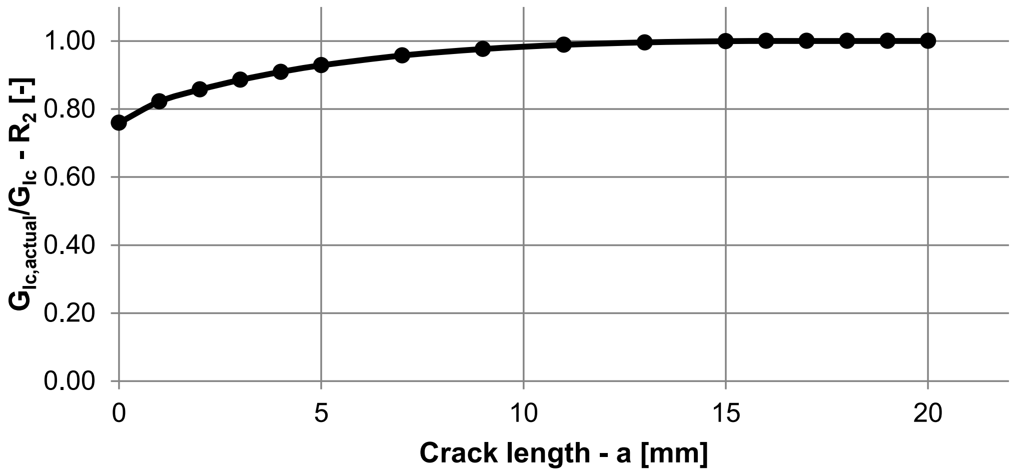

Figure B.2: Ratio R_2 plotted against crack length.

3) In order to use the Paris law, the mode I strain energy release rate G_I at the crack tip should be known for any given crack length for a predefined applied peak loading. However, this information was not directly obtained from the finite element model. Instead, G_I was plotted against applied load for the simulated range of crack lengths, as shown in Figure B.3. A second order polynomial trend line was then created, so that G_I at the crack tip was known for any applied load for the range of crack lengths.

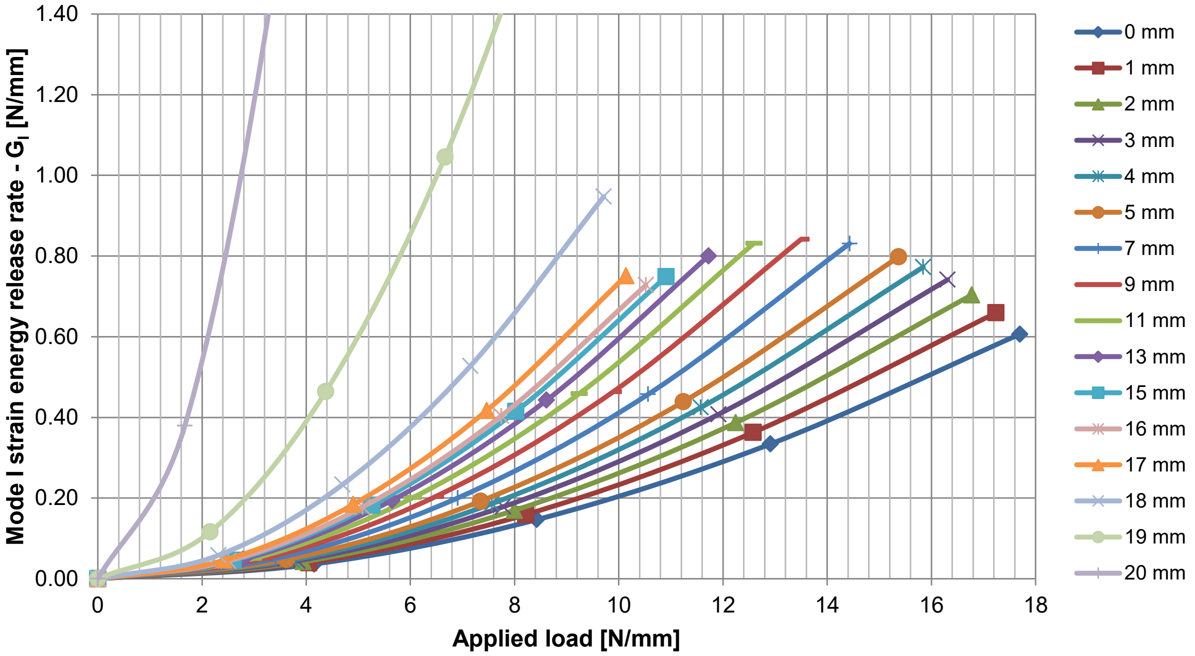

Figure B.3: G_I plotted against applied load for a range of crack lengths.

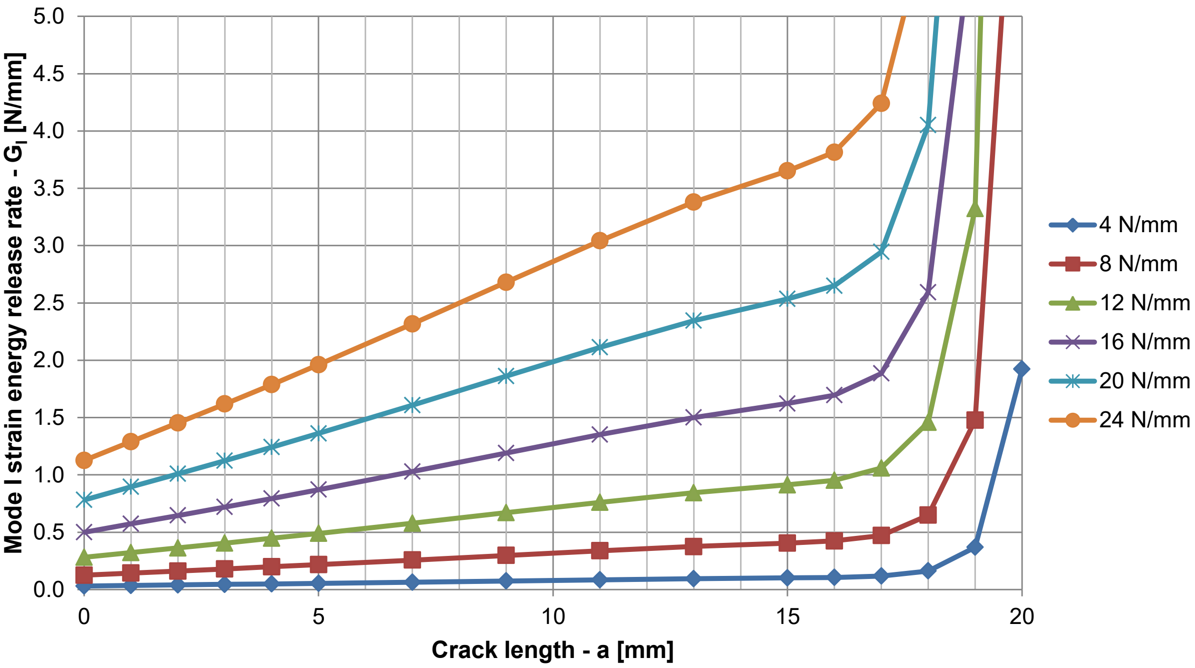

Figure B.4: G_I plotted against crack length for a range of applied loads.

4) Now G_I could be calculated over the range of crack lengths for any applied load. This is shown in Figure B.4. This was an important step in the fatigue analysis, because now the mode I strain energy release rate at the crack tip was known during an entire fatigue experiment for a constant applied cyclic peak loading. In order to use the data as shown in the Figure, a trend line was created, so that G_I was known for any crack length. In this example, a linear trend line was used up to a crack length of 16 mm and a fourth order polynomial trend line was used for the remaining section.

5) Through an iterative process the crack length was calculated for a range of cycle counts. An example of this is shown in Table B.1. The cycle count increment was based on the G_I and $\mathrm{d}a/\mathrm{d}N$ values. If G_I was near $G_{Ic,actual}$ or if the difference between the previous two crack growth rates was relatively high, the steps between the cycle counts were reduced. This was done to ensure that the calculated values converged closely to the ideal case, where an iteration was performed for every cycle.

Table B.1: Iterative process for calculating crack length. These values were found for an applied peak loading of 20 N/mm using the data from *Martin & Murri* (1990) [122] with a loading amplitude of 0.5.

Cycle #	Crack length [mm]	R_2 [–]	G_I [N/mm]	dA/dN [mm/cycle]
1	3.500000	0.894869	1.192612	1.139E-05
2	3.500011	0.894870	1.192613	1.139E-05
3	3.500023	0.894870	1.192615	1.139E-05
⋮	⋮	⋮	⋮	⋮
1000	3.511429	0.895170	1.193967	1.150E-05
2000	3.522930	0.895471	1.195331	1.161E-05
3000	3.534543	0.895775	1.196709	1.173E-05
⋮	⋮	⋮	⋮	⋮

The crack growth rate $\mathrm{d}a/\mathrm{d}N$ was calculated using the Paris law in Equation B.1. Because no fatigue data on CF/PA11 was available, data on CF/PEEK was used instead. The data used for this example is given in Table B.2. In three of these cases the amplitude R, the minimum peak force divided by the maximum peak force, was equal to 0.1 and in one case equal to 0.5. In some of the sources a upper and lower bound for the mode I and II strain energy release rates were given and in those cases the average value was taken. In *Prel et al.* [123] no threshold value was provided.

Table B.2: CF/PEEK fatigue properties from various sources. The loading amplitude R is the minimum peak force divided by the maximum peak force.

Source	G_{Ith} [N/mm]	G_{Ic} [N/mm]	G_{IIc} [N/mm]	c [–]	n [–]
Martin & Murri (1990) [122] - R = 0.1	0.53	2.08	3.13	6.03E-05	6.14
Martin & Murri (1990) [122] - R = 0.5	0.53	2.08	3.13	2.55E-06	8.5
Mall (1989) [121] - R = 0.1	0.2	1.21	1.51	4.70E-03	4.8
Prel et al. (1989) [123] - R = 0.1	—	2.40	2.28	6.52E-07	10.5

In Figures B.5 and B.6 an example is shown of the crack length plotted against the number of cycles. In the first figure the crack length is shown on a linear scale and in the second figure on a logarithmic scale. Note that these figures show the crack length measured after the pre-crack length of 3.5 mm. The number of cycles until failure was found once the crack length exceeded the weld length, in this case at 16.9 mm.

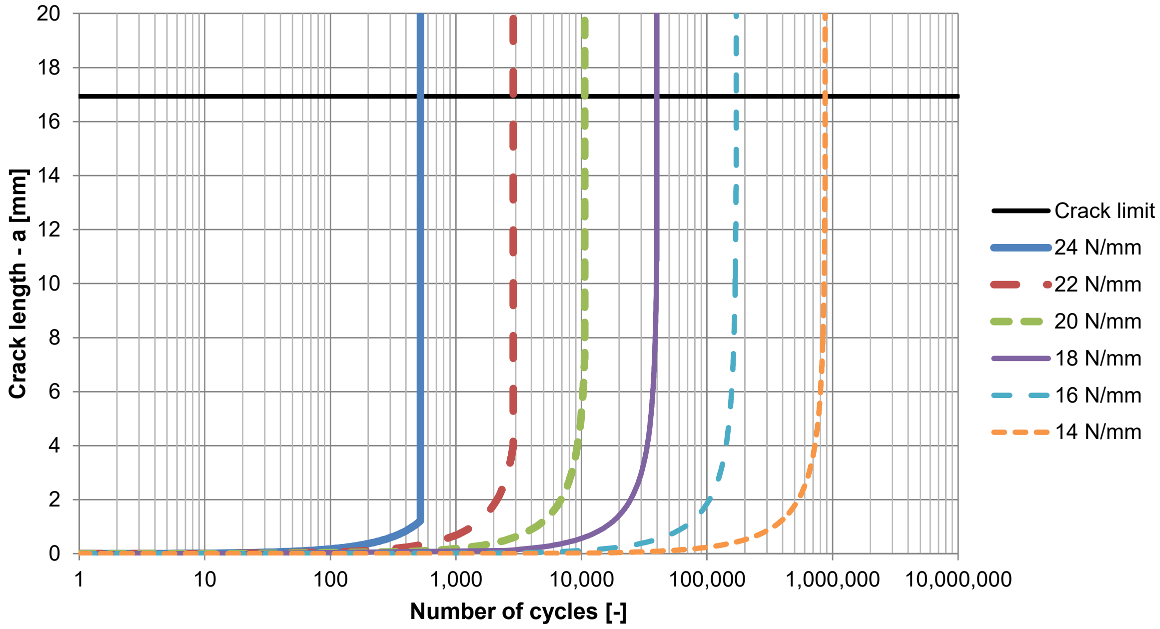

Figure B.5: Crack length plotted on a linear scale against number of cycles for a range of applied loads. These results were found for using the data from *Martin & Murri* (1990) [122] with a loading amplitude of 0.1.

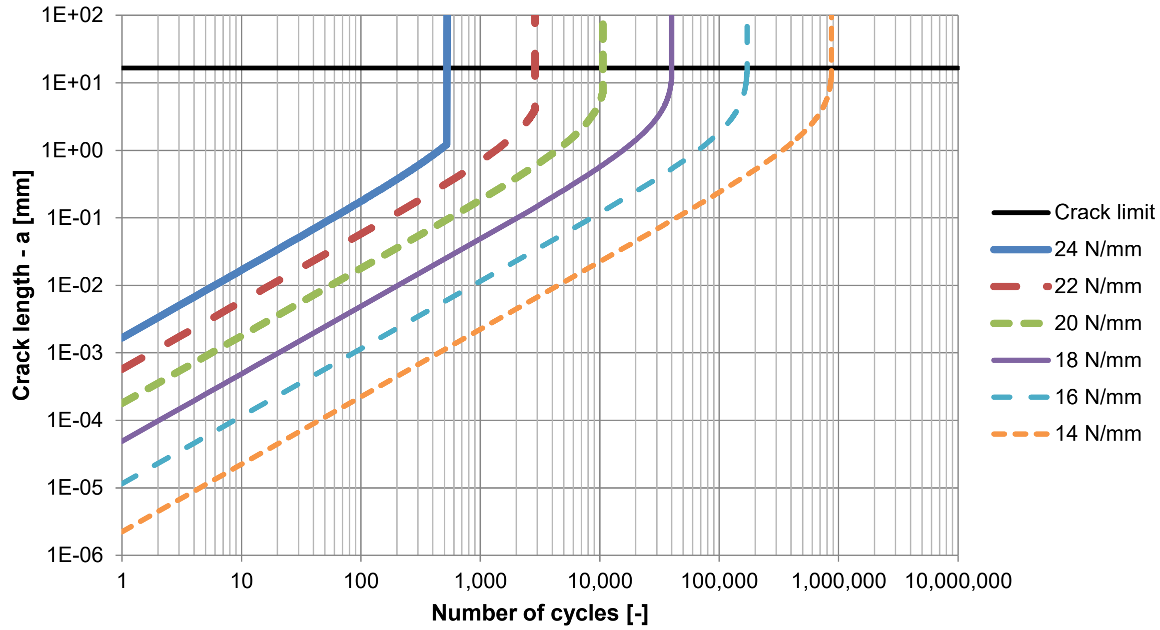

Figure B.6: Crack length plotted on a logarithmic scale against number of cycles for a range of applied loads. These results were found for using the data from *Martin & Murri* (1990) [122] with a loading amplitude of 0.1.

This procedure was followed using the data from the sources listed in Table B.2 and the fatigue curves that were created are shown in Figure B.7. Because the fracture toughness values reported by the sources were different, the calculated static failure load was also different. The experimental test data from joint 1 are shown for reference. In Figure B.8 the same result are shown, but in this case the applied load is divided by the static failure load.

It can be noted from the results that the difference between the fatigue life curves is large. This shows that when performing fatigue life analysis, the Paris law constants should be selected carefully. As was shown in Table B.2, the difference between the constants, as well as the threshold and critical strain energy release rate values, among sources can be large for the same material. Also shown in Figures B.7 and B.8 is that for a reduced load amplitude, thus a higher value for R, the fatigue life is increased. This is as expected, because the joint is subjected to less severe load cycles. As was stated previously, due to the absence of experimental fatigue data, the results from this model were not validated.

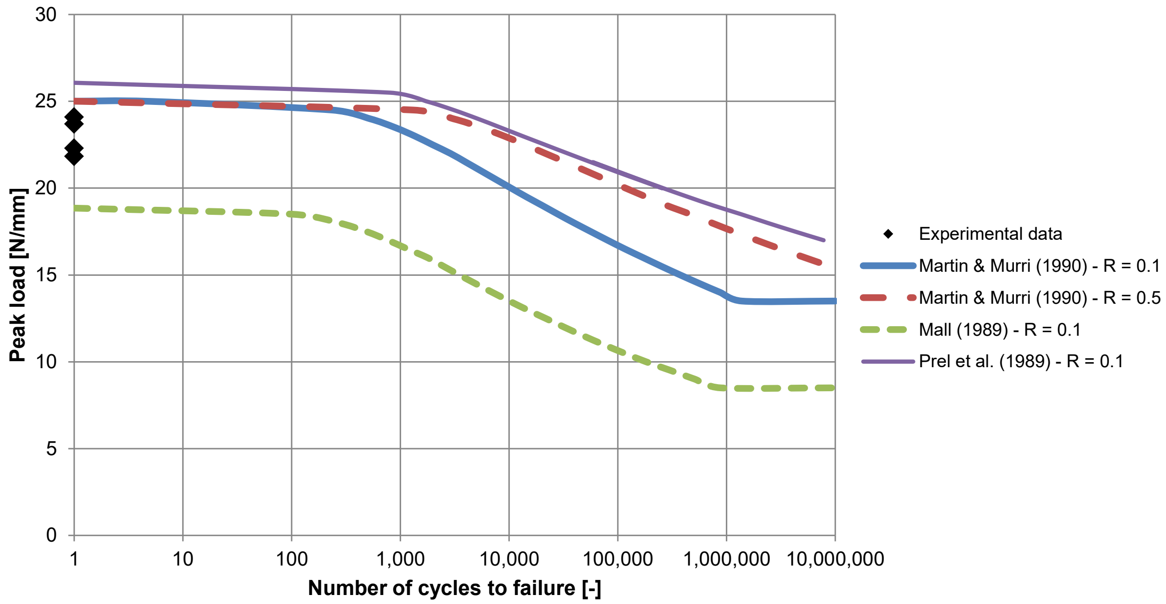

Figure B.7: Fatigue curves for joint 1 using CF/PEEK data. The cyclic peak load is plotted against the number of cycles until failure.

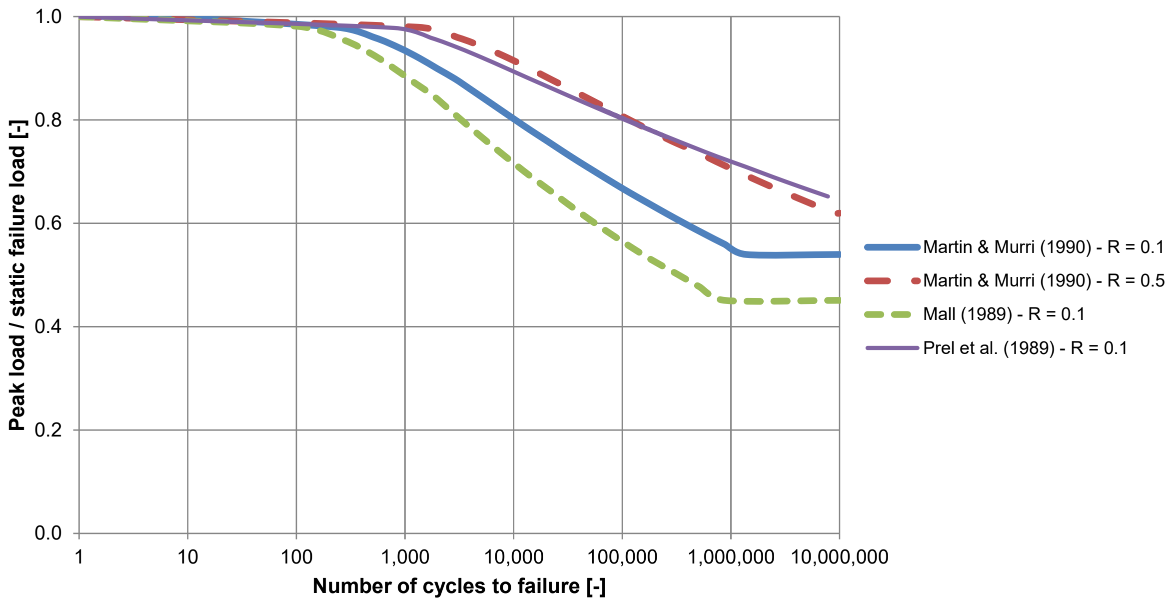

Figure B.8: Fatigue curves for joint 1 using CF/PEEK data. The cyclic peak load divided by the quasi-static failure load is plotted against the number of cycles until failure.

Bibliography

[1] G. Kempe and H. Krauss, “Processing and mechanical properties of fiber-reinforced polyetheretherketone (PEEK),” in *Proceedings of the 14th Congress of the International Council of the Aeronautical Sciences*, Toulouse, France, 1984, pp. 91–98.

[2] P. Curtis, “An investigation of the mechanical properties of improved carbon fibre composite materials,” *Journal of Composite Materials*, vol. 21, no. 12, pp. 1118–1144, 1987.

[3] D. Hunston, R. Moulton, N. Johnston, and W. Bascom, “Matrix resin effects in composite delamination: mode I fracture aspects,” in *Toughened Composites, ASTM STP 937*, N. Johnston, Ed. Philadelphia, PA, USA: American Society for Testing and Materials, 1987, pp. 74–94.

[4] V. Stokes, “Joining methods for plastics and plastic composites: an overview,” *Polymer Engineering and Science*, vol. 29, no. 19, 1989.

[5] J. Van Ingen, A. Buitenhuis, M. Van Wijngaarden, and F. Simmons, III, “Development of the Gulfstream G650 induction welded thermoplastic elevators and rudder,” in *Proceedings of SAMPE 2010 Conference and Exhibition*, Seattle, WA, USA, 2010, pp. 374–389.

[6] A. Offringa, “New thermoplastic composite design concepts and their automated manufacture,” *JEC Composites*, no. 58, pp. 45–49, 2010.

[7] M. Niu, *Airframe Structural Design, Practical Design Information and Data on Aircraft Structures*. Hong Kong: Conmilit Press Ltd., 1988.

[8] D. Stavrov and H. Bersee, “Resistance welding of thermoplastic composites – an overview,” *Composites Part A: Applied Science and Manufacturing*, vol. 36, no. 1, pp. 39–54, 2005.

[9] E. Rybicki and M. Kanninen, “A finite element calculation of stress intensity factors by a modified crack closure integral,” *Engineering Fracture Mechanics*, vol. 9, no. 4, pp. 931–938, 1977.

[10] R. Krueger, “Virtual crack closure technique: History, approach, and applications,” *Applied Mechanics Reviews*, vol. 57, no. 2, pp. 109–143, 2004.

[11] R. Krueger, “The virtual crack closure technique for modeling interlaminar failure and delamination in advanced composite materials,” in *Numerical Modelling of Failure in Advanced Composite Materials*, P. Camanho and S. Hallett, Eds. Cambridge, UK: Woodhead Publishing, 2015, pp. 3–53.

[12] TenCate Advanced Composites USA, Inc., “CETEX TC900 nylon 11,” Morgan Hill, CA, USA, CETEX TC900 nylon 11 datasheet, 2011.

[13] Solvay, “APC (PEKK-FC) thermoplastic polymer prepreg,” Alpharetta, GA, USA, APC (PEKK-FC) datasheet, 2017.

[14] A. Yousefpour, M. Hojjati, and J. Immarigeon, “Fusion bonding/welding of thermoplastic composites,” *Journal of Thermoplastic Composite Materials*, vol. 17, no. 4, pp. 303–341, 2004.

[15] A. Benatar and T. Gutowski, “Methods for fusion bonding thermoplastic composites,” *SAMPE Quarterly*, vol. 18, no. 1, pp. 35–42, 1986.

[16] N. Taylor and R. Davenport, “The resistive implant welding of thermoplastic composite materials,” in *Proceedings of the 49th Annual Technical Conference (ANTEC’91)*, Montreal, Canada, 1991, pp. 2038–2041.

[17] I. Chang, "Thermoplastic matrix composites development update," in *Proceedings of the 37th International SAMPE Symposium*, Anaheim, CA, USA, 1992.

[18] A. Da Costa, E. Botelho, M. Costa, N. Narita, and J. Tarpani, "A review of welding technologies for thermoplastic composites in aerospace applications," *Journal of Aerospace Technology and Management*, vol. 4, no. 3, pp. 255–265, 2012.

[19] W. Werner, "Structural components of fibre reinforced thermoplastics," in *Proceedings of the Fourth European Conference on Composite Materials (ECCM4)*, Stuttgart, Germany, 1990, pp. 831–834.

[20] L. Berglund, "Thermoplastic resins," in *Handbook of Composites*, 2nd ed., S. Peters, Ed. Boston, MA, USA: Springer, 1998, ch. 6, pp. 115–130.

[21] J. Bell, "Thermoplastics shape up," *New Scientist*, vol. 113, no. 1552, p. 29, 1987.

[22] T. Bayerl, M. Duhovic, P. Mitschang, and D. Bhattacharyya, "The heating of polymer composites by electromagnetic induction – a review," *Composites Part A: Applied Science and Manufacturing*, vol. 57, no. 2014, pp. 27–40, 2014.

[23] R. Haimbaugh, *Induction Heat Treating*, 2nd ed. Materials Park, OH, USA: ASM International, 2015.

[24] T. Ahmed, D. Stavrov, H. Bersee, and A. Beukers, "Induction welding of thermoplastic composites – an overview," *Composites Part A: Applied Science and Manufacturing*, vol. 37, no. 1, pp. 1638–1651, 2006.

[25] S. Yarlagadda, H. Kim, J. Gillespie, Jr., N. Shevchenko, and B. Fink, "A study on the induction heating of conductive fiber reinforced composites," *Journal of Composite Materials*, vol. 36, no. 4, pp. 401–421, 2002.

[26] W. Suwanwatana, S. Yarlagadda, and J. Gillespie, Jr., "Hysteresis heating based induction bonding of thermoplastic composites," *Composites Science and Technology*, vol. 66, no. 11-12, pp. 1713–1723, 2006.

[27] R. Rudolf, P. Mitschang, and M. Neitzel, "Induction heating of continuous carbon-fibre-reinforced thermoplastics," *Composites Part A: Applied Science and Manufacturing*, vol. 31, no. 11, pp. 1191–1202, 2000.

[28] S. Pappadà, A. Salomi, J. Montanaro, R. Angiuli, A. Passaro, A. Caruso, and A. Maffezzoli, "Induction welding of PPS-carbon composites: modeling and experimental results," in *Proceedings of the 19th International Conference on Composite Materials (ICCM19)*, Montreal, Canada, 2013, pp. 5481–5488.

[29] R. De Wit, "Induction heating of uni-directional carbon-fibre PEKK composites," MSc thesis, Dept. Aerosp. Struct. and Mater., Delft Univ. of Techol., Delft, The Netherlands, 2017.

[30] R. Rudolf, P. Mitschang, M. Neitzel, and C. Rueckert, "Welding of high-performance thermoplastic composites," *Polymers and Polymer Composites*, vol. 7, no. 5, pp. 309–315, 1999.

[31] M. Flanagan, A. Doyle, K. Doyle, M. Ward, M. Bizeul, R. Canavan, B. Weafer, C. Ó Brádaigh, N. Harrison, and J. Goggins, "Comparative manufacture and testing of induction-welded and adhesively bonded carbon fibre PEEK stiffened panels," *Journal of Thermoplastic Composite Materials*, vol. 13, no. 12, pp. 1622–1649, 2018.

[32] P. Paul, C. Saff, K. Sanger, M. Mahler, H. Kan, and R. Deo, "Out-of-plane analysis for composite structures volume I," NAWCADWAR-94138-60 Vol. I, 1994.

[33] E. Johnson and N. Rastogi, "Load transfer in the stiffener-to-skin joints of a pressurized fuselage," Virginia Polytechnic Inst. and State Univ., Blacksburg, VA, USA, 1995.

[34] C. Shah, H. Kan, and M. Mahler, “Certification methodology for stiffener terminations,” Northrop Grumman Corporation, Hawthorne, CA, USA, DOT/FAA/AR-95/10, 1996.

[35] P. Paul, C. Saff, K. Sanger, M. Mahler, H. Kan, and E. Kautz, “Analysis and test techniques for composite structures subjected to out-of-plane loads,” *Composite Materials Testing and Design*, vol. 10, pp. 238–252, 1992.

[36] H. Kim and K. Kedward, “Stress analysis of adhesively-bonded joints under in-plane shear loading,” *Journal of Adhesion*, vol. 76, no. 1, pp. 1–36, 2001.

[37] M. Niu, *Composite Airframe Structures*. Hong Kong: Conmilit Press Ltd., 1992.

[38] C. Kassapoglou, *Design and Analysis of Composite Structures: With Applications to Aerospace Structures*. Chichester, UK: John Wiley & Sons Ltd, 2010.

[39] ASTM Standard D1002, 2010, “Standard Test Method for Apparent Shear Strength of Single-Lap-Joint Adhesively Bonded Metal Specimens by Tension Loading (Metal-to-Metal),” 2010.

[40] E. Silverman and R. Griese, “Joining methods for graphite/PEEK thermoplastic composites,” *Sampe Journal*, vol. 25, no. 5, pp. 34–38, 1989.

[41] R. Don, L. Bastien, T. Jakobsen, and J. Gillespie, Jr., “Fusion bonding of thermoplastic composites by resistance heating,” *SAMPE Journal*, vol. 26, no. 1, pp. 59–66, 1990.

[42] X. R. Xiao, S. V. Hoa, and K. N. Street, “Processing and modelling of resistance welding of APC-2 composite,” *Journal of Composite Materials*, vol. 26, no. 7, pp. 1031–1049, 1992.

[43] M. Van Wijngaarden, “Robotic induction welding of carbon fiber reinforced thermoplastics,” in *Proceedings of the 37th International SAMPE Technical Conference*, Seattle, WA, USA, 2005.

[44] M. Dubé, P. Hubert, J. Gallet, D. Stavrov, H. Bersee, and A. Yousefpour, “Metal mesh heating element size effect in resistance welding of thermoplastic composites,” *Journal of Composite Materials*, vol. 46, no. 8, pp. 911–919, 2012.

[45] É. Talbot, P. Hubert, M. Dubé, and A. Yousefpour, “Optimization of thermoplastic composites resistance welding parameters based on transient heat transfer finite element modeling,” *Journal of Thermoplastic Composite Materials*, vol. 26, no. 5, pp. 699–717, 2013.

[46] I. Fernandez Villegas, L. Moser, A. Yousefpour, P. Mitschang, and H. Bersee, “Process and performance evaluation of ultrasonic, induction and resistance welding of advanced thermoplastic composites,” *Journal of Thermoplastic Composite Materials*, vol. 26, pp. 1007–1024, 2013.

[47] P. O’Shaughnessey, M. Dubé, and I. Fernandez Villegas, “Modeling and experimental investigation of induction welding of thermoplastic composites and comparison with other welding processes,” *Journal of Composite Materials*, vol. 50, no. 21, pp. 2895–2910, 2016.

[48] ASTM Standard D3163, 2001 (2014), “Standard Test Method for Determining Strength of Adhesively Bonded Rigid Plastic Lap-Shear Joints in Shear by Tension Loading,” 2001.

[49] P. Meakin, F. Cogswell, A. Halbritter, A. Smiley, and P. Staniland, “Thermoplastic interlayer bonding of aromatic polymer composites – methods for using semi-crystallized polymers,” *Composites Manufacturing*, vol. 2, no. 2, pp. 86–91, 1991.

[50] ASTM Standard D5868, 2001 (2014), “Standard Test Method for Lap Shear Adhesion for Fiber Reinforced Plastic (FRP) Bonding,” 2001.

[51] I. De Baere, W. Van Paepegem, and J. Degrieck, “Study of the interlaminar quasi-static and fatigue behaviour of a carbon PPS using the single lap shear geometry,” in *Proceedings of the 16th European Conference on Composite Materials (ECCM16)*, Seville, Spain, 2014, pp. 22–26.

[52] S. Pappadà, A. Salomi, J. Montanaro, A. Passaro, A. Caruso, and A. Maffezzoli, "Fabrication of a thermoplastic matrix composite stiffened panel by induction welding," *Aerospace Science and Technology*, vol. 43, pp. 314–320, 2015.

[53] M. Dubé, A. Chazerain, P. Hubert, A. Yousefpour, and H. Bersee, "Characterization of resistance-welded thermoplastic composite double-lap joints under static and fatigue loading," *Journal of Thermoplastic Composite Materials*, vol. 28, no. 6, pp. 762–776, 2015.

[54] ASTM Standard D3528, 1996 (2016), "Standard Test Method for Strength Properties of Double Lap Shear Adhesive Joints by Tension Loading," 2016.

[55] K. Tserpes, R. Růžek, and S. Pantelakis, "Strength of Pi shaped non-crimp fabric adhesively bonded joints," *Plastics, Rubber and Composites*, vol. 41, no. 2, pp. 100–106, 2012.

[56] G. Pearce, C. Tao, Y. Quek, and N. Chowdhury, "A modified Arcan test for mixed-mode loading of bolted joints in composite structures," *Composite Structures*, vol. 187, pp. 203–211, 2018.

[57] M. Sutton, A. Reynolds, J. Yan, B. Yang, and N. Yuan, "Microstructure and mixed mode I/II fracture of AA2524-T351 base material and friction stir welds," *Engineering Fracture Mechanics*, vol. 73, no. 4, pp. 391–407, 2006.

[58] S. Coppieters, P. Lava, H. Sol, P. Van Houtte, and D. Debruyne, "Multi-axial quasi-static strength of a clinched sheet metal assembly," in *Proceedings of the 2012 Annual Conference on Experimental and Applied Mechanics*, 2012, pp. 339–344.

[59] J. Cognard, P. Davies, B. Gineste, and L. Sohier, "Development of an improved adhesive test method for composite assembly design," *Composites Science and Technology*, vol. 65, no. 3-4, pp. 359–368, 2005.

[60] R. Créac'hcadec, G. Jamin, J. Cognard, and P. Jousset, "Experimental analysis of the mechanical behaviour of a thick flexible adhesive under tensile/compression-shear loads," *International Journal of Adhesion and Adhesives*, vol. 48, pp. 258–267, 2014.

[61] L. Alfonso, C. Badulescu, and N. Carrere, "Use of the modified Arcan fixture to study the strength of bonded assemblies for automotive applications," *International Journal of Adhesion and Adhesives*, vol. 80, pp. 104–114, 2018.

[62] M. Banea and L. Da Silva, "Adhesively bonded joints in composite materials: an overview," *Proceedings of the Institution of Mechanical Engineers, Part L: Journal of Materials: Design and Applications*, vol. 223, no. 1, pp. 1–18, 2009.

[63] S. Budhe, M. Banea, S. De Barros, and L. Da Silva, "An updated review of adhesively bonded joints in composite materials," *International Journal of Adhesion and Adhesives*, vol. 72, pp. 30–42, 2017.

[64] T. Lang and P. Mallick, "Effect of spew geometry on stresses in single lap adhesive joints," *International Journal of Adhesion and Adhesives*, vol. 18, no. 3, pp. 167–177, 1998.

[65] G. Belingardi, L. Goglio, and A. Tarditi, "Investigating the effect of spew and chamfer size on the stresses in metal/plastics adhesive joints," *International Journal of Adhesion and Adhesives*, vol. 22, no. 4, pp. 273–282, 2002.

[66] M. Quaresimin and M. Ricotta, "Fatigue behaviour and damage evolution of single lap bonded joints in composite material," *Composites Science and Technology*, vol. 66, no. 2, pp. 176–187, 2006.

[67] K. Kim, J. Yoo, Y. Yi, and C. Kim, "Failure mode and strength of uni-directional composite single lap bonded joints with different bonding methods," *Composite Structures*, vol. 72, no. 4, pp. 477–485, 2006.

[68] Z. Wang, L. Wang, W. Guo, H. Deng, J. Tong, and F. Aymerich, "An investigation on strain/stress distribution around the overlap end of laminated composite single-lap joints," *Composite Structures*, vol. 89, no. 4, pp. 589–595, 2009.

[69] Y. Yang, L. Wu, Y. Guo, and Z. Zhou, “Effect of spew fillets on strength of single-lap adhesive composites joints,” *Advanced Materials Research*, vol. 239-242, pp. 810–814, 2011.

[70] A. Çalık, “Effect of adherend shape on stress concentration reduction of adhesively bonded single lap joint,” *Engineering Review*, vol. 36, no. 1, pp. 29–34, 2016.

[71] H. Shi, I. Fernandez Villegas, and H. Bersee, “An investigation on the strain distribution of resistance welded thermoplastic composite joints,” in *Proceedings of the 53rd AIAA/ASME/ASCE/AHS/ASC Structures, Structural Dynamics and Materials Conference*, Honolulu, HI, USA, 2012, pp. 1425–1433.

[72] L. Da Silva and R. Adams, “Techniques to reduce the peel stresses in adhesive joints with composites,” *International Journal of Adhesion and Adhesives*, vol. 27, no. 3, pp. 227–235, 2007.

[73] W. Renton and J. Vinson, “Fatigue behavior of bonded joints in composite material structures,” *Journal of Aircraft*, vol. 12, no. 5, pp. 442–447, 1975.

[74] J. Renton and J. Vinson, “On the behavior of bonded joints in composite material structures,” *Engineering Fracture Mechanics*, vol. 7, pp. 41–60, 1975.

[75] K. Shin, J. Lee, and D. Lee, “A study on the lap shear strength of a co-cured single lap joint,” *Journal of Adhesion Science and Technology*, vol. 14, no. 1, pp. 123–139, 2000.

[76] L. Da Silva, P. Das Neves, R. Adams, A. Wang, and J. Spelt, “Analytical models of adhesively bonded joints – Part II: Comparative study,” *International Journal of Adhesion and Adhesives*, vol. 29, no. 3, pp. 331–341, 2009.

[77] H. Roh and C. Sun, “The effect of joint configuration on joint strength,” in *Proceedings of the 25th Technical Conference of the American Society for Composites and 14th US-Japan Conference on Composite Materials 2010*, vol. 1, Dayton, OH, USA, 2010, pp. 397–406.

[78] J. Neto, R. Campilho, and L. Da Silva, “Parametric study of adhesive joints with composites,” *International Journal of Adhesion and Adhesives*, vol. 37, pp. 96–101, 2012.

[79] F. Lionetto, S. Pappadà, G. Buccoliero, and A. Maffezzoli, “Finite element modeling of continuous induction welding of thermoplastic matrix composites,” *Materials and Design*, vol. 120, pp. 212–221, 2017.

[80] F. Sacchetti, “Interlaminar toughness of fusion bonded thermoplastic composites,” PhD dissertation, Univ. of Twente, Enschede, The Netherlands, 2017.

[81] S. Gao and J. Kim, “Cooling rate influences in carbon fibre/PEEK composites. Part 1. Crystallinity and interface adhesion,” *Composites Part A: Applied Science and Manufacturing*, vol. 31, pp. 517–530, 2000.

[82] T. Choupin, “Mechanical performances of PEKK thermoplastic composites linked to their processing parameters,” PhD dissertation, Arts et Métiers ParisTech, Paris, France, 2017.

[83] W. Lee, M. Talbott, G. Springer, and L. Berglund, “Effects of cooling rate on the crystallinity and mechanical properties of thermoplastic composites,” *Journal of Reinforced Plastics and Composites*, vol. 6, no. 1, pp. 2–12, 1987.

[84] I. Lee, D. Kim, K. Jung, H. Kim, and H. Kim, “Effect of the cooling rate on the mechanical properties of glass fiber reinforced thermoplastic composites,” *Composite Structures*, vol. 177, pp. 28–37, 2017.

[85] Committee on Thermoplastic Composites as Structural Components, “The place for thermoplastic composites in structural components,” Washington, D.C., USA, NBAB-434, 1987.

[86] S. Feih and H. Shercliff, “Adhesive and composite failure prediction of single-L joint structures under tensile loading,” *International Journal of Adhesion and Adhesives*, vol. 25, no. 1, pp. 47–59, 2005.

[87] Z. Sápi, R. Butler, and A. Rhead, “Filler materials in composite out-of-plane joints – a review,” *Composite Structures*, vol. 207, pp. 787–800, 2019.

[88] M. Li, P. Chen, B. Kong, T. Peng, Z. Yao, and X. Qiu, “Influences of thickness ratios of flange and skin of composite T-joints on the reinforcement effect of Z-pin,” *Composites Part B: Engineering*, vol. 97, pp. 216–225, 2016.

[89] D. Huan, Y. Li, Y. Tan, X. Zhang, and J. Xiao, “On the assessment of the load-bearing capacity of Z-pinned composite T-joint under out-of-plane tension,” *Journal of Reinforced Plastics and Composites*, vol. 36, no. 22, pp. 1639–1650, 2017.

[90] D. Haugen, “Fracture of skin-stiffener intersections in composite wind turbine blade structures,” MSc thesis, Montana State Univ., Bozeman, USA, 1998.

[91] M. Hyer and D. Cohen, “Calculation of stresses and forces between the skin and stiffener in composite panels,” in *Proceedings of the 28th Structures, Structural Dynamics and Materials Conference*, Monterey, CA, USA, 1987, pp. 165–173.

[92] C. Kassapoglou, “Stress determination at skin-stiffener interfaces of composite stiffened panels under generalized loading,” *Journal of Reinforced Plastics and Composites*, vol. 13, pp. 555–571, 1994.

[93] P. Minguet and T. O’Brien, “Analysis of test methods for characterizing skin/stringer debonding failures in reinforced composite panels,” in *Composite Materials: Testing and Design, Twelfth Volume, ASTM STP 1274*, R. Deo and C. Saff, Eds. American Society for Testing and Materials, 1996, pp. 105–124.

[94] M. Cvitkovich, T. O’Brien, and P. Minguet, “Fatigue debonding characterization in composite skin/stringer configurations,” National Aeronautics and Space Administration, Hampton, VA, USA, NASA Tech. Memo. 110331, 1997.

[95] R. Krueger, M. Cvitkovich, T. O’Brien, and P. Minguet, “Testing and analysis of composite skin/stringer debonding under multi-axial loading,” *Journal of Composite Materials*, vol. 34, pp. 1263–1300, 2000.

[96] M. Dubé, P. Hubert, A. Yousefpour, and J. Denault, “Resistance welding of thermoplastic composites skin/stringer joints,” *Composites Part A: Applied Science and Manufacturing*, vol. 38, no. 12, pp. 2541–2552, 2007.

[97] *Composite Materials Handbook, Vol. 3 - Polymer Matrix Composites Materials Usage, Design, and Analysis*. CMG-17-3G, SAE International, 2012.

[98] J. Hoffmann, A. Brast, and G. Scharr, “Z-pin insertion process for through-thickness reinforced thermoplastic composites,” *Journal of Composite Materials*, vol. 53, no. 2, pp. 173–182, 2019.

[99] C. Inglis, “Stresses in a plate due to the presence of cracks and sharp corners,” *Transactions of the Institute of Naval Architects*, vol. 55, pp. 219–242, 1913.

[100] A. Griffith, “The phenomena of rupture and flow in solids,” *Philosophical Transactions of the Royal Society of London. Series A, Containing Papers of a Mathematical or Physical Character*, vol. 221, pp. 163–198, 1921.

[101] G. Irwin, “Fracture,” in *Handbuch der Physik VI*, S. Flügge, Ed. Berlin, Germany: Springer-Verlag, 1958, pp. 551–590.

[102] R. Krueger, P. Minguet, and T. O’Brien, “Implementation of interlaminar fracture mechanics in design: an overview,” in *Proceedings of the 2003 International Conference on Composite Materials (ICCM-14)*, San Diego, CA, USA, 2003.

[103] ASTM Standard D5528, 2013, “Standard Test Method for Mode I Interlaminar Fracture Toughness of Unidirectional Fiber-Reinforced Polymer Matrix Composites,” 2013.

[104] S. Béland, *High Performance Thermoplastic Resins and Their Composites*, Park Ridge, NJ, USA, 1990.

[105] W. Brocks, "The cohesive model," in *Solid Mechanics and Its Applications: Plasticity and Fracture*, J. Barber and A. Klarbring, Eds. Cham, Switzerland: Springer, 2018, vol. 244, pp. 151–170.

[106] E. Barbero, *Introduction to composite materials design*, 3rd ed. Boca Raton, FL, USA: CRC Press, 2018.

[107] EOS GmbH, "PA1101," PA1101 datasheet, 2019.

[108] EOS GmbH, "PA2200 Performance 1.0," PA2200 datasheet, 2019.

[109] Promolding BV. "PRIM | Printed Injection Mould". [Online]. Available: https://www.p3d-prim.com/,

[110] Huntsman Advanced Materials, "Araldite 2048-1," Basel, Switzerland, Araldite 2048-1 datasheet, 2016.

[111] M. Mohd Tahir, W. Wang, and T. Matsubara, "Failure behavior of quasi-isotropic carbon fiber-reinforced polyamide composites under tension," *Advanced Composite Materials*, vol. 27, no. 5, pp. 483–497, 2017.

[112] J. De Vries, M. Bosboom, and M. Labordus, "Developments on thermoplastic induction welding," in *SC Aerospace Conference & Expo 2016 ACE'16 Technical Symposium Proceedings*, Columbia, SC, USA, 2016.

[113] S. Guo and R. Morishima, "Numerical analysis and experiment of composite sandwich T-joints subjected to pulling load," *Composite Structures*, vol. 94, no. 1, pp. 229–238, 2011.

[114] T. Koh, S. Feih, and A. Mouritz, "Experimental determination of the structural properties and strengthening mechanisms of z-pinned composite T-joints," *Composite Structures*, vol. 93, no. 9, pp. 2222–2230, 2011.

[115] M. Thawre, K. Pandey, A. Dubey, K. Verma, D. Peshwe, R. Paretkar, N. Jagannathan, and C. Manjunatha, "Effect of ply-drop on fatigue life of a carbon fiber composite under a fighter aircraft spectrum load sequence," *Composites Part B: Engineering*, vol. 86, pp. 120–125, 2016.

[116] J. Justo, J. Reinoso, and A. Blázquez, "Pull-off tests of single T-stiffened specimens," *Composite Structures*, vol. 177, pp. 13–27, 2017.

[117] Parts On Demand BV. [Online]. Available: https://partsondemand.eu/,

[118] D. Leach, D. Curtis, and D. Tamblin, "Delamination behavior of carbon fiber/poly(etheretherketone) (PEEK) composites," in *Toughened Composites, ASTM STP 937*, N. Johnston, Ed. Philadelphia, PA, USA: American Society for Testing and Materials, 1987, pp. 358–380.

[119] R. Krueger, "Application of benchmark examples to assess the single and mixed-mode static delamination propagation capabilities in ANSYS," National Aeronautics and Space Administration, Hampton, VA, USA, NASA CR-2012-217588, 2012.

[120] J. Reeder, "3D mixed-mode delamination fracture criteria – an experimentalist's perspective," in *Proceedings of the 21st Annual Technical Conference*. Dearborn, MI, USA: American Society for Composites, 2006.

[121] S. Mall, "Influence of resin on delamination and debonding mechanisms of composite materials under fatigue loading," in *Interlaminar Fracture of Composites*, E. Armanios, Ed. Aedermannsdorf, Switzerland: Trans Tech Publication, 1989, pp. 209–224.

[122] R. Martin and G. Murri, "Characterization of mode I and mode II delamination growth and thresholds in AS4/PEEK composites," in *Composite Materials: Testing and Design, Ninth Volume, ASTM STP 1059*, S. Garbo, Ed. Philadelphia, PA, USA: American Society for Testing and Materials, 1990, pp. 251–271.

[123] Y. Prel, P. Davies, M. Benzeggagh, and F. De Charentenay, “Mode I and mode II delamination of thermosetting and thermoplastic composites,” in *Composite Materials: Fatigue and Fracture, Second Volume, ASTM STP1012*, P. Lagace, Ed. Philadelphia, PA, USA: American Society for Testing and Materials, 1989, pp. 251–269.